UNIVERSIDADE DE LISBOA
FACULDADE DE CIÊNCIAS
DEPARTAMENTO DE ENGENHARIA GEOGRÁFICA, GEOFÍSICA E ENERGIA

Modelling Venus-like exoplanetary atmospheres with a GCM: planetary parameters impact on the large-scale circulation and observational prospects

Diogo Filipe Gonçalves dos Santos Quirino

Mestrado em Ciências Geofísicas
Especialização em Meteorologia e Oceanografia

Dissertação orientada por:
Doutor Pedro Machado
Doutora Gabriella Gilli

2022

“In space there are countless constellations, suns and planets; we see only the suns because they give light; the planets remain invisible, for they are small and dark. There are also numberless earths circling around their suns...”

– Giordano Bruno, *Despre infinit univers si lumi* (1584)

Figure 0. Earth photographed from Voyager 2 on its way to the outer Solar System.

“Look again at that dot. That’s here. That’s home. That’s us. On it everyone you love, everyone you know, everyone you ever heard of, every human being who ever was, lived out their lives. The aggregate of our joy and suffering, thousands of confident religions, ideologies, and economic doctrines, every hunter and forager, every hero and coward, every creator and destroyer of civilization, every king and peasant, every young couple in love, every mother and father, hopeful child, inventor and explorer, every teacher of morals, every corrupt politician, every “superstar,” every “supreme leader”, every saint and sinner in the history of our species lived there–on a mote of dust suspended in a sunbeam.

The Earth is a very small stage in a vast cosmic arena. Think of the rivers of blood spilled by all those generals and emperors so that, in glory and triumph, they could become the momentary masters of a fraction of a dot. Think of the endless cruelties visited by the inhabitants of one corner of this pixel on the scarcely distinguishable inhabitants of some other corner, how frequent their misunderstandings, how eager they are to kill one another, how fervent their hatreds.

Our posturings, our imagined self-importance, the delusion that we have some privileged position in the Universe, are challenged by this point of pale light. Our planet is a lonely speck in the great enveloping cosmic dark. In our obscurity, in all this vastness, there is no hint that help will come from elsewhere to save us from ourselves.

The Earth is the only world known so far to harbor life. There is nowhere else, at least in the near future, to which our species could migrate. Visit, yes. Settle, not yet. Like it or not, for the moment the Earth is where we make our stand.

It has been said that Astronomy is a humbling and character-building experience. There is perhaps no better demonstration of the folly of human conceits than this distant image of our tiny world. To me, it underscores our responsibility to deal more kindly with one another, and to preserve and cherish the pale blue dot, the only home we’ve ever known.”

– Carl Sagan, Pale Blue Dot (1994)

(Picture taken from: https://www.planetary.org/explore/space-topics/earth/pale-blue-dot.html)

Special mention

This work is dedicated to Manuel Pedro Nunes Santos,
whose legacy and memory will endure in our actions.

Acknowledgements

My first word go towards my supervisors. I want to express my sincere and deepest gratitude to **Gabriella Gilli**, **Thomas Navarro**, and **Pedro Machado**. Their support and guidance were permanent during this Master Dissertation. The countless meetings, discussions, and e-mails were crucial for the elaboration of this document.

To **Gabriella Gilli**, my internal and first supervisor, for accepting me has her student, for all her patience, time in teaching me how to work with the Generic-GCM and support in helping me analysing the outputs. I started to work under the supervision of Gabriella Gilli for my Bachelor project back in August 2018, then with the Venus GCM. Back then, her dedication to teach me how to work with a GCM was extraordinary and that project motivated me to pursue the current Master project, studying Venus-like exoplanetary atmospheres. I recall the long afternoons where she dedicated to ensure that the Generic-GCM was running smoothly and her endless support in solving launching, compilation situations. Her critical thinking and problem-solving approach have had a positive and everlasting impact in me.

To **Thomas Navarro** from *McGill Space Institute*, my external and second supervisor, for his extraordinary support in helping me analysing the large-scale atmospheric circulation in this work. For providing valuable input to improve the quality of this work.

I am grateful to **Martin Turbet** from *Laboratoire de Météorologie Dynamique* for his incredible support and very useful feedback in double-checking with me the phase curves routines, and for helping me interpreting the phase curves routines.

To **Thomas Fauchez** *from NASA Goddard Space Flight Center* for his valuable help in helping preparing the input files to be read with the `Planetary Spectrum Generator` and later used to produce the transmission spectra of TRAPPIST-1 c.

To **Jérémy Leconte** from *Laboratoire d'astrophysique de Bordeaux* for his time spent in meetings and for double-checking and help interpreting the results of the phase curves of TRAPPIST-1 c, with and without Venus-like clouds.

To **Emmanuel Marcq** from *Laboratoire Atmosphères, Milieux, Observations Spatiales (LATMOS), Université de Versailles Saint-Quentin*, for his valuable discussions on the simulated atmosphere of TRAPPIST-1 c and suggestions for future follow-up studies.

To **Franck Selsis** from *Laboratoire d'astrophysique de Bordeaux* for the support in the phase curves routine.

I want also to thank to the extended research team at ***Laboratoire de Météorologie Dynamique*** for their warm welcome in their team meetings and for their overall support.

This modelling work could not be possible without the help of **Carlos Martins** from the **Lisbon Astronomical Observatory**, whose technical support was decisive to overcome problems. I also want to thank **Sandra Homem** for all the bureaucratic support. Globally, I want to thank to the Lisbon Astronomical Observatory for accepting me as a student and for creating the excellent working conditions that allowed me to deliver this work.

I also want to thank my professors at **Faculdade de Ciências da Universidade de Lisboa** for stimulating my interest in Planetary Physics, for their useful feedback and career preparation. To **Professor Álvaro Peliz** for the amazing discussions on planetary waves and for the excellent and useful numerical exercises during lectures. To **Professor Carlos da Camara** for his support in discussing large-scale atmospheric circulation and for his amazing lectures that so elegantly link concepts. To **Professor Ricardo Trigo** for

the feedback in discussing exoclimatology and for always believing in me. To **Professor Pedro Machado** for his amazing Planetary Science lectures.

I want to thank to my dear friends for life, **Cristiana Ernesto** and **Francisco Bolrão**, for sharing this academic walk with me. Thank you for the extraordinary support! From my heart to yours, I wish you all the success!

O meu agradecimento não fica completo sem regressar onde tudo começou: à minha família. Ao meu pai **António** e à minha mãe **Lídia** por acreditarem naquele menino de 4 anos que se sentava a ler livros de Astronomia. Por me levarem a todos os eventos, por me ensinarem o nome das estrelas, das constelações e dos mares lunares. À minha irmã **Sandra** pela força do seu exemplo, por ser quem é e pela sua integridade e resolução. À minha avó **Maria do Carmo** que permanecerá para sempre comigo, enquanto o vento de leste agitar a canópia das alfarrobeiras no estio e em todos os caíres da noite nos quais se vem a levantar a Lua sobre os montes tingidos de azul.

Por todos aqueles que partiram nestes 2 anos de pandemia: estarão no meu pensamento para sempre.

Resumo

Vários exoplanetas de dimensões terrestres foram detectados nos últimos anos em órbita de estrelas de pequena massa. Estes exoplanetas apresentam períodos orbitais de apenas alguns dias terrestres. Apesar das suas dimensões, a sua curta distância orbital à estrela, associada ao menor raio da própria estrela em comparação com o do Sol, fazem destes mundos os melhores candidatos para estudos atmosféricos de exoplanetas rochosos. Com um fluxo estelar várias vezes superior ao da Constante Solar, o seu Clima será provavelmente mais semelhante ao do de Vénus do que ao da Terra.

Neste trabalho, utilizo um modelo global da circulação da atmosfera (GCM, *Global Circulation Model*), o *Generic-GCM*, para simular uma possível atmosfera semelhante à de Vénus no exoplaneta TRAPPIST-1 c. Este exoplaneta é tomado como um caso representativo de uma possível classe de exoplanetas rochosos a orbitar estrelas do tipo espectral M e que detêm valores de irradiação estelar superiores aos da Constante Solar no topo-da-atmosfera. O *Generic-GCM* foi desenvolvido pela equipa do *Laboratoire de Météorologie Dynamique* (LMD) no âmbito de estudos paleoclimáticos e de exoplanetas. O modelo inclui uma componente 3D de dinâmica, a qual é comum a todos os planetas terrestres, e uma componente física, a qual é específica do planeta. O *Generic-GCM* possui também uma rotina genérica de transferência radiativa que permite simular diferentes composições atmosféricas. Os grandes objectivos deste trabalho consistem em: (1) estudar e descrever a circulação atmosférica de larga-escala neste tipo de exoplanetas; e (2) produzir observáveis baseados nos ficheiros das simulações com o *Generic-GCM*: curvas de fase (luz reflectida e luz emitida) e espectros de transmissão atmosférica, os quais permitam responder aos requisitos de observação futura por instrumentos e missões (e.g., *James Webb Space Telescope*, JWST). Para a obtenção das curvas de fase produzi um código *Python* que permite ao utilizador converter os fluxos radiativos no topo-da-atmosfera do planeta, obtidos da simulação com o GCM. A produção do espectro de transmissão do planeta é obtida após conversão dos perfis atmosféricos da concentração dos gases e dos aerossóis e da temperatura num ficheiro de leitura que permite a produção do espectro com recurso ao *Planetary Spectrum Generator*. Vários pressupostos foram assumidos relativamente à simulação de TRAPPIST-1 c: rotação síncrona, excentricidade e inclinação nulas e uma atmosfera semelhante à de Vénus com 92 *bar* de pressão atmosférica à superfície e uma parametrização de um coberto global de nuvens de ácido sulfúrico, radiativamente activo.

Antes de simular a atmosfera de TRAPPIST-1 c, realizei um teste para avaliar o modo como o *Generic-GCM* representa a circulação atmosférica de larga escala em Vénus, comparando os resultados com o modelo GCM de Vénus, *IPSL-VGCM*. Primeiro, o *Generic-GCM* reproduz o intervalo de pressão onde ocorre a superrotação e os jactos das latitudes elevadas previamente observados com o IPSL-VGCM. Segundo, o *Generic-GCM* responde correctamente à diminuição da irradiação solar no topo-da-atmosfera, da qual resulta uma redução da velocidade da componente zonal do campo do vento. Terceiro, a superrotação é uma característica dinâmica presente no espectro de valores da irradiação solar explorados neste trabalho.

As simulações de TRAPPIST-1 c indicam uma atmosfera mais quente do que a de Vénus, possivelmente consequência da maior emissão de radiação estelar no infravermelho próximo do que no visível resultando na sua posterior absorção pelo Dióxido de Carbono na atmosfera do planeta. A redistribuição de energia do hemisfério diurno para o hemisfério nocturno do planeta é dominada pela circulação meridional e por jactos dirigidos para Este e em superrotação em relação à superfície planetária, um localizado no equador e dois nas latitudes elevadas. A circulação meridional é composta por duas células de grandes dimensões, uma por hemisfério (Norte e Sul), que atravessam a respectiva região polar. O transporte meridional de energia é principalmente explicado pela componente da circulação média meridional, com uma contribuição menor da componente das ondas estacionárias nas latitudes médias em favor do transporte de energia na direcção do pólo. O campo da temperatura no topo da nuvens apresenta um padrão característico (em inglês, *chevron-like pattern*) com deslocação do máximo de temperatura para Este da região sub-estelar. Estas características do campo da temperatura sugerem a advecção de massas de ar quente da região sub-estelar para o terminador da noite pelo jacto equatorial em superrotação. Existem ainda indicações nos resultados da presença de uma onda planetária sobre o equador com velocidade de fase média, $\bar{c}$, de $\sim$ 130 $m\,s^{-1}$ e período, $\overline{T_w}$, de 17.5 horas.

As curvas de fase da radiação reflectida de TRAPPIST-1 c produzidas neste trabalho têm um valor máximo na ordem de 10^{-6} da razão da radiação reflectida pelo planeta e emitida pela estrela (i.e., contraste planeta-estrela) na mesma banda espectral. A ordem de grandeza do valor confirma que a presença de aerossóis de Ácido Sulfúrico, de albedo elevado, em exoplanetas semelhantes a Vénus pode favorecer a sua detecção pelo JWST e outros instrumentos futuros. Este trabalho também verifica que as curvas de fase da radiação emitida pelo planeta permitem explorar diferentes níveis na atmosfera do exoplaneta, dependendo da banda espectral. As bandas de absorção de Dióxido de Carbono permitem obter dados da mesosfera, enquanto as regiões do contínuo do espectro electromagnético permitem explorar a altitude correspondente ao topo das nuvens.

A presença de aerossóis de Ácido Sulfúrico no espectro de transmissão de TRAPPIST-1 c é responsável, como esperado, por impedir a detecção da maior parte das bandas de absorção com excepção das bandas de absorção mais fortes do Dióxido de Carbono (e.g., 4.3 μm ou 15 μm). Os resultados indicam que a detecção de bandas de absorção mais fracas de Dióxido de Carbono pode ser possível e, nesse caso, podem constituir-se como indício da uma atmosfera com concentrações mais elevadas de Dióxido de Carbono, como é o caso da de Vénus. Em particular, este trabalho sugere que uma detecção da banda de absorção de CO_2 centrada nos 4.8 μm pode ser possível, o que pode indicar a presença de uma atmosfera com elevada pressão atmosférica à superfície.

Os resultados deste trabalho também sugerem que a remoção dos aerossóis de Ácido Sulfúrico da simulação de TRAPPIST-1 c conduz a um aumento de temperatura em níveis inferiores da atmosfera e nas regiões polares, por comparação com a simulação com aerossóis.

O estudo paramétrico releva que exoplanetas com raios maiores apresentam uma intensificação do jacto equatorial, menores deslocamentos para Este do máximo de temperatura no topo das nuvens e valores mais elevados do contraste planeta-estrela, tanto para as curvas de fase da radiação reflectida como da radiação emitida. O estudo de ressonâncias orbitais de 3:2 e de 2:1 tem como consequência a modulação da amplitude e da fase orbital de máxima emissão, sugerindo que este observável em particular pode ser usado no futuro para determinar o estado de rotação planetária.

Palavras-chave: TRAPPIST-1 c, Vénus, GCM, Modelação Numérica.

Abstract

In recent years, several Earth-sized exoplanets have been detected in short-period orbits of a few Earth days, around low-mass stars. Despite their small size compared to gas giants, their close-in orbits, combined with the small radius of the host star compared to our Sun's, make these worlds the best targets for atmospheric characterisation among rocky exoplanets. These worlds have stellar irradiation levels that can be several times that of the Earth, suggesting that a Venus-like climate is more likely.

In this work, I use a Global Circulation Model (GCM), the Generic-GCM, to model a possible Venus-like atmosphere on TRAPPIST-1 c as a benchmark of highly-irradiated rocky exoplanets orbiting M-dwarf stars. The model has been developed at the *Laboratoire de Météorologie Dynamique* (LMD) for exoplanet and paleoclimate studies. It includes a 3D dynamical core common to all terrestrial planets and a planet-specific physical part. In addition, the Generic-GCM has a generalised radiative transfer routine for variable atmospheric compositions. The overarching goal is twofold: (1) to study the large-scale atmospheric circulation of highly-irradiated rocky exoplanets; and (2) to address the observational prospects of this kind of planet by producing phase curves (reflection and emission) and transmission spectra to support future space missions (e.g., James Webb Space Telescope, JWST). I assumed that TRAPPIST-1 c is a synchronous rotator with zero eccentricity and obliquity. It has a Venus-like atmosphere, a 92 bar surface atmospheric pressure, and a radiatively active sulphuric acid prescribed global cloud cover. I run a test to assess the Generic-GCM representation of the large-scale atmospheric circulation on Venus, comparing the results with a Venus specific GCM: the IPSL-VGCM. First, the Generic-GCM reproduces the superrotation pressure range and high-latitudes jets observed in the IPSL-VGCM. Second, the Generic-GCM responds well to decreasing insolation by reducing the zonal wind speeds. Third, superrotation is a robust dynamical feature present in the range of insolation explored.

The results for TRAPPIST-1 c indicate a warmer atmosphere than that of Venus, possibly a consequence of carbon dioxide absorption of stellar radiation, which is strongest in the near-infrared. The day-night heat redistribution in the planet is done through eastward superrotation jets (equatorial and two high-latitudes) and meridional circulation. The latter comprises two large cells, one per hemisphere (northern and southern), crossing the pole. Heat transport is mainly explained by its mean meridional circulation component, with a minor poleward contribution of the stationary waves in the mid-latitudes. The cloud top temperature field shows a distinctive chevron-like pattern and an eastward shift of the peak thermal emission from the substellar point, suggesting an advection of warm air masses by the equatorial zonal superrotation jet. There is evidence for an equatorial wave ($\bar{c} \sim 130\ m\, s^{-1}$, $\overline{T_w}$ = 17.5 hours).

The TRAPPIST-1 c reflection phase curves reach a maximum planet-to-star contrast on the order of 10^{-6}, confirming that high albedo sulphuric acid aerosols of Venus-like cloudy exoplanets may favour their detection by JWST and other future instruments. This work also shows that thermal phase curves can sound different atmospheric levels, depending on the spectral band: carbon dioxide absorption bands will sound mesospheric levels, while *continuum* bands will sound the cloud top. The simulated transmission spectrum of TRAPPIST-1 c is flattened by clouds, screening almost all but the strongest carbon dioxide absorption bands (e.g., 4.3 μm, 15 μm). Detection of weaker CO_2 spectral lines might be possible, suggesting a higher abundance, Venus-like carbon dioxide atmosphere. In particular, the work shows that detecting the 4.8 μm CO_2 spectral band might be possible, indicating a high-pressure atmosphere.

The removal of Venus-like aerosols from simulations leads to a warmer deep atmosphere, including the development of polar warming. The parametric study reveals that larger exoplanets will have more intense zonal equatorial jets but a smaller eastward shift of the hotspot and larger planet-to-star contrast in the phase curves. The higher-order spin-orbit resonances will modulate the amplitude and peak emission of the thermal phase curve, suggesting that this observable can be used to constrain the rotation state.

Keywords: TRAPPIST-1 c, Venus, GCM, Numerical Modelling.

Contents

List of Tables

List of Figures

List of Abbreviations

1D - One-dimensional

3D - Three-dimensional

ASR - Absorbed stellar radiation

AU - Astronomical Unit

CCN - Cloud condensation nuclei

CNRS - *Centre national de la recherche scientifique*

E-ELT - European Extremely Large Telescope

ESA - European Space Agency

ESO - European Southern Observatory

GCM - Global Circulation Model

Generic-GCM - Generic Global Circulation Model

GPI - Gemini Planet Imager

HST - Hubble Space Telescope

HZ - Habitable Zone

IA - Institute of Astrophysics and Space Sciences

IAU - International Astronomical Union

IPSL - *Institut Pierre Simon Laplace*

IPSL-VGCM - *Institut Pierre Simon Laplace* - Venus Global Circulation Model

IR - Infrared

JWST - James Webb Space Telescope

LMD - *Laboratoire de Météorologie Dynamique*

LW - Long-wavelength radiation

MIR - Mid-Infrared

MIRI - Mid-Infrared Instrument (from JWST)

M-UV - Middle Ultraviolet

NASA - National Aeronautics and Space Administration

NIR - Near-Infrared

NIRSpec - Near-Infrared Spectrograph (from JWST)

N-UV - Near-Ultraviolet

OLR - Outgoing long-wavelength radiation

PCAR - Phase Curves Assessment Routine

ppb - Parts per billion

ppm - Parts per million

PSG - Planetary Spectrum Generator

SNR - Signal-to-noise ratio

SPHERE - Spectro-Polarimetric High-contrast Exoplanet REsearch instrument

SW - Short-wavelength radiation

TESS - Transiting Exoplanet Survey Satellite

THAI - TRAPPIST Habitable Atmosphere Intercomparison (workshop)

TOA - Top-of-the-atmosphere

TRAPPIST - TRansiting Planets and PlanetesImals Small Telescope

UV - Ultraviolet

VIRA - Venus International Reference Atmosphere

VLT - Very Large Telescope

VZ - Venus Zone

List of Symbols

t_{adv} - Advection timescale

p_b - Base pressure (of the cloud deck)

L - Characteristic horizontal length scale of the flow

U - Characteristic horizontal wind speed scale

α - Convergence factor

f - Coriolis parameter

s - Dry static energy

$\rho_\oplus$ - Earth density

$S_\oplus$ - Earth insolation

$M_\oplus$ - Earth mass

$R_\oplus$ - Earth radii

e - Eccentricity

$h(\lambda)$ - Effective height

R_{eff} - Effective radius

ν_{eff} - Effective variance

T_{eq} - Equilibrium Temperature

q_I - Filter function

F_r - Flux at the top-of-the-atmosphere used in the Generic-GCM

$F_{r,o,cell}$ - Flux from a cell and received by the observer

G - Gravitational constant

z - Height

S - Insolation / Instellation

z_o - Local observer zenith angle

z_s - Local stellar zenith angle

$\rho_♂$ - Mars density

v - Meridional component of the wind

r - Orbital distance

T_P - Orbital period

M - Planetary mass

A_s - Planetary scattering albedo

d_o - Planet-observer distance

p - Pressure

t_{rad} - Radiative timescale

R - Radius

R_p - Resolving power

Ro - Rossby Number

Ω - Rotation rate

a - Semimajor axis

P - Sidereal rotation period / Solid-body rotation period

P_s - Solar day

$L_\odot$ - Solar luminosity

$M_\odot$ - Solar mass

$R_\odot$ - Solar radii

c_p - Specific heat at constant pressure

σ_{SB} - Stefan-Boltzmann constant

$T_{*,eff}$ - Stellar effective temperature

$F_{*,AU}$ - Stellar flux at $1\ AU$

$F_{*,o}$ - Stellar flux at the observer

$F_{*,P}$ - Stellar flux at the planet's orbital distance

$I_{*,s}$ - Stellar intensity at the stellar surface

L_* - Stellar luminosity

M_* - Stellar mass

R_* - Stellar radius

$lat_{observer}$ - Sub-observer latitude

ΔS - Surface element area of the cell

g - Surface gravity

v_t - Tangential velocity

T - Temperature

p_t - Top pressure (of the cloud deck)

$S_{\venus}$ - Venus insolation

w - Vertical component of the wind

$\mathrm{d}u/\mathrm{d}z$ - Vertical wind shear

T_w - Wave period

c - Wave phase speed

u - Zonal component of the wind

Ψ - Zonal mass streamfunction

$\mathrm{d}u/\mathrm{d}x$ - Zonal wind shear

1 Introduction

1.1 Planetary Systems and Exoclimatology

1.1.1 A new frontier for Planetary Science: Exoplanetary Systems

An exoplanet is a planet outside our Solar System. The first detection of a planet orbiting a main-sequence star took place in 1995 (Marcy et al., 1997; Mayor and Queloz, 1995) by *Michel Mayor* and *Didier Queloz* from the University of *Genève*. The discovery granted *Mayor* and *Queloz* the Nobel Prize in Physics 2019 "for the discovery of an exoplanet orbiting a solar-type star". The exoplanet, designated as *51 Pegasi b* (1), stands as a prototype for a new class of astronomical objects and a symbol for a new paradigm in Science. One paradigm breaking centuries of old conventions and, as eloquently put by the Nobel Committee as a "contribution to our understanding of the Earth's place in the cosmos" (Nobel Prize, 2019).

After the discovery of 51 Pegasi b and until the present day (as of April 19^{th}, 2022), the figure of detected and confirmed exoplanets increased to 5 014 objects (NASA, 2022a). Truly Planetary Science and Astrophysics are experiencing a golden age with the detection, confirmation and characterisation of the enormous diversity of planets and their possible climates. Estimates suggest, on average, that each star in the Milky Way galaxy is host to a planet; there will be plenty of targets to study in the future (Cassan et al., 2012). Additionally, rocky exoplanets are likely around a significant fraction of stars (Bonfils et al., 2013; Borucki et al., 2011; Howard et al., 2010). Many discovered exoplanets also mean that observational statistics are becoming available. A first picture on two main parameters of exoplanetary characterisation, the orbital period and planetary radius, is given in Figure 1.1, including a group of nearby exoplanets (closer than 15 pc (2) from Earth) (NASA, 2022a).

Exoplanetary statistics have changed our understanding of Planetary Science, shaped by centuries of Solar System studies. In our own Solar System, two main planet populations emerge: (1) inner rocky planets with small radii and thin atmospheres or no atmosphere (Mercury, Venus, Earth, and Mars); and (2) outer giant planets with large radii and massive gas envelopes (Jupiter, Saturn, Uranus, and Neptune). While the radius separation between the two populations of planets is evident in our Solar System, Exoplanetary Science tells us otherwise. Figure 1.1 shows that the distribution of planetary radii values is continuous from sub-Earth sized planets (roughly 0.8 $R_{\oplus}$) to Jupiter sized (and larger) worlds (roughly 10-11 $R_{\oplus}$). The exoplanets' radius distribution suggests a larger diversity of exoplanetary populations than one would expect in the first place, considering the planets found in our Solar System. For instance, where the predicted transition between small rocky and more massive planets would take place, between 2 - 4 $R_{\oplus}$, there is a *continuum* in the radius distribution. With so many exoplanets falling in the transition regime between rocky and icy giant planets (e.g., Neptune) (Forget and Leconte, 2014), it is possible that the diversity of Solar System worlds might be a particular, specific outcome of the much wider spectrum of possible planets.

---

[1] The exoplanet naming rule for planets orbiting one star combines the host star name with a lowercase letter identifying the planet, starting with the letter "b". Following this rule, later planetary detections in the same system are labelled with subsequent letters. Furthermore, if multiple detections in the same system happen simultaneously, exoplanet naming will follow the orbital distance rule, with the closest exoplanet receiving the first available letter.

[2] A *parsec* or pc is a length unit commonly used in Astronomy to measure distances outside the Solar System. A parsec is approximately equal to $3.0857 \cdot 10^{16}\ m$.

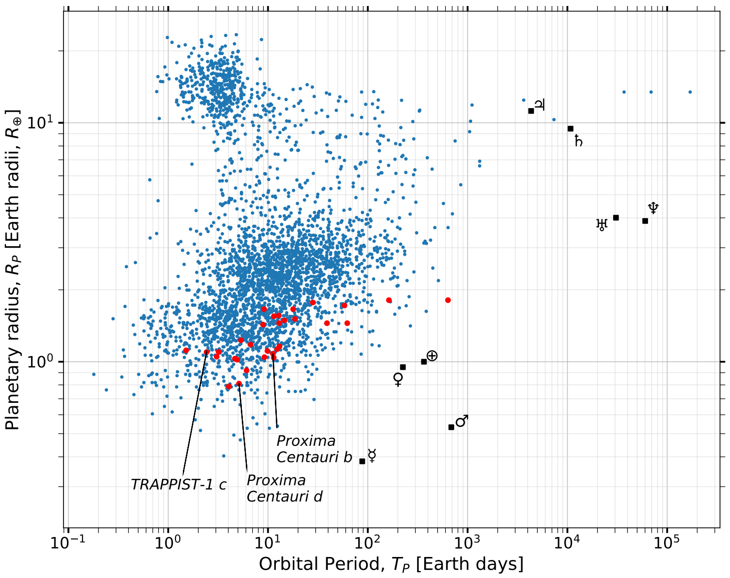

Figure 1.1: The distribution of confirmed exoplanets in orbital period and planetary radius. The confirmed exoplanets (a total of 3334 objects) for which the orbital period T_P in Earth days and the planetary radius R_P in units of $R_\oplus$ (i.e., Earth radii units) are known as of April 19^{th} 2022. The exoplanets are identified by the blue and red dots in the diagram. The Solar System planets are identified by black squares followed by the planet's symbol. The red dots mark a subgroup of nearby rocky exoplanets (31 exoplanets) closer than 15 pc to the Solar System, with radii lower than 2 $R_\oplus$, and with masses lower than 4 $M_\oplus$ (i.e., Earth mass units), with levels of stellar incident flux between 0.2 $S_\oplus$ and 5 $S_\oplus$ (i.e., Solar Constant units). Three of these exoplanets are identified (Proxima Centauri b and d and TRAPPIST-1 c) in the figure.

The possible planetary diversity suggested in Figure 1.1 sets the tone for the questions we want to contribute with an answer in this work. We will seek synergies with Solar System planets to answer those questions, helping establish realistic assumptions for the possible diversity of worlds, atmospheres, and climates. The focus is on the atmosphere and Climate study of nearby rocky, Earth-sized exoplanets (e.g., the red dots in Figure 1.1). Globally, most of the discovered rocky worlds have short orbital periods of a few Earth days and orbit inside Mercury's orbit. Nevertheless, what can we tell about the Climate of these worlds? After all, the largest rocky planets, Venus and Earth, have very distinct atmospheres, climates, and surface conditions.

1.1.2 Detecting Exoplanets: main methods and observational biases

Since 2014, most exoplanetary detections done each year were using the **transit method** (NASA, 2022a). Most of the exoplanets shown in Figure 1.1 were detected via this technique. The transit method measures the stellar flux in search of a periodic decrease caused by a partly stellar occultation by the planet's disk. Consequently, the method allows for a determination of the planet's radius and the orbital period. A strong effort for exoplanetary detection through this method was made by the NASA's space telescope *Kepler* (active from 2009 - 2018), which is responsible alone for the detection of almost 2700 confirmed exoplanets and by the finding that Earth-sized exoplanets are common (Batalha et al., 2013; NASA, 2022a). After the decommissioning of *Kepler*, a new space telescope by NASA, the *Transiting Exoplanet Survey Satellite* (TESS) continued the work of detecting transiting exoplanets, with almost 200 confirmed detections (NASA, 2022a). As such, the technique's success owns to the rapid increase in detections and the diversity of exoplanetary sizes and potential climates (Batalha et al., 2013; Lissauer et al., 2014; Rowe et al., 2014).

The transit method also works under an **observational bias**. This bias is visible in the exoplanet distribution in Figure 1.1, where most exoplanets have short-period orbits of a few to dozens of Earth days. This short-orbital trend is a consequence of the transit method itself. Transiting planets are primarily detected in extensive field surveys of the sky. The reason is that the orbital plane of transiting planets must be aligned with Earth to detect a planet crossing the star's disk. A crucial aspect, demonstrated by Kane and von Braun (2008) is the *geometric factor*: the probability of transit detection is *directly* related to the star's radius and the planet's radius and *inversely proportional* to the orbital distance. Thus, the transit method favours the detection of larger planets orbiting stars with smaller radii (compared to the Sun) in short orbital periods. For instance, in our Solar System, the geometric transit probability of Venus is larger than that of the Earth. Both planets have similar radii, but the Earth's larger orbital distance means a lower transit detection probability. Thus, Earth-sized planets with highly-irradiated climates are more *likely* to be first detected (and characterised) via the transit method (Kane et al., 2013). Additionally, short-orbit planets have more observed transits per observational campaign. Therefore, having a more significant number of transits for a given time interval will improve the transit signature's quality, making it more visible against noise sources (e.g., instrumental), i.e. improving the signal-to-noise ratio (SNR).

The second detection technique by the number of confirmed discoveries is the **radial velocity** method. The planet's mass displaces the system's centre of gravity from the star's centre, leading both the star and the planet to orbit a common centre of gravity. The system's centre of gravity offset is responsible for a star's radial velocity variation. Consequently, the more massive and close the planet is, the greater the radial velocity signal (e.g., 51 Pegasi b, the first confirmed exoplanet, is a short period Jovian mass planet) (NASA, 2022a).

The nature of the two main exoplanet detection methods indicates that detecting rocky, Earth-sized exoplanets is more likely around small mass stars. The lowest mass stars, the **M-dwarf stars**, provide the best opportunity for rocky exoplanet detection and atmospheric characterisation studies in the next decade, as these stars are smaller and dimmer compared to other main sequence spectral types. Transiting planets orbiting them offers the best case for exoplanetary atmosphere follow-up studies.

In summary, the population of Earth-sized exoplanets more amenable for detection and atmosphere characterisation studies in the next decade are: **(i)** orbiting small mass, small radius M-dwarf stars, in **(ii)** short orbital periods (observational bias) - thus are highly-irradiated worlds; and **(iii)** have greater transit signal over the signal's noise - as shorter orbital periods lead to an increase in the number of data acquired per time interval. Owning to the transit observational bias favouring short orbital period exoplanets (**high transit probability**, **high transit frequency**, and **high equilibrium temperature**), Venus-like exoplanets are key targets for the near-term observational campaigns, namely those of TESS and with the recently launched *James Webb Space Telescope* (JWST) (Ostberg and Kane, 2019).

1.1.3 Venus-like exoplanets: a population of highly-irradiated Earth-sized exoplanets

In our Solar System, Venus and Earth have similar radii, masses and likely bulk composition. However, the shorter orbital distance of Venus leads to a higher transit probability (Kane and von Braun, 2008). The observational bias thus indicates that Earth-sized exoplanets with high levels of instellation(3) will be detected and characterised first. These highly-irradiated planets will have instellation flux levels closer to present-day Venus than Earth and will orbit inside the **Habitable Zone** (HZ). The HZ is defined as the range of planetary orbits where bodies of water can remain thermodynamically stable in the liquid state on a planetary surface with adequate atmospheric pressure and temperature (Kasting et al., 1993; Kopparapu et al., 2017, 2013a; Selsis et al., 2007; Yang et al., 2014). The HZ is a concept that serves the purpose of identifying a group of rocky exoplanets whose remote sensing of their atmospheres is more

---

[3] Defined as the amount of stellar energy or stellar irradiance reaching the top-of-the-atmosphere (TOA) (Mackwell et al., 2014).

likely to suggest an Earth-like composition and, ultimately, increase the probability of life's detection. As such, the concept of HZ can not be confused with planetary habitability (Kasting et al., 2014).

Furthermore, to understand where the Venus-Earth Climate divergence originates from (and hence Earth's surface habitability), an estimate on the frequency of rocky exoplanets with Venus-like climates is essential. For this purpose, Kane et al. (2014) define the "**Venus Zone**" (VZ), corresponding to the range of orbits whose instellation values place the planet under a likely runaway greenhouse state, where Climate and surface conditions are more probable to be Venus-like. In Figure 1.2, I represent several nearby Earth-sized exoplanets as a function of their instellation.

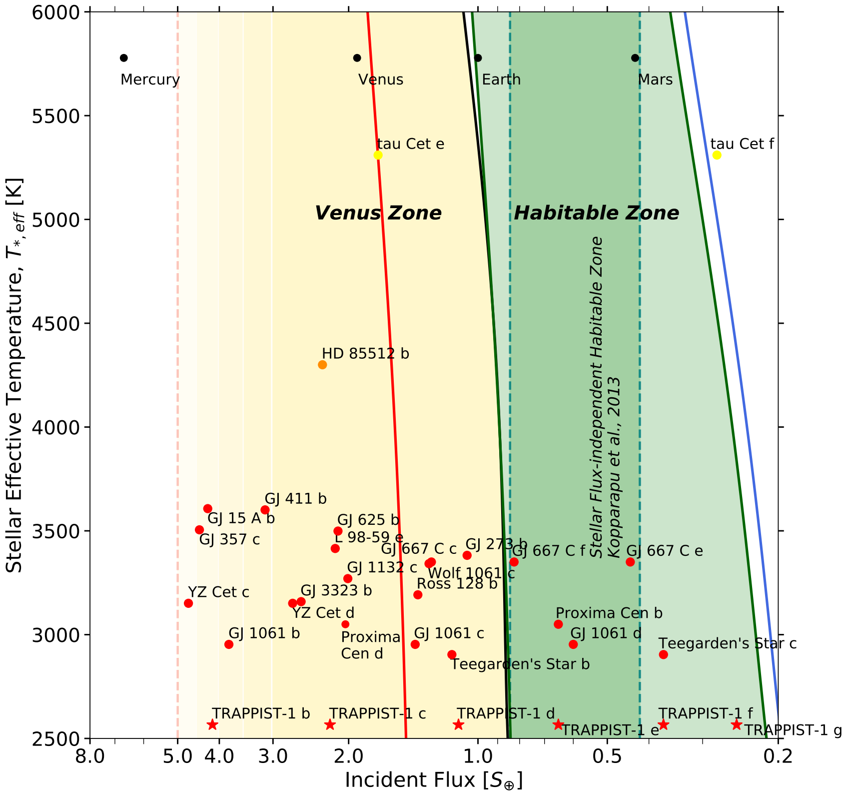

Figure 1.2: The Habitable Zone and Venus Zone for the four innermost Solar System planets and a selection of nearby Earth-sized exoplanets. The incident stellar flux is in Earth flux units, $S_\oplus$, with 1 $S_\oplus$ = 1366 $W\,m^{-2}$, while the stellar effective temperature is in K. The figure represents the range of orbits of the Venus Zone (yellow area) and the Habitable Zone in its conservative extent (green area), according to one-dimensional Climate models. A stellar flux-independent HZ is identified by green dashed lines between 0.42 $S_\oplus$ and 0.842 $S_\oplus$. The curves represent different conditions, following Kopparapu et al. (2013a): "Recent Venus" (solid red); "Runaway Greenhouse" (solid black); "Moist Greenhouse" (inner edge HZ, solid green); "Maximum Greenhouse" (outer edge HZ, solid green); and "Early Mars" (solid blue). The black dots indicate the location of the Solar System planets as a function of insolation. At the same time, several nearby Earth-sized exoplanets are depicted by coloured symbols as a function of their respective instellation. The type of symbol identifies the discovery method: stars for transit and dots for radial velocity. Also, the colours of each symbol identify the spectral type of the host star: red for M-dwarfs, orange for K-dwarfs, and yellow for G-dwarfs. The exoplanet data was taken from NASA's Exoplanet Archive (NASA, 2022a) with the following selection criteria: **(i)** distance closer than 15 pc; **(ii)** planetary radii lower than 2 Earth radii ($R_\oplus$); **(iii)** less than 4 Earth masses ($M_\oplus$); and **(iv)** instellation: 0.2 - 5 $S_\oplus$. A total of 31 confirmed exoplanets are represented in the figure.

Instellation or insolation (in the case of the Solar System) is the first-level approach that separates possible Earth-like and Venus-like climates. For comparison, Venus has an insolation ($S_♀$) nearly twice that of the Earth ($S_\oplus$), i.e., $S_♀$ = 1.911 $S_\oplus$ (Williams, 2022a). The VZ extend from the "runaway greenhouse"([4]) (solid black line in Figure 1.2) to a "conservative" inner edge (dashed orange line in Figure 1.2) where stellar irradiation-driven atmospheric erosion becomes dominant over a planet's ability to

---

[4] Defined as the limit at which the oceans evaporate entirely.

support an atmosphere(5) (Zahnle and Catling, 2017). The concept of VZ allows for an estimation of the occurrence rates of VZ rocky exoplanets, i.e., planets that are likely to have spectral features suggestive of a Venus-like atmosphere. For M-dwarf stars, these planets' frequency is $\sim 32\%$ (Kane et al., 2014)(6).

1.1.4 A population of possible nearby Venus-like exoplanets

Figure 1.2 represents a population of Earth-sized exoplanets in the Solar neighbourhood (see details in the Figure's legend), with 22 exoplanets orbiting in the Venus Zone and eight exoplanets inside the Habitable Zone. Most exoplanets orbit M-dwarf stars, including the transiting planets of TRAPPIST-1 system (Gillon et al., 2016, 2017; Luger et al., 2017a).

Planets in the HZ include Proxima Centauri b, (Anglada-Escudé et al., 2016), TRAPPIST-1 e (Gillon et al., 2017), and GJ 1061 d (Dreizler et al., 2020), these planets are more likely to have temperate surface conditions. The confirmation of whether these planets have a Venus-like or an Earth-like atmosphere or Climate depends on reliable atmospheric studies, namely those provided by transmission spectroscopy (Bean et al., 2017).

Inside the VZ, there are notable discoveries, such as the three innermost planets of the planetary system TRAPPIST-1: b, c and d (Gillon et al., 2016, 2017). Another relevant detection is Proxima Centauri d, announced earlier this year (2022) by *João Faria* (Institute of Astrophysics and Space Sciences, IA-Porto) and colleagues (Faria et al., 2022). Some of these VZ exoplanets, such as TRAPPIST-1 d, have instellation values close to the "runaway greenhouse" limit, making them targets for testing the boundaries of HZ and VZ (other cases might include Teegarden's Star b (Zechmeister et al., 2019), Ross 128 b (Bonfils et al., 2018), Wolf 1061 c (Wright et al., 2016) or GJ 273 b (Astudillo-Defru et al., 2017)). In addition, this particular group of VZ exoplanets will likely serve as a laboratory to study the runaway greenhouse theory and the impacts of atmospheric escape and evolution, creating an ensemble on the possible diversity of rocky exoplanets atmospheres (Kane et al., 2014).

From its instellation value in Figure 1.2, and for being a transiting planet, TRAPPIST-1 c emerges as the best candidate to study a possible Venus-like atmosphere. Future atmospheric observations will depend on whether the planet possesses an atmosphere. The observation of TRAPPIST-1 c with JWST will take place later this year (Kreidberg et al., 2021), with the first cycle of observations focusing on detecting the presence of an atmosphere around the planet.

1.1.5 The TRAPPIST-1 Planetary System

The TRAPPIST-1 planetary system is composed of at least seven Earth-sized transiting planets orbiting one ultracool ($T_{*,eff} = 2566\ K$) M-dwarf star (spectral type M8V) with a very low mass ($M_* = 0.09\ M_\odot$), TRAPPIST-1, located at about 12 pc from the Solar System (Gillon et al., 2016, 2017; Luger et al., 2017a; Van Grootel et al., 2018). The TRAPPIST-1 planets are similar in radius, varying from $\sim 0.76\ R_\oplus$ to $\sim 1.12\ R_\oplus$, and have short orbital periods, ranging from ~ 1.5 to ~ 18.8 Earth days (Agol et al., 2021). The planets orbit a range of instellation values (from $\sim 0.14\ S_\oplus$ to $\sim 4.15\ S_\oplus$), similar to the range of insolation received by the Solar System's rocky planets (Turbet et al., 2020a), as seen in Figure 1.3.

---

[5] Kane et al. (2014) places the VZ inner edge at 25 $S_\oplus$, where the atmosphere escape effects are likely to cause a complete atmospheric erosion (Zahnle and Catling, 2017). However, atmospheres subject to higher instellation levels are likely to be substantially different from that of Venus, deviating from established Venus-like atmosphere composition assumptions, e.g., impact in photochemistry reactions driven by high levels of ionising stellar irradiation. To reach a conservative compromise, we decided to set the VZ in Figure 1.2 at 5 $S_\oplus$.

[6] For Sun-like stars the occurrence rate of VZ planets raises to 42% according to Kane et al. (2014).

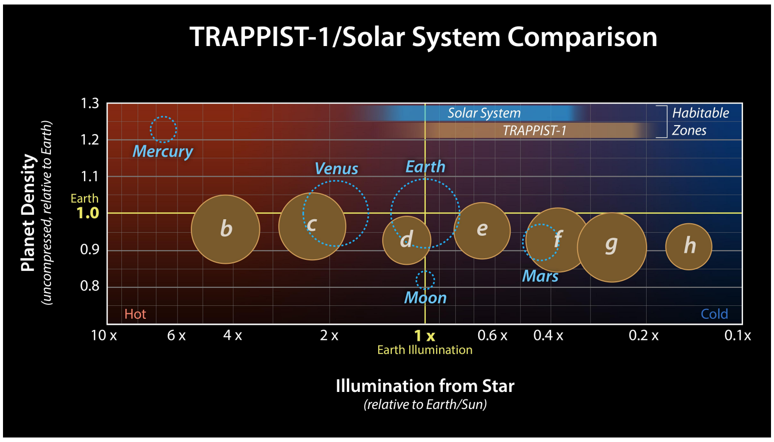

Figure 1.3: Comparison between the TRAPPIST-1 planetary system and the Solar System. The diagram shows the relative planetary radii of the TRAPPIST-1 planets (b to h), instellation in Earth illumination units ($S_\oplus$) and planetary density (relative to Earth). The Solar System inner planets (Mercury to Mars) and the Moon are represented by dashed blue circles according to their relative radii. A comparison between the insolation/instellation ranges of each system HZ is presented in the upper part of the figure. Illustration from: NASA/JPL-Caltech (all data from 2021). (Cofield and Greicius, 2021)

Discovery history The two innermost planets, TRAPPIST-1 b and c, were discovered in 2016 by Gillon et al. (2016). The authors measured TRAPPIST-1 brightness during 62 nights using the telescope TRAPPIST (TRansiting Planets and PlanetesImals Small Telescope)(7). The following year, the NASA/Spitzer Space Telescope confirmed the presence of these two innermost planets. Furthermore, it identified four additional planets while providing evidence of the presence of a seventh planet in the system (Gillon et al., 2017). This study confirmed the orbital period of the six innermost planets, with the outermost planet's period later confirmed by Luger et al. (2017a). Additionally, later follow-up observations confirmed the presence of a seventh planet in the system (Burdanov et al., 2019; Delrez et al., 2018; Ducrot et al., 2018, 2020). The presence of an eighth planet is not confirmed in the recent study by Agol et al. (2021). However, this study has been crucial to refining the system's planetary parameters.

Orbital architecture The TRAPPIST-1 planetary system is very compact, sharing some analogies to the inner rocky Solar System planets (Gillon et al., 2017). The seven planets have sizes and masses similar to those of the Earth, with planets d, e, and h having intermediate sizes between Mars and the Earth (Gillon et al., 2017). Mass estimations for the six innermost planets suggest a rocky composition (Zeng et al., 2016). Orbital inclinations are close to 90°, TRAPPIST-1 c is nearly edge-on to Earth.

The TRAPPIST-1 planetary system architecture is that of an extremely compact system with: **(i)** close-in orbits, all planetary orbits are inside a 0.06 AU (8) distance from the star (Gillon et al., 2017); **(ii)** planets have very low orbital eccentricities (Agol et al., 2021); **(iii)** extremely coplanar orbits (Delrez et al., 2018; Luger et al., 2017a); **(iv)** the six innermost planets are in a near-resonant chain(9), which might lead to strong mutual gravitational interactions between planets (Luger et al., 2017a); **(v)** orbital stability on the timescales on the order of 10 Myr (Agol et al., 2021); and **(vi)** the planets are likely to be tidally-locked (Vinson et al., 2019) or locked in a higher-order spin-orbit resonance, with the latter being unlikely given the low orbital eccentricities (Agol et al., 2021; Gillon et al., 2017; Ribas et al., 2016).

Planetary interior composition TRAPPIST-1's orbital architecture (extremely compact system with orbital resonances) favours an orbital evolution scenario with planetary formation beyond the ice-

---

[7] TRAPPIST is a small 60 cm diameter ground-based telescope located at the *European Southern Observatory* (ESO) facilities in La Silla Observatory, Chile (Gillon et al., 2011, 2013).

[8] 1 Astronomical Unit is by definition 149 597 870 700 m (International Astronomical Union, IAU).

[9] The orbital periods of these planets are near-ratios of small integers.

line(10) followed by inward migration driven by angular momentum interactions with the planetary disk (Cresswell and Nelson, 2006; Mills et al., 2016; Terquem and Papaloizou, 2007). The most-likely formation scenario of TRAPPIST-1 planets constrains their possible interiors, favouring volatile-rich compositions with lower densities than the Earth (Alibert and Benz, 2017; Raymond et al., 2008).

The recent state-of-the-art study by Agol et al. (2021) supports this interior composition scenario. The study refines the planetary parameters of the system: mass, radii, and densities, leading to a better constraint of the planetary interior composition. Each of the planets from TRAPPIST-1 system have an intermediate density between Earth's ($\rho_{\oplus} = 5514\ kg\, m^{-3}$) and that of Mars ($\rho_{♂} = 0.713\ \rho_{\oplus}$) (Williams, 2022b). Their surface gravity spans from 57% of the Earth (planet h) to 110% of Earth (planet b). Furthermore, the pattern of TRAPPIST-1 planets' masses and radii is consistent with a uniform planetary composition for all planets, with each world having lower uncompressed densities than the Solar System rocky planets (Venus, Earth, and Mars), as shown in Figure 1.3. Thus, the planetary parameters found may be consistent with two (not self-limited) hypotheses for the interior composition: **(i)** an iron-depleted rocky mass-radius relationship, with 21% iron (compared to 32% of that of the Earth); or **(ii)** an Earth-like composition enhanced in light elements (e.g., surface water layer or a core-free structure with a highly oxidised iron mantle), with TRAPPIST-1 planets having possible water mass fractions ranging up to 25% of their bulk composition (Agol et al., 2021; Turbet et al., 2020a).

Possible planetary atmospheres There is no confirmation of planetary atmospheres around TRAPPIST-1 planets; however, the system's orbital architecture favours planetary formation at a volatile-rich region followed by inward migration. Therefore, the type of planetary formation might have had an impact on the type of possible planetary atmospheres, mainly by controlling the quantity of initial volatile chemical species accreted by the planets (Turbet et al., 2020a).

The presence of a planetary atmosphere will thus depend on the following factors: **(i)** residence time beyond the ice-line, relevant for establishing the initial volatile reservoir available for late outgassing; **(ii)** the balance between collisional erosion processes versus effective volatile delivery; and **(iii)** atmospheric erosion from conditions arising from the stellar evolution, the magnitude of the stellar wind, and high-energetic stellar radiation. The magnitude of each process has a degree of uncertainty, with the effectiveness of erosion mechanisms likely to be higher for the innermost planets. However, the lower relative densities compared to Earth's favour an internal composition enriched in volatiles and offer a possibility that the initial volatile reservoir can be considerable despite facing strong atmospheric erosion. So what kind of planetary atmospheres can we expect for TRAPPIST-1 planets?

Turbet et al. (2020a) provide a review of the most likely atmospheres in the TRAPPIST-1 system:

- **Water vapour** or **steam dominated atmospheres**. These are more likely for the innermost planets, whose irradiation is above the runaway greenhouse limit for water. The instellation levels are so large that they prevent water condensation on the surface and form oceans. Instead, water vapour is likely to escape to space through atmospheric erosion processes (e.g., hydrodynamic escape (Luger and Barnes, 2015)). These steam atmospheres have the potential to evolve into secondary atmospheres, leaving the planets in a desiccated state;
- **Oxygen dominated atmospheres**. These are the likely abiotically remnant (Meadows, 2017)

---

[10] Orbital distance from the host star in which the temperature of the stellar nebula becomes low enough for water to solidify and remain stable in the solid form. The water ice will be an active element in planetary formation's accretion process, potentially contributing to a decrease in planetary density. The relative planetary densities of TRAPPIST-1 planets are lower than Earth's, suggesting a bulk composition rich in lighter elements (Agol et al., 2021).

from early significant atmospheric erosion of water vapour dominated atmospheres during the superluminous pre-main-sequence phase of the low mass stars (Lincowski et al., 2019);

- **Carbon dioxide dominated atmospheres**. Carbon dioxide is one of the most likely chemical species to accumulate in the planetary atmospheres of TRAPPIST-1 (Lincowski et al., 2019). The gas accumulation is favoured as it is resilient to atmospheric escape processes compared to most common chemical species. The explanation for its resilience comes from its heavy molecular weight and radiative cooling properties, which decrease thermal escape efficiency (Turbet et al., 2020a). Photochemistry reactions can reduce the carbon dioxide levels in the atmosphere, leading to carbon monoxide and oxygen atmosphere accumulation (Gao et al., 2015) - in particular around TRAPPIST-1, which is a low-mass M-dwarf star (Hu et al., 2020). The possible accumulation of several *bar* of carbon monoxide and oxygen in the atmospheres of TRAPPIST-1 planets can still lead to planetary warming via adiabatic heating (Lincowski et al., 2018) and pressure broadening of the remaining carbon dioxide. Such processes might overcome these gases' relative inefficiency for radiative heating since they are not significant greenhouse gases in the first place.

Overall, the planetary atmospheres of TRAPPIST-1 planets are very likely to be **secondary atmospheres**, heavily evolved from their primordial composition (Lincowski et al., 2019). Impact from the long evolution superluminous pre-main-sequence phase (Baraffe et al., 2015) and life-long stellar activity (Tarter et al., 2007) can not be ignored, in particular given TRAPPIST-1 system's age of 7.6 Gyr (Burgasser and Mamajek, 2017). Thus, we can not exclude both possibilities that the highly-irradiated planets in the system (TRAPPIST-1 b and TRAPPIST-1 c) could be airless planets, like Mercury, or have a significant, thick atmosphere like that of Venus.

The exceptionalism of the TRAPPIST-1 system Despite many exoplanet discoveries, most targets lay beyond the current and near-future technological capabilities for atmospheric characterisation studies. The factors that contribute to TRAPPIST-1 being a prime target for future atmospheric characterisation studies are:

- **Ultracool M-dwarf star**. TRAPPIST-1 (spectral type: M8V) is a late-type M-dwarf star (Gillon et al., 2016): these stars have the smallest radii, lowest masses and luminosities of all main-sequence stars, meaning that its planets' relative radii and masses compared to the host star are *larger* than in other planetary systems;
- **Proximity to Earth**. At ~ 12 pc from the Solar System, TRAPPIST-1 is brighter in the infrared than most ultracool M-dwarf stars;
- **Multiplanetary system with frequent transits**. The short orbital period of the TRAPPIST-1 planets results in a higher transit frequency leading to a larger SNR (in particular for the innermost planets);
- **Comparative (exo)planetology studies**. The range of instellation values of TRAPPIST-1 planets is similar to those of Solar System rocky planets, e.g., TRAPPIST-1 c has a similar instellation flux to that of Venus (see Figure 1.2). As multiple planets orbit the same host star, TRAPPIST-1 system is a laboratory for comparative planetology, allowing to study different exoplanetary atmospheres inside and outside the VZ or HZ. Considering that the planets orbit a low-mass star, their evolutionary paths might be potentially very distinct from those of the Solar System rocky planets, providing more cases to test the theories of planetary and atmosphere formation and evolution.

1.2 Overview of the Venus atmosphere

Venus has been known to humankind since before the dawn of Civilisation. It is the brightest object in the sky after the Moon and the Sun. From an astrophysical point of view, Venus has Earth-like parameters: a similar mass, radius and a relative density which might imply a similar structure and bulk composition (Taylor et al., 2018). The two worlds would be astrophysically indistinguishable in the event we were observing them as exoplanets. However, present-day Venus has a much different Climate than Earth's. The Venus atmosphere is carbon dioxide dominated with a global cloud cover of sulphuric acid clouds and a surface atmospheric pressure of 92 bar (Taylor et al., 2018). The high-pressure carbon dioxide is responsible for the potent greenhouse effect on the planet, raising the surface temperature to $\sim 735\ K$ (Lebonnois et al., 2010). In this section, we will overview the characteristics of the Venus atmosphere.

1.2.1 The atmospheric composition

The relative abundances of chemical species present in the Venus atmosphere, compared to their relative abundance in Earth's atmosphere, are listed in Table 1.1. The Venus atmosphere is 96% carbon dioxide and 3% nitrogen. Minor constituents include argon and other noble gases, but also carbon monoxide, water vapour, and sulphur dioxide.

Table 1.1: Comparative chemical composition of the atmospheres of Venus and Earth

Chemical species	**Venus**	**Earth**	**Origin/relevant process**
Carbon dioxide	96 %	400 ppm	Greenhouse gas
Nitrogen	3.5 %	77 %	Similar absolute abundances
Argon	70 ppm	0.93 %	Atmosphere evolution
Neon	5 ppm	18 ppm	Atmosphere evolution
Water vapour	30 ppm	~ 1 %	Volcanic, cloud, greenhouse gas
Sulphur dioxide	150 ppm	0.2 ppb	Volcanic, cloud, greenhouse gas
Carbonyl sulfide	4 ppm	0.5 ppb	Volcanic, cloud
Carbon monoxide	40 ppm	120 ppb	Deep circulation

Note: The chemical species are presented under the form of fractional abundances, except when parts per million (ppm) and parts per billion (ppb) are stated. Data from: Taylor et al. (2018).

Venus atmospheric composition, with a larger abundance of sulphur dioxide than Earth, suggests a volcanic origin. Water is present in the Venus atmosphere in the form of vapour (approximately 30 ppm) and a highly concentrated solution of sulphuric acid in the form of cloud droplets. The total water is 10^5 times lower than in Earth's atmosphere (Taylor et al., 2018). The abundance of minor constituents in the Venus atmosphere is controlled by photochemical cycles associated with radiative and transport processes. For example, carbon monoxide production comes from carbon dioxide photodissociation by ultraviolet (UV) radiation in the uppermost levels of the atmosphere, but the gas will suffer recombination into carbon dioxide at and below the cloud deck, preventing higher relative abundances of carbon monoxide (Gao et al., 2015; Taylor et al., 2018).

1.2.2 Current Climate and thermal structure

Venus and Earth temperature profiles (see Figure 1.4) are similar within their common pressure range. The main difference between the two profiles is the maximum in Earth's stratosphere ($\sim 1\ mbar$), caused by radiative heating from UV absorption in the ozone layer, absent in Venus. Other differences result mainly from the high abundance of carbon dioxide in the Venus' atmosphere and different insolation values between the two planets (Taylor et al., 2018).

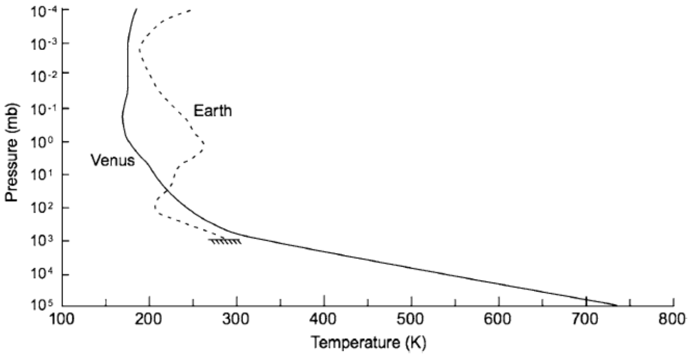

Figure 1.4: Comparative generic temperature profiles for Venus and Earth. Data for Venus is obtained from *Pioneer Venus*, while for Earth is obtained from *Nimbus 7* satellites. The same logarithmic scale is applied to both profiles. Illustration from: Taylor et al. (2018).

In the next points I will summarise the relevant parameters for the thermal structure of Venus:

- **Upper atmosphere**. At $\sim 250\ mbar$ the atmosphere (clouds) becomes optically thick for most infrared (IR) wavelengths. They will radiate almost as perfect blackbody, leading to a global temperature of $\sim 235\ K$. The low water vapour abundance above the clouds, enables transmission for most wavelengths, leading to most of radiant energy to escape to space. The low opacity of the upper atmosphere is interrupted near the **15** $\mu m\ CO_2$ **absorption band** (Limaye et al., 2018);
- **Cloud top**. At $\sim 70\ km$ the temperature is in equilibrium with incoming solar radiation. The planetary bond albedo is 0.77. Despite the insolation being $\sim$ 2-fold that of the Earth, Venus' high albedo explains why the planet absorbs less energy than Earth's (Taylor et al., 2018);
- **Cloud base**, at $\sim 48\ km$, where the atmosphere becomes opaque for most wavelengths;
- **Deep atmosphere**, below the cloud deck, the temperature profile is controlled mainly by convection, following a dry adiabat (lapse rate $\sim 10\ K\ km^{-1}$). Observed dynamical variations have a minor impact in the thermal structure, leading to a stable lower atmosphere. The resulting steady temperature increase from the cloud base to the surface, leads to a high surface temperature of $\sim 735\ K$. The high surface temperature on Venus is primarily due to the high pressure of its atmosphere (Taylor et al., 2018).

Horizontal temperature gradients are small on Venus. However, cloud structure variability, responsible for variations in absorption and emission of radiation, will cause significant horizontal temperature gradients ($\lesssim 10\ K$) inside the cloud deck (Taylor et al., 2018).

1.2.3 The global cloud deck, hazes and radiative balance

The Venus cloud system is the most complex and extensive one among rocky Solar System planets. Atmospheric complexity arises from the close interaction between gases chemistry and photochemistry processes. Overall, the planet has a global cloud cover between altitudes $\sim$ **48** km to $\sim$ **70** km. Below and above the cloud deck, lower and upper hazes extend, respectively, to about 30 km and 100 km (Titov et al., 2018). The average (planetary) cloud top altitude is set between 72 km and 74 km by several authors as Ignatiev et al. (2009); Limaye and Rengel (2013); Limaye et al. (2018). Garate-Lopez and Lebonnois (2018) describe a latitudinal variation in cloud top altitude ranging from 71 km at equator, decreasing down to 70 km at 50° N/S and 61 km at the poles. The main cloud components are photochemically-produced sulphuric acid aerosols, solid sulphur, and an UV absorber of unknown origin. The main regions of the cloud and haze system are, from top to base:

- **Upper haze**. Occupying almost the entire mesosphere from $\sim$ 100 km to the cloud top;
- **Cloud top**. The altitude of vertical optical depth for the visible wavelengths. The cloud top altitude latitudinally varies from $\sim$ 71 km at equator to $\sim$ 61 km at the pole (Ignatiev et al., 2009);
- **Upper cloud layer**. The upper cloud layer has its physical base on the tropopause;
- **Middle and lower cloud layers**. Convection-dominated region, which base is located at 48-50 km for low and middle latitudes and possibly below 45 km for the polar regions (Barstow et al., 2012; Tellmann et al., 2009). The lowest, densest, physically thin (1 - 2 km) layer harbours the largest radii and highest concentration of particles, accounting for most of the total column optical depth in the atmosphere. These are likely wind-blow mineral dust, solid particles from volcanic origin;
- **Cloud base**. Level where the sulphuric acid becomes *thermodynamically unstable*, i.e., the temperature becomes higher than the evaporation point of sulphuric acid;
- **Lower haze**. A more tenuous layer extends from the cloud base down to $\sim$ 30 km, where the temperature is too high for sulphuric acid to be in the liquid form. Below the lower haze, there is indication of a near-surface haze.

1.2.4 Circulation and general dynamics of the Venus atmosphere

The Venus atmosphere is characterised for two main dynamical regimes:

- **Retrograde zonal superrotation** (Read and Lebonnois, 2018): dominant from the surface to $\sim$ 70 km altitude. The wind is directed *westwards* and its speed increase from the surface to the cloud top level, reaching speeds $\mathcal{O}$ (100 $m\,s^{-1}$) at the equator. An air parcel at the equator would encircle the planet in four/five Earth days, sixty times faster than the solid-body rotation (hence, "superrotation"). In the mid-latitudes (40° - 60° N/S) there is a jet with speeds reaching $\sim$ 120 $m\,s^{-1}$ at the cloud top (Lebonnois et al., 2010). The study of the retrograde zonal superrotation on Venus comes from cloud tracking at the highest cloud layers and the Doppler shift of solar backscattered radiation at the cloud tops. Zonal wind deceleration occurs above and below the cloud layer. Above the cloud tops, zonal wind deceleration results from the temperature-driven pressure gradient, particularly because mid atmosphere temperature is $\sim$ 20 K warmer at the pole compared to the equator. Below the clouds, atmospheric drag becomes more intense, and the winds tend to zero at the surface.
- **Solar to antisolar circulation** (Clancy et al., 2015): dominant for altitudes above 110 km which is caused by the day-night temperature gradient originating in the absorption of short-wavelength radiation in the dayside. It reaches speeds of $\sim$ 300 $m\,s^{-1}$.

Due to the particular importance of the zonal superrotation has in the energy redistribution of possible Venus-like exoplanets we will address the particular dynamics in the next section.

1.3 Principles of Planetary Climate: from the theory to modelling

1.3.1 Basic parameters of the Climate System

Climate systems are complex systems where the interaction between their subsystems may lead to non-linear outcomes. It is possible to break down the basic coupled physical and dynamical planetary processes in the control of the Climate system, as shown in Figure 1.5.

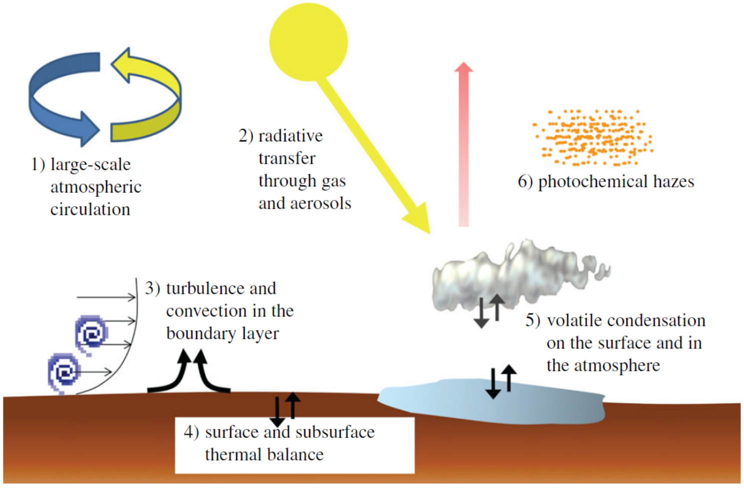

Figure 1.5: Basic physical and dynamical processes controlling the Climate System for a rocky planet. Illustration from: Forget and Leconte (2014).

While several physical processes influence the planetary atmosphere behaviour, a limited number of basic coupled physical and dynamical processes control the Climate System (Forget and Leconte, 2014):

(1) The **general circulation of the atmosphere**, primarily driven by large-scale temperature gradients caused by the radiative forcing. The *Navier-Stokes* equations describe the air parcel motions;

(2) The **radiative transfer** equations that describe stellar (short wavelength) and thermal (long wavelength) radiation interaction (absorption, emission, scattering processes) with the planetary surface and wavelength-dependent opacity media, such as clouds (aerosols) and gases;

(3) **Vertical mixing and boundary layer atmospheric processes** from small-scale turbulence and convection;

(4) **Heat storage** in the planetary subsurface through conduction;

(5) **Phase transition of condensable species**, described by thermodynamic equations, on the surface and in the atmosphere through the means of clouds and aerosols - where the cloud formation and evolution is described with microphysics;

(6) **Photochemistry processes** as drivers for aerosol, cloud, and haze production and modification. In specific cases, the photochemistry processes might have a pivotal role in the creation of spatial and time inhomogeneities in the atmospheric composition. These photochemistry processes are described through chemical/photochemical kinetic equations.

Depending on the planet, other physical and dynamical processes can become relevant to describe the Climate. For example, dust-related processes are essential for Mars, while oceanic heat transport is crucial to the Earth's Climate (or Earth-like exoplanets). These coupled physical and dynamical processes can define *multiple* climates, especially when considering a particular set of planetary and orbital parameters and atmospheric composition (Forget and Leconte, 2014). These parameters include the mass and radius (thus the surface gravity), rotation rate, instellation and host star spectral type.

The **planetary rotation rate** is relevant for its impact in the large-scale atmosphere dynamics and thermal structure (Heng and Showman, 2015). The rotation rate determines the magnitude of *Coriolis* and centrifugal forces, controlling the *Hadley* cell extension, the emergence of extratropical or equatorial superrotation jets, and the type of planetary waves present (Forget and Leconte, 2014; Read, 2011). The contribution from rotation to the planetary Climate can be quantified by the **Rossby Number**, Ro:

$$Ro = \frac{U}{fL} \tag{1.1}$$

Where U represents a characteristic horizontal wind speed scale, f is the *Coriolis* parameter, and L is a characteristic horizontal length scale([11]) of the flow. The magnitude of Ro defines the dynamical regime: when $Ro \ll 1$, the rotation effects are relevant to the large-scale circulation, while for $Ro \sim 1$, the rotation has a mild impact in the large-scale circulation (Showman et al., 2013).

In a simple manner, a planet can be classified according to its rotation rate into **fast rotator** (e.g., Earth, Mars) or **slow rotator** (e.g., Mercury, Venus, Titan). In some cases, tidal forces can lead to an extreme configuration of planetary rotation: a **synchronous rotator**. Synchronous rotators (or tide-locked planets) are worlds in which tidal stresses from the gravitational gradient field from a much more massive body (star or planet) progressively and steadily force the rotation period to equalise the orbital period. This case should be the most likely scenario for the rotation rate of close-in highly-irradiated planets around M-dwarf stars.

1.3.2 The Climate of synchronous rotators

The synchronous rotation leads to the *disappearance* of the diurnal cycle, as the same hemisphere *always* faces the host star. Synchronous rotators have permanent dayside and nightside hemispheres, and the stellar energy available for the Climate system will be limited to the permanently-irradiated dayside hemisphere. If an atmosphere is present, atmospheric dynamics are controlled by the installation of a strong **day-night heating contrast**. This thermal gradient will drive zonal and meridional winds, and the large-scale circulation will transport heat from the dayside to the nightside. Hence, energy redistribution between hemispheres will be governed by horizontal heat transport from advection and waves. Furthermore, tidal forces that lead to the synchronous rotation will reduce planetary obliquity, impacting the latitudinal distribution of instellation and the seasonal cycle, reducing the stellar energy available to the polar regions (Forget and Leconte, 2014). Due to orbital evolution, these worlds are likely to have very low orbital eccentricities, minimising instellation variation along the year (Heng and Showman, 2015; Hut, 1980; Pierrehumbert and Hammond, 2019).

Two characteristic timescales support an estimate for the magnitude of the day-night temperature contrast (Cooper and Showman, 2005; Cowan and Agol, 2011; Heng et al., 2011a,b; Perna et al., 2012; Showman and Guillot, 2002; Showman et al., 2008):

- **Advection timescale**, t_{adv}, over which the air advects from the dayside to nightside;
- **Radiative timescale**, t_{rad}, over which the air gains or loses energy from absorbing short-wavelength stellar irradiation and infrared energy.

---

[11] A characteristic order of magnitude for L is the one that better represents the large, planetary-scale flow, on the order of the planetary radius $\mathcal{O}\,(10^6\ m)$.

The fractional day-night temperature difference is large when $t_{rad} \ll t_{adv}$. When the two characteristic timescales have the same order of magnitude, $t_{adv} \sim t_{rad}$, the transition from small to large fractional day-night temperature occurs (Perna et al., 2012), and the winds can reshape the temperature field, *eastward* moving hot spots (peak thermal emission regions) from the substellar point to the evening terminator region (Showman and Guillot, 2002). The condition also predicts the occurrence of an equatorial eastward superrotation jet (in the same direction as the planet's spin). Thus, the main characteristics of the global circulation of synchronous rotators are, as suggested by modelling work:

- **Equatorial eastward jet**, dominant feature in simulations of hot Jupiters (warm close-in gas giants) and rocky planets, appearing as a fast, broad eastward-flowing equatorial jet (Cooper and Showman, 2005, 2006; Dobbs-Dixon and Lin, 2008; Dobbs-Dixon et al., 2010, 2012; Hammond and Pierrehumbert, 2018; Heng et al., 2011a,b; Lewis et al., 2010; Perna et al., 2012; Rauscher and Menou, 2010, 2012; Showman and Guillot, 2002; Showman et al., 2008, 2009, 2013). Often termed as a **superrotation** jet because of the larger angular momentum per unit mass of the atmospheric flow compared with the angular momentum of the planet's solid-body at the equator (Pierrehumbert and Hammond, 2019). In our Solar System, Venus (Gierasch, 1975; Read, 1986) and Titan (Mitchell and Lora, 2016) atmospheres are in superrotation(12).

  The emergence of superrotation is likely associated with planetary-scale *Rossby* and *Kelvin* wave modes, driven by the strong day-night temperature gradient . These wave modes are trapped in the equatorial region, i.e., their propagation is *exclusively* zonal, with the Kelvin wave located at the equator and two Rossby waves located at its poleward flanks. These baroclinic wave modes exhibit a **differential zonal group propagation**, with the Kelvin wave group directed eastward and the Rossby's westward. The latitudinal varying zonal propagation caused by these wave modes will generate an eddy velocity pattern, tilting northwest-southeast (northern hemisphere) and southwest-northeast (southern hemisphere). This eddy velocity pattern drives an **equatorward eddy angular momentum flux** from higher latitudes to the equator, allowing for an angular momentum convergence: the forcing mechanism behind the equatorial superrotation (Heng and Showman, 2015; Showman and Polvani, 2010, 2011; Tsai et al., 2014).

- **High-latitudes eastward jets**, in some cases when the superrotation is present and there is a fast, but synchronous rotator, there is an emergence of additional eastward mid-latitudes (or high-latitudes) jets (Kataria et al., 2013; Showman et al., 2008, 2009).

- **Chevron-like feature** (for example, present in temperature field) with an orientation southwest-northeast (northern hemisphere) and northwest-southeast (southern hemisphere) (Heng and Showman, 2015).

- **Mean-meridional circulation** whose intensity and depth of the cells depend on the instellation, with more irradiated planets having stronger and deeper cells (Perna et al., 2012).

- **Hotspot eastward offset** is a consequence of the advection of warm air masses from the substellar region by the intense equatorial zonal superrotation jet. The extent of the hotspot eastward offset is variable (Hammond and Pierrehumbert, 2018; Showman and Guillot, 2002).

- **Rossby lobes**, a pair of cold-core low-pressure regions located west of the substellar point in the nightside hemisphere. Their location is symmetrically disposed around the equator, on both the

---

[12] The tropospheres of Earth and Mars show a subrotation feature, the mean westward equatorial flow.

northern and southern hemispheres, peaking in the mid-latitudes. They can be an effect from the equatorial zonal superrotation jet (Pierrehumbert and Ding, 2016; Turbet et al., 2016).

Describing the Planetary Climate of worlds with such different dynamical features requires the usage of **Climate models**, complex numerical codes designed to consider as many of the physical processes described above with the highest accuracy degree possible. All the Climate processes described can be included in models with the support of numerical schemes and parametrisations that include a certain number of coupled differential equations (Forget and Leconte, 2014).

1.3.3 Climate Models for exploring planetary Climate

Climate models were initially developed to study the Earth's Climate (e.g., anthropogenic Climate Change). However, Solar System exploration and exoplanetary detections led to the adaptation of these Earth-based models to study possible exoplanetary atmospheres.

The models used in Figure 1.2 to limit the HZ and VZ are simple one-dimensional (1D), steady-state radiative-convective Climate models. They offer a first approximation to the kind of expected Climate, providing an evaluation of the influence of the atmospheric radiative properties in the global mean parameters such as temperature (Kasting et al., 1993; Kopparapu, 2013b; Kopparapu et al., 2013a). However, 1D Climate models cannot represent the radiative impact from spatially variable transient features like clouds. Similarly, 1D Climate models do not represent seasonal and diurnal cycles or planets with a strong day-night temperature gradient. Thus, to adequately estimate the instellation regime and global energy redistribution by the atmosphere (or ocean), a spatial and time representation of dynamical and physical processes on a spherical three-dimension (3D) are required, hence the need for a 3D Global Climate Model (GCM).

A 3D GCM is composed of a series of columns representing a physical system (e.g., atmosphere, ocean) connected through a 3D (hydro)dynamical core. The model's dynamical core links the columns through 3D fields of horizontal mass and energy transports carried by wind (or ocean currents). The dynamical core is the foundation of any 3D GCM, for it solves the *Navier-Stokes* equations for fluid dynamics on a rotating sphere envelope. Additionally, at each model grid-point, physical variables are prognostically calculated by dedicated physical parameterisations. The range of physical processes treated by these parameterisations depends on the model's desired level of detail. However, some model routines can be considered pivotal for representing the Climate System, like the radiative transfer, which describes how stellar and thermal energy interact with atmospheric constituents at each level, or the turbulence and convection parametrisation.

The description of atmospheric dynamics, cloud systems, and complex 3D temperature variations are not feasible to prognostic without the range of physical interactions enabled by 3D models. These traits make 3D GCMs exceptionally well placed for exoplanetary Climate studies and to predict the kind of observables we might expect from a planet. Conversely, 3D GCMs can be computationally demanding with simulations running on computer clusters. The 3D GCMs are sophisticated Climate models that build upon large teams' expertise and years of development.

1.3.4 The 3D LMD Generic Global Climate Model

This work uses a 3D GCM, the Generic Global Climate Model (Generic-GCM) developed by the *Laboratoire de Météorologie Dynamique* (LMD), *Institut Pierre-Simon Laplace* (IPSL) (Paris, France), to simulate Venus-like exoplanetary atmospheres around M-dwarf stars, using the planetary parameters of

TRAPPIST-1 c as a benchmark. The Generic-GCM derives from the LMDz Earth GCM (Hourdin et al., 2006), a second-generation GCM developed at IPSL-LMD. The model has been used in several studies to simulate a diversity of climates with a wide insolation range. In the Solar System, the Generic-GCM has been used in paleoclimate studies of Earth's archean (Charnay et al., 2013), early Mars - the case of a low-irradiated planet (Forget et al., 2013; Kerber et al., 2015; Turbet et al., 2017a, 2020b; Wordsworth et al., 2013, 2015), or early Titan (Charnay et al., 2014).

The model has also been successfully used to simulate the vast diversity of exoplanetary climates, from low irradiated planets like exoplanet Gliese 581 d (Wordsworth et al., 2011), to exoplanets with similar Earth-like instellations (Bolmont et al., 2016; Turbet et al., 2017b) - in particular, the closest Earth-like exoplanet to our Solar System, Proxima Centauri b (Turbet et al., 2016). The Generic-GCM has also been used to simulate the Climate of highly-irradiated planets, e.g., future Earth (Leconte et al., 2013b), and those of synchronous rotators, like exoplanet Gliese 581 c/HD 85512 b (Leconte et al., 2013a). Many of these studies have focused on the Earth-like climates, studying the HZ and its evolution (Leconte et al., 2013a,b; Turbet et al., 2020b; Wordsworth et al., 2011). Of relevant importance for this work is the study led by Turbet et al. (2018a), which uses the Generic-GCM to simulate the Climate diversity of TRAPPIST-1 planets, including the highly-irradiated TRAPPIST-1 b and c planets.

Dynamical core and physical part of the model The Generic-GCM is composed of a dynamical and physical part, coupled through a common interface.

- The **dynamical core**: responsible for solving the primitive equations of geophysical fluid dynamics by integrating them in time over the 3D sphere grid covering the entire planetary atmosphere. This part provides the numerical solution of the general equations for atmospheric circulation. The dynamical core is the same as in the LMDz Earth GCM and counterparts that simulate the atmospheres of other Solar System bodies Venus (Lebonnois et al., 2010), Mars (Forget et al., 1999), Titan (Lebonnois et al., 2012) or Pluto (Bertrand and Forget, 2016, 2017; Bertrand et al., 2020; Forget et al., 2017)([13]). The calculations for this dynamical part are made on a 3D spherical grid, and horizontal exchanges between the grid boxes are allowed.
- The **physical part**, planet-specific, is responsible for the calculation of the circulation forcing and climatic parameters on each grid point. The physical code is written as a juxtaposition of 1D columns, with each column independent of the neighbouring one. The physical part includes routines for radiative transfer, tracer transport or evolution, and surface-atmosphere interactions.

Model grid The model grid discretisation is made in the horizontal and vertical directions. The grid boxes in the model have typical horizontal values such as 64 per 48 or 32 per 24 in longitude and latitude. The grid box size is dependent on the planetary radius, which the user can modify. For the vertical direction, hybrid σ - p coordinates are used, with a gradual transition from σ coordinates near the surface to pressure p coordinates in the upper levels of the atmosphere.

The radiative transfer in the Generic-GCM The radiative transfer routine in the Generic-GCM (Richard et al., 2012; Wordsworth et al., 2010) is historically based on the NASA Ames radiation code (Wordsworth et al., 2010), which supports variable atmospheric compositions. In addition, it uses the correlated-k model, which enables fast calculations of opacities (Eymet et al., 2016; Fu and Liou, 1992). The radiative transfer considers the absorption/emission by aerosols, gases, and clouds at any altitude,

---

[13] Under specific conditions, the dynamical part applies to the upper atmospheres of gas giant planets.

from the far-infrared to the visible, together with the radiative scattering from clouds and the Rayleigh scattering.

The method consists in calculating k-coefficients from high-resolution absorption spectra computed by `kspectrum` (a line-by-line model available online at http://www.meso-star.com/en_Products.html), using the HITRAN 2012 database (Rothman et al., 2013). The details on how those coefficients are pre-calculated and stored in a matrix of temperature and log-pressure grid are in the PhD thesis manuscript of Martin Turbet (Turbet, 2018b). In practice, the method converts a high-resolution spectrum into a distribution of absorption (also called “k-distribution”) expressed as a cumulative probability function. In other words, we assume that the absorption can reach a set of different values, each associated with a different probability. The benefit of using correlated-k coefficients is having a smaller database of coefficients for the model, enabling a faster computation time - a relevant asset, given that radiative transfer often has a heavy computational burden.

1.4 Atmospheric observation methods

This subsection introduces the theory behind the observables produced in this work: the phase curves (reflection and emission) and transmission spectra. These observables will be used to interpret the thermal structure, large-scale atmospheric circulation, and chemical composition of the simulated Venus-like exoplanetary atmosphere.

1.4.1 Phase Curves

A phase curve represents the temporal flux variation incoming from an astronomical object (e.g., planetary brightness) throughout different orbital phases (Parmentier and Crossfield, 2018). Typically, the phase curve presents the exoplanetary brightness or the ratio of planetary flux to stellar flux (planet-to-star contrast) as a function of the orbital phase (see the red dashed curve in Figure 1.6).

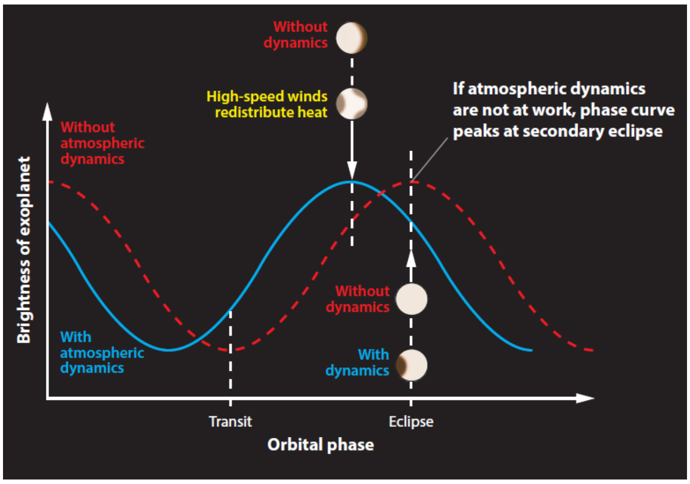

Figure 1.6: The efficiency of the high-speed (superrotation) wind system will favour heat redistribution among specific geographical patterns. The red dashed curve represents the case of absent atmospheric dynamics, where the substellar point is simultaneously the point of largest incident flux and thermal emission to space. The solid blue curve represents a scenario where atmospheric dynamics leads the peak of thermal emission to be shifted eastwards, imprinting a signature in the phase curve where the peak emission happens before the eclipse. In a planet whose orbit is edge-on to Earth, the eclipse corresponds approximately to the point where the substellar point is directly facing the Earth and the transit corresponds to the point where the antistellar point is directly facing the Earth. Illustration from: Heng and Showman (2015).

The planetary flux in the phase curve is disk-integrated, depicting a series of subsequent longitudes and is convoluted with its geometric projection to the observer. Thus, the phase curve is the best observational technique to characterise the longitudinal structure of an exoplanet (Cowan and Agol, 2008; Parmentier and Crossfield, 2018).

The planetary brightness results from the combination of reflected stellar light and thermal emission from the planet (Crossfield, 2015; Heng and Showman, 2015; Parmentier and Crossfield, 2018). Several phase curves from different spectral bands provide the best possible planetary atmosphere representation.

The reflected stellar light is the dominant component of the planetary brightness in the visible. Thus, reflection phase curves convey information on the longitudinal variation of planetary albedo, and they constrain the aerosols' relative abundances and size (Demory et al., 2013; Heng and Demory, 2013).

The planetary thermal emission dominates over the stellar contribution in the infrared. Therefore, the thermal phase curve provides information on the longitudinal variation of the temperature field and chemical composition (Parmentier and Crossfield, 2018). Furthermore, measurements in several spectral bands will allow the exploration of different atmospheric levels with different thermal phase curves, enabling the possibility of interpreting physical processes that might occur at different levels and the construction of 3D temperature fields (Heng and Showman, 2015).

Phase curves are the observational method that is best fit to study and probe the 3D structure of an exoplanetary atmosphere (Parmentier and Crossfield, 2018). Phase curve observations can provide important information about planetary atmosphere dynamics and energy when inverted to yield the longitudinal (i.e., latitudinal-mean) brightness temperature maps. These maps help constrain atmospheric properties at the planetary surface or cloud tops, in the region of thermal and reflected light opacity (Cowan and Agol, 2008; Crossfield, 2015; Heng and Showman, 2015).

Two parameters are fundamental when interpreting the information contained in a phase curve: the **amplitude** and the **orbital phase of maximum planet-to-star contrast**. The first level of longitudinal variability in the planetary brightness comes from the variation of the illuminated fraction of the planet's Earth-facing hemisphere. The resulting longitudinal temperature differences are first explained by the existence of a warmer and brighter dayside hemisphere and a colder and dimmer nightside hemisphere (Parmentier and Crossfield, 2018). These temperature differences establish the **amplitude** of the phase curve. Planets with a large day-night temperature contrast experience high-amplitude thermal phase curves. Conversely, small day-night temperature gradients can lead, in the limit, to a flat thermal phase curve. In this sense, highly-irradiated exoplanets are expected to have larger thermal phase curve amplitudes (Perez-Becker and Showman, 2013).

The second relevant parameter in the analysis is the **orbital phase peak emission** and the possibility of a longitudinal offset of peak emission with respect to the substellar point (see blue curve in Figure 1.6). If atmospheric dynamics are not relevant, the peak emission occurs at the secondary eclipse, the orbital phase where the planet's Earth-facing hemisphere is fully illuminated (see the red dashed curve in Figure 1.6). However, if atmospheric dynamics are relevant, they could be responsible for advecting warm air masses from the substellar point in the direction of the nightside hemisphere. The resulting energy redistribution in the atmosphere could lead to an eastward shift of the peak emission. In this scenario, the corresponding thermal phase curve maximum will occur before the secondary eclipse, as suggested by the blue thermal phase curve in Figure 1.6 (Crossfield, 2015).

The modulation of a phase curve is a proxy for atmospheric thermodynamics, as they are related to factors such as the atmosphere radiative, advection and drag timescales and heat redistribution by the wind field. For example, suppose the radiative timescale is low. In that case, the absorbed stellar irradiation is immediately reradiated to space through thermal emission. As a result, the warmest region is the one that receives the largest stellar incident flux, i.e., the substellar point. In this scenario, the thermal phase offset becomes negligible, which could also be the case of a planet without an atmosphere. In opposition, if the advection and radiative timescales are similar, the atmospheric dynamics will be responsible for an eastward displacement of the maximum thermal emission from the region of the substellar point in the direction of the evening terminator. The presence of a superrotation equatorial jet is appointed as the most likely dynamical explanation for the hotspot eastward shift (Showman and Guillot, 2002) and has already been observed for exoplanet HD 189799 b (Knutson et al., 2007, 2008, 2012), and other hot Jupiters (Crossfield et al., 2010; Lewis et al., 2013; Zellem et al., 2014). Moreover, the eastward shift of the hotspot has been predicted theoretically before its detection (Showman and Guillot, 2002). Since then, the feature has been successfully reproduced in GCM simulations (Cooper and Showman, 2005; Dobbs-Dixon and Lin, 2008; Heng et al., 2011a,b; Mayne et al., 2014; Perna et al., 2012; Showman et al., 2009).

Therefore, a thermal phase curve offset indicates heat redistribution is present on the planet. A large offset could suggest strong advection from superrotation jets or drag forces or be related to frontal regions of shock-like features (Cowan and Agol, 2010; Heng, 2012; Perez-Becker and Showman, 2013).

1.4.2 Transmission Spectroscopy

The atmospheric characterisation is also possible from planets transiting their host stars, favouring larger planets in close-in, edge-on orbits (Brown, 2001; Seager and Sasselov, 2000). From the Earth's perspective, the **transit** or primary eclipse occurs when the planet passes in front of the host star, blocking part of the incoming stellar light due to the opaque planetary disk. When the planet passes behind the star, the event is called a **secondary eclipse**. Figure 1.7 presents the orbital geometry of a transiting planet.

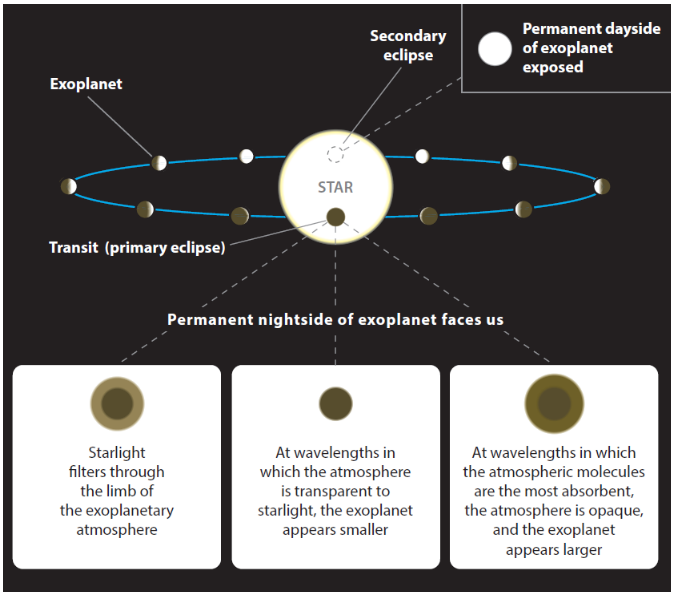

Figure 1.7: From the Earth's perspective a nearly edge-on planet will cross its host star disk in an event called a transit (primary eclipse). When the planet passes behind the host star, the event is called a secondary eclipse. Illustration from: Heng and Showman (2015).

The information on the exoplanet's atmosphere is retrieved by measuring the incoming flux before, during, and after the transit. The reduction on the stellar flux can be used to estimate the planet's radius. If the planet has an atmosphere, the stellar light will be transmitted through the atmosphere in the planetary limb. The transmitted stellar light at planet's terminator region is measured across multiple wavelengths providing information on how atmospheric absorption and scattering vary according to the wavelength (Encrenaz, 2014; Heng and Showman, 2015). The different chemical species, dust and aerosols present in the atmosphere will modify the transmission, making the atmosphere more transparent or opaque for different wavelengths. Since atmospheric opacity is wavelength dependent, the exoplanet effective radius will vary with wavelength (Brown, 2001; Hubbard et al., 2001; Seager and Sasselov, 2000). At wavelengths where the stellar radiation is absorbed or scattered by atmospheric constituents the atmosphere becomes opaque and the exoplanet's effective radius appears larger. Conversely, at wavelengths where the atmosphere is transparent to stellar light, the radiation passes through the atmosphere and the exoplanet's effective radius will appear smaller (see Figure 1.7). The decrease in the stellar flux is thus measured across multiple wavelengths, creating the **transmission spectrum**, presented in **relative transit depth**, which compares the atmosphere signal to the solid body. The **relative transit depth** (ppm) of the atmosphere following Lincowski et al. (2018) (valid only for atmospheres with small scale height) is:

$$\frac{\mathrm{d}F_a}{F} \approx 2\frac{R\,R_a}{R_*^2} \tag{1.2}$$

Where R is planet's radius (solid-body), R_a the atmosphere's vertical extent and R_* is the radius of the star. The transmission spectrum can be used to infer the atmospheric composition by identifying different absorption spectral features that can be related to atomic and molecular species in the atmosphere (Heng and Showman, 2015).

The study of exoplanetary atmospheres with transmission spectroscopy has evolved to characterise smaller mass exoplanets with a gradually denser wavelength coverage. The method was applied to identify alkali metals in the atmosphere of hot Jupiters. It enabled the first detection of an exoplanetary atmosphere, with the detection of Na I in the visible light by Charbonneau et al. (2002). Given the high dayside temperatures typical of this exoplanet class (1000 - 2000 K), they are in the gas phase and are extremely absorbing at specific absorption lines in the visible wavelengths (Seager and Sasselov, 2000). Detection of chemical species more familiar to the range of temperatures seen in terrestrial planets, like water, carbon monoxide, carbon dioxide, or methane, is far more challenging (Heng and Showman, 2015). To identify these molecular species, measurements must be made in the near-infrared part of the electromagnetic spectrum (Swain et al., 2008; Tinetti et al., 2007), typically between 1 - 5 μm (Heng and Showman, 2015). However, water vapour has been successfully detected in the transmission spectrum of hot Jupiters (Kreidberg et al., 2015; Sánchez-López et al., 2019; Tinetti et al., 2007), and a water vapour breakthrough detection was made more recently for a Super-Earth planet orbiting the habitable zone of an M-dwarf star (Tsiaras et al., 2019). Equally relevant to detecting chemical species is the intriguing detection of flat or relatively flat transmission spectra on some exoplanets. The existence of high altitude hazes or clouds has been advanced as a likely explanation. Hazes and clouds will raise the opacity level and have an efficient scattering at a wide range of wavelengths, screening spectral features from atmospheric constituents (Knutson et al., 2014; Kreidberg et al., 2014). The evidence for atmospheric haze was derived from the visible transmission spectrum (Pont et al., 2008).

1.5 Motivation and Opportunity

The objective of Exoplanetary Science is the detection and characterisation of other worlds in other Planetary Systems. The ultimate aim is to find an Earth-like planet. A series of intermediate steps are necessary for this quest as *in situ* exploration of these worlds is beyond current Humanity's technological capabilities. Following the first exoplanet discoveries, Exoplanetary Science has had an astrophysical approach by developing and improving methods and techniques for exoplanet detection and characterisation in terms of their orbital parameters, mass and radius. The progressive developments, namely in instruments' resolution, allowed Exoplanetary Science to start answering research questions related to these worlds' atmospheres and climates. This characterisation started with the "highly-irradiated"(14) gas giants, whose large surface area and close-in orbits offer a more favourable observing geometry. Next-generation observatories will gradually extend this characterisation to include small, rocky exoplanets in short orbital periods. Data from observations will focus on planetary spectroscopy and time measurements of the planetary flux and its ratio over the stellar flux, i.e., the planet-to-star contrast.

Dedicated atmosphere observations of rocky exoplanets have already been conducted by the *Hubble Space Telescope* (HST) (e.g., de Wit et al. (2016, 2018)). Furthermore, the launch of the *James Webb Space Telescope* (JWST) on December 25th, 2021, will greatly advance the atmosphere and Climate characterisation of nearby rocky exoplanets, given its larger resolution and survey in the near-infrared (NIR) part of the electromagnetic spectrum (Bean et al., 2018). This characterisation will continue to advance and deepen with upcoming dedicated missions in the next decade, such as the European Space Agency's (ESA) Ariel mission, along with future ground-based telescopes such as the *European Extremely Large Telescope* (E-ELT) and the *Thirty Meter Telescope*.

Present and future missions will produce many observations, including reflection, emission phase curves and transmission spectra. The expected vast amount of data will pose a significant *challenge* but also a unique opportunity. It will open the atmosphere and Climate characterisation to more rocky exoplanets, expanding comparative planetology and allowing for a comprehensive understanding of the diversity of worlds (Leconte et al., 2015a).

Nonetheless, the adequate characterisation of these worlds' climates and atmospheres will remain a challenging task. Moreover, in the face of the vast array of observational data, the community must identify and prioritise targets for the follow-up observations (Kempton et al., 2018). Permanent support from theoretical atmospheric modelling studies is necessary for data interpretation. Furthermore, the production of synthetic observables is crucial to support observation proposals and more efficient use of the highly competitive telescope time.

Three-dimensional Global Climate Models (3D GCMs) are particularly fit to meet the challenge of describing the diversity of exoplanetary climates. The top-of-the-atmosphere fluxes produced by these models are critical to interpreting the observable signal modulation. These fluxes can be disk-integrated as a function of the orbital phase and Earth-facing hemisphere. The spatial and time variability of the disk-integrated flux will reflect the atmospheric variability of the simulated temperature and wind fields, providing insight into the large-scale atmospheric circulation. The outputs can also be used to produce transmission spectra, which will characterise the atmospheric composition in different layers.

The advances in the field will also benefit from the synergies with the Solar System planets. For example, with similar mass, radius, and bulk compositions, Venus and Earth would be astrophysically indistinguishable in the event we observe them as exoplanets. However, despite astrophysical based similarities, both planets have experienced a divergent atmosphere evolution. The factors behind the development and maintenance of this atmospheric divergence are *unknown*. Additionally, most rocky exoplanets are highly-irradiated worlds, probably rather Venus-like than Earth-like climates. Therefore, these exoplanets are the most favourable targets for atmospheric characterisation studies, meaning that

---

[14] We will use the terminology highly-irradiated to describe a planet whose instellation is larger than Earth's insolation.

the first exoplanetary atmospheres to be studied will be those of Venus analogues (Kane and von Braun, 2008). The survey of Venus-like atmospheres and their inherent diversity might contribute to understanding the Climate divergence between Earth and Venus and the conditions for long-term surface habitability.

1.6 Objectives

This Master Dissertation aims to study the large-scale atmospheric circulation of highly-irradiated exoplanets. The selected atmosphere is Venus-like, carbon dioxide dominated, with a 92 bar surface pressure. I will address the observational prospects by producing phase curves (reflection and emission) and transmission spectra to support future space missions (e.g., JWST). This work is a modelling study which uses the Generic Global Circulation Model (Generic-GCM), initially developed by the IPSL-LMD and continuously improved thanks to the efforts of several European teams. The objectives established for this work are:

- **To characterise the thermal structure, radiative balance, large-scale atmospheric circulation of the reference exoplanet TRAPPIST-1 c simulated with a Venus-like atmosphere and clouds**. To describe the thermal structure and compare it to that of Venus. To determine the radiative tendencies and the main aspects of the global circulation (zonal and meridional). Emphasis will be given to the cloud top level temperature and wind fields for their relevance to observational prospects, namely the reflection and emission phase curves.

- **To develop and analyse synthetic observables of TRAPPIST-1 c: reflection and emission phase curves and transmission spectra in the perspective of addressing future observational prospects**. To produce `Python` routines to create synthetic observables based on model outputs, followed by their analysis and contribute to understanding the planet's thermal structure and large-scale atmospheric circulation aspects.

- **To study the impact of removing Venus-like clouds in the TRAPPIST-1 c atmosphere's thermal structure, large-scale circulation and synthetic observables**. The objective is to evaluate the impact of Venus-like aerosols on the atmosphere of TRAPPIST-1 c and its observational prospects.

- **To study the impact of varying planetary parameters under mass-radius relationships and higher-order spin-orbit resonances in the atmosphere's thermal structure, large-scale circulation and synthetic observables**. The study of the influence of mass-radius relationships and different planetary rotation rates on the atmosphere's thermal structure and large-scale circulation, together with the reflection and emission phase curves production and interpretation, represents a first step towards a more extensive parametric study.

This Master Dissertation ultimate goal is to contribute to the building a *grid of possible Venus-like exoplanets*, in which the Generic-GCM can be used to explore a diversity (or a specific set when required) of parametric combinations that will be used to interpret and support future observations.

1.6.1 Dissertation Organisation

This dissertation is organised in the following sections:

- Chapter 1: **Introduction** provides theoretical background and reviews the literature starting from the increasing body of evidence of possible Venus-like exoplanets with a promising population of nearby exoplanets available for atmospheric characterisation. The section introduces TRAPPIST-1 system as an exceptional system for atmospheric characterisation with TRAPPIST-1 c being currently one of the best targets for atmospheric characterisation studies. An introduction to 3D Climate modelling is done, focusing on the Generic-GCM developed by the IPSL-LMD.

- Chapter 2: **Methodology** introduces the *rationale* behind the modelling work with the Generic-GCM, from modelling Venus orbiting the Sun to modelling a Venus-like exoplanetary atmosphere using TRAPPIST-1 c planetary parameters and TRAPPIST-1 stellar spectra as templates for a benchmark possible Venus analogue orbiting an M-dwarf star. The presentation of the numerical scheme needed to address the long convergence times of the deepest layers is also introduced and discussed. The considerations on the particular nature of the parametric tests: mass-radius relationships and higher-order spin-orbit resonances are also presented here. A presentation of the synthetic observables produced with this work including the *Python* script created to compute the reflection and emission phase curves (see **Appendix II**), as well as the usage of the `Planetary Spectrum Generator` (Villanueva et al., 2018) to compute the transmission spectra of TRAPPIST-1 c with Venus-like clouds and clear-sky conditions are presented here.

- Chapter 3: **Results**. The section presents the results for the different simulations with particular focus on TRAPPIST-1 c modelled as a synchronous rotator and with Venus-like clouds, similar surface atmospheric pressure (92 bar) and atmospheric composition. The results focus on presenting, analysing and discussing the thermal structure, radiative tendencies, large-scale atmospheric circulation but also the synthetic observables. The results proceed to the analysis of the clear-sky conditions on TRAPPIST-1 c, on how removing Venus-like aerosols impacts the large-scale circulation and the observables. The final subsection is the parametric study (planetary radius and surface gravity variation following a mass-radius relationship and 3:2 and 2:1 spin-orbit resonances).

- Chapter 4: **Conclusions and Final Remarks**. The section summarises the main conclusions of this work and presents final remarks which include a personal reflection over the objectives attained in the course of this Master Dissertation.

- Chapter 5: **Future Studies**. This section introduces the main open questions and opportunities that I want to contribute to answer with future studies and work.

2 Methodology

I have used the Generic-GCM described previously (**section 1.3.4.**) to investigate the impact of a set of planetary parameters in the large-scale circulation of Venus-like exoplanetary atmospheres and assess their potential influence on the synthetic observables. The followed methodology is presented below:

1. **Modelling Venus atmosphere with the Generic-GCM**. I simulate Venus orbiting the Sun at its orbital distance of 0.72 AU using a Venus-like atmosphere and the following planet's parameters: radius, rotation rate and surface gravity. The objectives are two-fold: **(i)** to assess if the Generic-GCM is reproducing the essential characteristics of the large-scale atmospheric circulation: the superrotation pressure range and wind speed predicted by the Venus GCM, the IPSL-VCGM([15]) (Garate-Lopez and Lebonnois, 2018); and **(ii)** to obtain a global temperature profile that will serve as an input for simulating a Venus-like exoplanet orbiting an M-dwarf star. The start files used as input for the Generic-GCM simulations already have the planet's atmosphere in a state of superrotation.
2. **3D Climate modelling of TRAPPIST-1 c with a Venus-like atmosphere**. Based on the state-of-the-art literature, I select TRAPPIST-1 c as a possible Venus-like exoplanet, using its planetary parameters (orbital distance, radius, surface gravity) (Agol et al., 2021), combined with realistic assumptions. The objective is to simulate a Venus-like atmosphere on an exoplanet orbiting an M-dwarf star using the best available data. I assume TRAPPIST-1 c to be a synchronous rotator with a Venus-like atmosphere: similar chemical composition and surface atmospheric pressure with a parametrised ubiquitous global cloud layer following Haus et al. (2013). However, the dense, high mean molecular atmosphere leads to large thermal inertia in its deepest layers, preventing a steady-state after a few simulations, i.e., a classical modelling problem (Sainsbury-Martinez et al., 2019). To tackle this problem, I apply a numerical scheme with proven results (Turbet et al., 2021) to accelerate the Generic-GCM convergence towards thermal equilibrium at the TOA. The goal is to obtain a quasi-convergent simulation, using it as an initial state for the simulations of the TRAPPIST-1 c atmosphere. The final simulation is run for an additional 1000 days, and the GCM outputs are used to study the thermal structure, radiative tendencies, and large-scale atmospheric circulation. In addition, I compute reflection and emission phase curves and transmission spectra from Generic-GCM outputs.
3. **3D Climate modelling of TRAPPIST-1 c under clear-sky conditions**. Using the remaining planetary parameters as in the reference simulation, I compare the impact of clouds in the Climate simulation of TRAPPIST-1 c by assuming *clear-sky conditions*, i.e., by removing the Venus-like aerosols. The objective is to evaluate the influence of the chosen aerosol parameterisation in the thermal structure, large-scale atmospheric circulation and synthetic observables (reflection and emission phase curves).
4. **Parametric study of the Venus-like exoplanetary population**. I study the impact on the Venus-like atmosphere by varying specific planetary parameters while keeping TRAPPIST-1 as the host star and the same Venus-like atmosphere (same composition, Venus-like clouds, and surface atmospheric pressure of 92 bar) as in the reference simulation. In each parametric test, model outputs are used to analyse the thermal structure, large-scale circulation and for the production of reflection and thermal phase curves. The selected parametric tests are as follows:
   (a) **Mass-radius relationships** - varying the surface gravity (mass) and radius following an internal composition bi-layer planet model without atmosphere based on the proportion of three major planetary components (iron, rock, ice) (Zeng et al., 2016);

---

[15] IPSL-VGCM: *Institute Pierre Simon Laplace - Venus Global Circulation Model.*

(b) **Higher-order spin-orbit resonances** - studying the impact of varying TRAPPIST-1 c planetary rotation rate with higher-order spin-orbit resonances 3:2 and 2:1 (16).

I now will introduce in the next two subsections the common settings to all Generic-GCM simulations in this work: Venus-like atmosphere parameters, stellar spectra selection and instellation value selection.

2.1 Venus-like atmosphere: gases, global cloud deck and aerosol properties

In this work, I assume TRAPPIST-1 c to have a similar Venus atmospheric composition: a **carbon dioxide-dominated atmosphere** with *four minor components* (see Table 2.1), all radiatively-active species. These gases' interaction with the stellar radiation might produce recognisable signatures in the observables, possibly hinting at large-scale atmospheric processes. I excluded nitrogen, a non-radiatively active gas, from the atmospheric cocktail based on this criterion. Consequently, I increase the carbon dioxide mixing ratio and adjust the atmosphere's mean molecular weight to $44.01\ g\,mol^{-1}$.

Table 2.1: Venus-like atmosphere composition used in the Generic-GCM simulations

Chemical species	**Simulations**	**Venus**
Main Components		
Carbon dioxide (CO_2)	99.96%	96%
Nitrogen (N_2)	-	3.5%
Minor Components		
Sulphur dioxide, (SO_2)	180 ppm	150 ppm
Carbonyl sulfide, (OCS)	51.0 ppm	4 ppm
Water vapour, (H_2O)	31.1 ppm	30 ppm
Carbon monoxide, (CO)	12.0 ppm	40 ppm

Abbreviation: ppm, parts per million (10^{-6}). References of the Venus data: Taylor et al. (2018).

The chemical species used in the Generic-GCM simulations have fixed atmospheric concentrations, i.e. not variable in time, and they are used for Rayleigh scattering calculations. Thus, the model does not consider chemical/photochemical reactions that could change their relative abundances. In addition, there are no condensables in the simulated atmosphere, and the water cycle subroutines are disabled.

Each gas abundance profile was used to produce the correlated-k table coefficients in the radiative transfer calculations. Carbon dioxide abundance is constant at 99.96 % throughout the atmospheric column. In contrast, the minor components' abundances vary according to pressure level, reproducing approximately the observations in the Venus atmosphere, as seen in Figure 2.1. Furthermore, the minor components' largest abundances occur at or below the global cloud deck (see the dashed black lines in Figure 2.1), which is defined in this work between pressure ranges of $1\ bar$ and $37\ mbar$.

---

[16] Higher-order spin-orbit resonance is a type of orbital configuration in which the planet's sidereal rotation period and orbital period relate through a simple fractional relationship. The lowest energy orbital state is the synchronous rotator or 1:1 spin-orbit resonance expected in short orbit planets, as the tidal stresses from the host star tend to circularise and tide-lock the planet. However, with dynamical evolution, other higher-order spin-orbit resonances might arise, such as the 3:2 and 2:1. A planet in a 3:2 spin-orbit resonance completes three sidereal rotation periods in two orbital periods. For the 2:1 case, the planet completes two sidereal rotation periods per one orbital period.

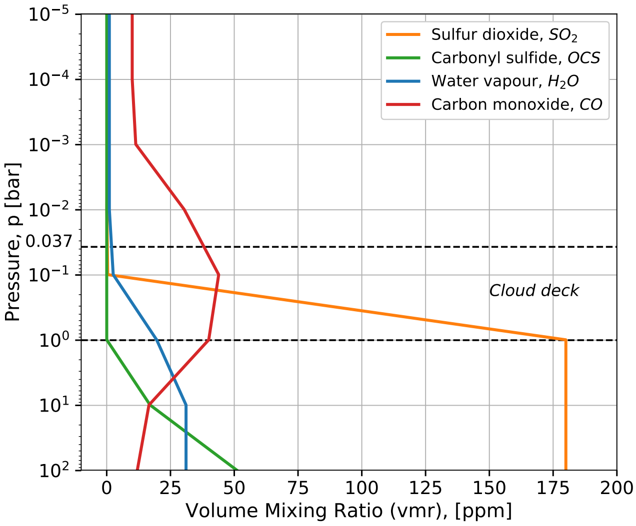

Figure 2.1: Minor species abundance profiles used for radiative transfer calculations. Three of the minor components abundances decrease to near-zero values for pressure levels above 0.1 bar. The dashed black lines represent the pressure range of the cloud deck from cloud base ($p = 1$ bar) to top ($p \sim 0.037$ bar).

Following previous modelling efforts by our collaborators at the LMD (e.g., *Sébastien Lebonnois*, *Martin Turbet*), the Generic-GCM simulations done in this work include a prescribed **globally-uniform cloud cover**, following the *ESA/Venus Express* observations reported in Haus et al. (2013). The implemented *Venus-like* global cloud cover consists of **four sulphuric acid aerosols**, defined as modes 1, 2, 2p (i.e., 2 prime), and 3, and the **"unknown" UV absorber**. The parametrisation of the sulphuric acid aerosols' effective radii and variance follows the specifications in Haus et al. (2013) (see the two top lines in Table 2.2). Moreover, no photochemistry or chemistry reactions were modelled in this Generic-GCM version, and cloud variability is not simulated in this study (implementing a microphysical cloud model for the sulphuric acid clouds in the Generic-GCM is still challenging). As such, present aerosol parameterisations included in the model are simplified schemes which use fixed values for the cloud condensation nuclei (CCN), effective radii and effective variances. Table 2.2 presents the aerosol parameters: effective radii, variances, and vertical extension of the cloud deck for each aerosol mode.

Table 2.2: Aerosol parameters used in the simulations

Aerosol	**Mode 1**	**Mode 2**	**Mode 2p**	**Mode 3**	**"unknown" UV**
Effective radius, R_{eff} (μm)	0.49	1.23	1.56	4.25	0.5
Effective variance, ν_{eff} (μm^2)	0.21	0.067	0.044	0.062	0.1
Top pressure, p_t (bar)	0.1	0.1	0.23	0.4	0.037
Base pressure, p_b (bar)	1	0.11	1	1	0.33

The calculation of aerosol mode density at each level is done by a simple pressure-dependent parametrisation included in the Generic-GCM. Each aerosol mode density distribution is defined inside a prescribed pressure range, between the base and top pressures (see the bottom two lines in Table 2.2). The numerical scheme supports transition regions where the aerosol mode density decreases towards zero for pressure layers above and beneath the base and top layers. Total aerosol opacity at each level results from combining the individual contributions from each aerosol mode density for that pressure level.

2.2 Selecting the stellar spectra and the irradiation at the TOA

When simulating a Climate in the Generic-GCM, two user-defined inputs are: **(i)** selecting the **stellar spectra** (stellar type); and **(ii)** setting the **stellar / solar flux at the TOA**, i.e, instellation or insolation.

In this work, I have used the synthetic **stellar spectra** of the Sun (a G-dwarf star) and TRAPPIST-1 (an M-dwarf star). The solar emission spectrum was provided with the downloaded Generic-GCM model package, while TRAPPIST-1's was gently given by our collaborator *Martin Turbet* (CNRS([17]), researcher at LMD, Paris, France). This stellar spectrum is the same used for the calculations in the TRAPPIST Habitable Atmosphere Intercomparison (THAI) workshop (Fauchez et al., 2021), and its wavelength range goes from the UV at $\sim 0.202\ \mu m$ to the mid-infrared (MIR) at $\sim 25.196\ \mu m$. This wavelength range covers most of TRAPPIST-1 stellar emission. Moreover, it contains the stellar emission in the deep regions of the MIR, where robust molecular absorption features may be identified in the TRAPPIST-1 c planetary atmosphere. As expected, dimmer TRAPPIST-1's emission peak occurs in the near-infrared (NIR), as seen in Figure 2.2.

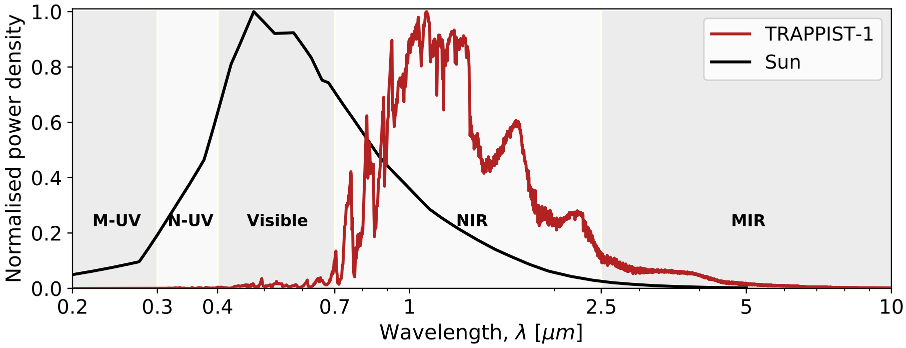

Figure 2.2: The synthetic emission spectra of the M-dwarf star TRAPPIST-1 (solid red line) and the Sun (solid black line) normalised by each spectrum's peak intensity value. The represented wavelength range spans from the middle-ultraviolet at 0.2 μm to the MIR at 10 μm. These synthetic emission spectra are used as inputs for the Generic-GCM calculations. The regions of the electromagnetic spectrum encompassed by this wavelength range are represented in shades, with the respective abbreviations: middle ultraviolet (M-UV): (i) 0.2 - 0.3 μm; (ii) near-ultraviolet (N-UV): 0.3 - 0.4 μm; (iii) visible: 0.4 - 0.7 μm; (iv) near-infrared (NIR): 0.7 - 2.5 μm; and (v) mid-infrared (MIR): 2.5 - 10 μm.

The Generic-GCM calculates the **stellar irradiation at the TOA** using the user-defined stellar flux value at 1 AU distance from the star, $F_{*,AU}$. For the Solar System, this value corresponds to the Earth's insolation, 1366 $W\,m^{-2}$, while for TRAPPIST-1, it is 0.7527 $W\,m^{-2}$ (see equation 2.4). The user also defines the planet's orbital distance, r (in AU), that the model uses to calculate the stellar irradiation on the TOA, F_r, according to the following equation:

$$F_r = F_{*,AU}\,\frac{d^2}{r^2} = F_{*,AU}\,\frac{1}{r^2} \tag{2.1}$$

Where the distance d represents 1 AU. The stellar irradiation value obtained in the model is the incoming stellar irradiation, which is corrected in the model for the planetary bond albedo to yield the absorbed stellar irradiation, the energy input quantity for the Climate.

The last two subsections introduced the settings used in all Generic-GCM simulations in this work. I will now introduce the parameters and assumptions needed for modelling Venus with the Generic-GCM.

---

[17] *Centre national de la recherche scientifique.*

2.3 Modelling Venus atmosphere with the Generic-GCM

The orbital and solid-body parameters (see Table 2.3) and the solar spectrum are used as inputs to simulate Venus's atmosphere with Generic-GCM. This simulation aims to evaluate whether the Generic-GCM can reproduce the general characteristics of the large-scale atmospheric circulation of Venus: the superrotation jets located at mesospheric levels and their wind speeds. The simulation is set to run a total of 300 Earth-days([18]). Since Venus is not a synchronous rotator, I declared in the model the length of the Venus year in solar days units: 1.92, given by the ratio between the planet's orbital period (T_P = 224.701 Earth days) and its solar day (P_s = 116.750 Earth days) (Williams, 2022a). I have assumed a circular orbit for simplicity. The maximum solar irradiance at the subsolar point is 2609.46 $W\,m^{-2}$ which is in good agreement with the value estimated for Venus (2601.3 $W\,m^{-2}$). Furthermore, the obliquity and the solid-body rotation are set for Venus values. The latter is obtained from the ratio between 2π and sidereal rotation period (P = 243.690 Earth days) (Williams, 2022a) - making the modelled planet Venus a realistic *slow rotator*.

Table 2.3: Planetary parameters for Venus used in the Generic-GCM simulation

Planetary Parameter	**Venus**
Orbital Parameters	
Semimajor axis, a (AU)	0.72
Eccentricity, e	0
Obliquity to orbit (deg)	177.36
Insolation, S ($W\,m^{-2}$)	2609.46
Solid-body Parameters	
Radius, R ($10^6\,m$)	6.052
Surface gravity, g ($m\,s^{-2}$)	8.87
Solid-body rotation rate, Ω ($rad\,s^{-1}$)	$2.99 \cdot 10^{-7}$

In addition, I decided to explore how the superrotation responds to varying the insolation at the TOA, which is done by changing the orbital distance (see Table (2.4)). The planet was placed at three additional orbital distances, all farther away from the Sun. In these simulations, I assumed the ratio between the orbital period and the sidereal rotation period to be constant and equal to 0.922. From Kepler's Third Law, I calculated the new orbital periods, T_P, for the selected orbital distances, by solving equation (2.2):

$$a^3 = k\,T_P^2 \tag{2.2}$$

Where k is a proportionality constant for the Solar System, equivalent to $7.496 \cdot 10^{-6}$ AU^3 / Earth days^2 (De Pater and Lissauer, 2015). After obtaining the new orbital period for the planet, the sidereal rotation period is calculated solving equation (2.3):

$$\frac{\texttt{Orbital Period}}{\texttt{Sidereal Rotation Period}} = 0.922 \tag{2.3}$$

The new values for the orbital distance and period, sidereal rotation period, rotation rate and the insolation are present in the Table (2.4). In all simulations, the ratio between the orbital period and the

---

[18] An Earth day is equivalent to 86 400 s.

solar day is 1.92.

Table 2.4: Calculated parameters for a Venus-like planet at different orbital distances from the Sun

Orbital distance $a\,(AU)$	**Orbital period** T_P (Earth days)	**Sidereal rotation period** P (Earth days)	**Rotation rate** $\Omega\,(rad\,s^{-1})$	**Insolation** $S\,(W\,m^{-2})$	 $S\,(S_{\oplus})$
0.72	224.70	243.69	$2.98 \cdot 10^{-7}$	2609.46	1.91
0.90	311.85	338.23	$2.15 \cdot 10^{-7}$	1685.49	1.23
1.00	365.25	396.15	$1.84 \cdot 10^{-7}$	1365.25	1.00
1.20	480.13	520.75	$1.40 \cdot 10^{-7}$	948.09	0.69

Following the Generic-GCM simulations of Venus orbiting the Sun and the subsequent tests to assess the response of the large-scale atmospheric circulation to the decreasing insolation, I proceed to the simulations of a Venus-like exoplanet orbiting a colder, dimmer star than the Sun: TRAPPIST-1.

2.4 3D Climate modelling of TRAPPIST-1 c with a Venus-like atmosphere

This section will introduce the planetary parameters used to set the simulation of TRAPPIST-1 c, the benchmark planet for the onset of studies on the population of Venus-like exoplanets. Then, to tackle the problem of modelling a dense atmosphere with a high mean molecular weight, I will present the numerical scheme used to address the problem and obtain a quasi-convergence of the radiative balance at TOA.

The TRAPPIST-1 c planetary parameters introduced in the model can be seen in Table 2.5. With the exception of obliquity, eccentricity and solid-body rotation period and rotation rate, the remaining parameters have state-of-the-art values (Agol et al., 2021; Grimm et al., 2018).

Table 2.5: Planetary Parameters of TRAPPIST-1 c used in the reference simulation

Planetary Parameter	**TRAPPIST-1 c**
Orbital Parameters	
Orbital Period, $T_P\,(Earth\ days)$	2.42
Semimajor axis, $a\,(AU)$	0.0158
Eccentricity, e	0
Obliquity (deg)	0
Instellation, $S\,(W\,m^{-2})$	3015
Solid-body Parameters	
Radius, $R\,(10^6\,m)$	6.995
Surface gravity, $g\,(m\,s^{-2})$	10.65
Solid-body rotation period, $P\,(s)$	209 000
Solid-body rotation rate, $\Omega\,(rad\,s^{-1})$	$3 \cdot 10^{-5}$

In the simulations, I have assumed that the orbital eccentricity and obliquity of TRAPPIST-1 c are both *zero* (i.e., the planet has no seasons). These are good assumptions for close-in planets orbiting M-dwarf stars, as these planets are likely to be subject to orbital circularisation due to tidal forces from the host star. This assumption is supported by the low eccentricity values (e = $6.54 \cdot 10^{-3}$) for TRAPPIST-1 c found by Grimm et al. (2018). Likewise, the obliquity or axial tilt is assumed to be zero, also a good assumption given the magnitude of gravitational tides expected for such a planet (Ribas et al., 2016). Planetary impacts can change the axial tilt, but information regarding this parameter is beyond our current technological capabilities. The most likely scenario for the TRAPPIST-1 c rotation rate is a synchronous rotator, supported by TRAPPIST-1 system orbital architecture. In the reference simulation, as a tide-locked planet, its orbital period equals the sidereal rotation period. Thus, I assumed a 209 000 s for the sidereal day period and a rotation rate of $3 \cdot 10^{-5}\ rad\, s^{-1}$. Therefore, the sidereal day on TRAPPIST-1 c is 2.42 times longer than Earth's, and its rotation rate is approximately 41% that of the Earth.

To calculate TRAPPIST-1 c's instellation, I first calculate the stellar flux at 1 AU with (2.4), using SI units:

$$F_{*,AU} = \frac{L_*}{4\pi\, r^2} \tag{2.4}$$

Where L_* is the stellar luminosity ($L_* = 5.53 \cdot 10^{-4}\ L_\odot$ ([19]) in Ducrot et al. (2020)). From equation (2.4), $F_{*,AU}$ yields 0.7527 $W\, m^{-2}$. From equation (2.1), TRAPPIST-1 c instellation is $S \sim 3015\ W\, m^{-2}$ (2.21 $S_\oplus$) at the substellar point, within the error margin estimated by Agol et al. (2021): $3013^{+117}_{-115}\ W\, m^{-2}$.

Horizontal, vertical and time resolutions. The reference simulation was performed with a horizontal resolution of 64 × 48 in longitude and latitude, corresponding to 5.625° longitude by 3.75° latitude. For TRAPPIST-1 c, it corresponds approximately 688 km per 458 km at the equator. In the vertical direction, the model is composed of a total of 50 distinct atmospheric layers under the assumption of hybrid $\sigma - p$ coordinates, extending from the surface to $\sim 0.05\ mbar$.

The dynamical time step is updated every 1.45 minutes, and the tendencies given by the physical parameterisations (physical time step) are calculated every 29 minutes. These values have been calculated to avoid model instabilities and adequate to the selected horizontal resolution. The radiative transfer tendencies are updated every 24 physical time steps. However, to better time represent the observables, I decreased the radiative time step to 1, i.e., the radiative time step is calculated at each physical time step.

Planetary surface and soil parameters I assume a rocky ground with 18 soil layers, with a thermal inertia of 2000 $J\, m^{-2}\, K^{-1}\, s^{-\frac{1}{2}}$, following the value in Leconte et al. (2013b) for continental ground. For the planetary surface, I select a **flat topography** and a **surface albedo** of **0.2**. The surface temperature is set as an input and assumed to be equal to the temperature of the lowest atmospheric level.

2.4.1 A numerical scheme for the convergence acceleration of hot, dense atmospheres

Unlike the uppermost layers of the atmosphere, which advance very fast towards equilibrium, the evolution in the deepest layers is slow. Thus simulating a hot dense Venus-like atmosphere creates *modelling challenges* that must be tackled with an appropriate **numerical scheme** to accelerate convergence in the deepest layers. The very large opacity, mean molecular weight, and heat capacity of the modelled high surface pressure (92 bar) carbon dioxide-dominated atmosphere will significantly increase the computation time needed for the simulation to reach the TOA radiative balance. Rather than being

---

[19] $L_\odot$, one solar luminosity, equals $3.828 \cdot 10^{26}\ W$ (International Astronomical Union, IAU) (Mamajek et al., 2015).

a problem of this work's simulation, very long convergence times are a **classical modelling problem** (Charnay et al., 2021; Sainsbury-Martinez et al., 2019; Turbet et al., 2021; Wang and Wordsworth, 2020).

To address the long computational time needed to obtain the radiative equilibrium at the TOA, we implemented a numerical scheme to accelerate the convergence in the deepest layers of the atmosphere, following Charnay et al. (2021); Turbet et al. (2021). The long and short wavelength heating rates in the radiative transfer routine are artificially multiplied by a *factor* under a pressure-dependent threshold:

$$\texttt{factor} = \left(\frac{p}{p_{lim}}\right)^{\alpha} \quad p > p_{lim}\ ,\ \texttt{with}\ p_{lim} = 10^4\ \texttt{Pa} \tag{2.5}$$

Where α is a convergence factor and p_{lim} is the pressure threshold ($10^4\ Pa$) for which the radiative tendencies in deeper layers are artificially accelerated. I have tested different convergence factor values, and the sensitivity tests showed that radiative tendencies evolution is faster under larger values of the convergence factor. Nonetheless, for values larger than α = 0.6 the simulations crashed. Therefore, I established the value of α = 0.6 as the convergence factor in the simulations.

To obtain the radiative balance at the TOA for the TRAPPIST-1 c simulation, I used as an input the global-mean temperature profile from the Generic-GCM simulation of Venus, described in **section 2.3**. I decided to define a **limit criterium** based on the radiative imbalance at TOA: the difference between the planet integrated absorbed stellar radiation (ASR) and outgoing long-wavelength radiation (OLR) should not be larger than 10 $W\,m^{-2}$ for at least 1000 orbits. In the aftermath, the model ran for 15 000 orbits of TRAPPIST-1 c with α = 0.6, resulting in a quasi-equilibrium state at the TOA ($\sim$ 6 $W\,m^{-2}$).

To double-check the quasi-equilibrium state obtained by accelerating the radiative tendencies after 15 000 orbits, I performed an additional Generic-GCM simulation using a *warmer* initial temperature profile as an input (50 K warmer than the previous profile). The two simulations, initialised with different temperature profiles: the hot adiabatic profile and cold adiabatic profile (Figure 2.3), almost converge to a similar temperature profile after 15 000 orbits.

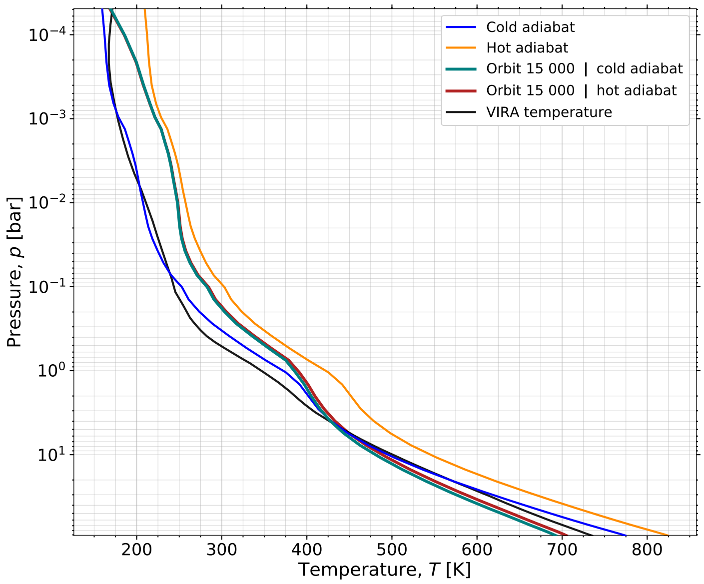

Figure 2.3: Temperature profiles used in the study of the numerical convergence scheme. The two input temperature profiles, the cold adiabat (solid blue line) and hot adiabat (solid yellow line), differ from each other by 50 K. The cold adiabatic profile results from Generic-GCM simulation of Venus. Surface temperatures are 775 K and 825 K for the cold and hot adiabat profiles, respectively. The final temperature profiles obtained after 15 000 orbits of TRAPPIST-1 c are presented for both cases, cold (solid green line) and hot (solid brown line). The Venus International Reference Atmosphere (VIRA) temperature profile is presented as black solid line, for comparison.

The hot adiabatic profile has *worse* values of radiative imbalance at the TOA than the cold one, reaching $\sim 9.9\ W\,m^{-2}$ after 15 000 orbits. For this reason the cold adiabat temperature profile obtained from the quasi-equilibrium state of TRAPPIST-1 c is selected as a *initial state* for the *nominal* reference simulation of TRAPPIST-1 c and additional parametric tests, which run for an additional 1000 orbits with $\alpha = 0$. The TOA radiative imbalance for these simulations is lower than about $5\ W\,m^{-2}$.

Finally, to double-check that the numerical scheme for convergence acceleration is working correctly, I performed an additional test with an isothermal atmospheric profile of 600 K as an initial state. The simulation converged, although *slower*, to the same radiative equilibrium at the TOA as the previous ones. The longer convergence time required for isothermal atmospheric profiles has already been reported in (Turbet et al., 2021). Additional simulations with isothermal atmospheric profiles of 700 K and 800 K were also tested but ended up with the model crashing.

2.5 3D Climate modelling of TRAPPIST-1 c under clear-sky conditions

To obtain the clear-sky simulation of TRAPPIST-1 c, I compiled the Generic-GCM without Venus-like aerosols. As an initial state, I used the cold adiabat temperature profile obtained from the quasi-equilibrium state of TRAPPIST-1 c. The final simulation has a radiative imbalance at TOA lower than $5\ W\,m^{-2}$, after 25 000 orbits of TRAPPIST-1 c. I applied the numerical scheme as in **section 2.4.1**, with $\alpha = 0.6$ in the first 20 000 orbits, removing the convergence factor in the final 5 000 orbits.

2.6 Parametric study of the Venus-like exoplanetary population

With this parametric study, I am not only simulating TRAPPIST-1 c with a Venus-like atmosphere but working towards extending conclusions to a broad population of Venus-like exoplanets, starting with mass-radius relationships and higher-order spin-orbit resonances. The former seeks to understand the impact of changing surface gravity and radius in the large-scale circulation and synthetic observables. The latter focuses on understanding the impact of varying TRAPPIST-1 c planetary rotation rate. All parametric studies assumed a Venus-like atmosphere with Venus-like clouds.

2.6.1 Mass-radius relationships

The mass-radius relationship values for rocky planets used in this work are taken from Zeng et al. (2016). The interior compositions follow a bi-layer planet model without atmosphere varying from 100% Fe to pure rock ($MgSiO_3$) to 100% H_2O, with intermediate compositions of Iron-Rock or Rock-Water (e.g., 20% Fe corresponds to 20% Fe and 80% $MgSiO_3$). The Generic-GCM has as inputs radius and surface gravity. Thus, to estimate the surface gravity, g, I used the following equation:

$$g = G\frac{M}{R^2} \tag{2.6}$$

Where M and R are respectively the planetary mass (in kg) and radius (in m), while G is the gravitational constant in SI units ($G = 6.67430 \cdot 10^{-11}\ m^3\,kg^{-1}\,s^{-2}$). In the calculations, I used $1\ M_\oplus = 5.9742 \cdot 10^{24}\ kg$ and $1\ R_\oplus = 6.371 \cdot 10^{6}\ m$, following Zeng et al. (2016). To prepare a wide study of mass-radius relationships, I took four different planetary masses: 0.5, 1, 2, and 4 $M_\oplus$, whose respective radii are in Zeng et al. (2016) and presented in Table 2.6 in Earth radii units ($R_\oplus$), following the several cases of the bi-layer internal composition model. Mass and radius are converted to SI units (blue rows in Table 2.6), and used for the calculation of surface gravity following equation 2.6. The calculated surface gravity values are presented in Table 2.7.

Table 2.6: Mass-radius relationship following Zeng et al. (2016) with unit conversion (blue rows)

	100%Fe	50%Fe	30%Fe	25%Fe	20%Fe	Rock	25%H_2O	50%H_2O	100%H_2O
Mass	Radius								
$M_\oplus$	$R_\oplus$	$R_\oplus$	$R_\oplus$	$R_\oplus$	$R_\oplus$	$R_\oplus$	$R_\oplus$	$R_\oplus$	$R_\oplus$
$10^{24}\ kg$	$10^6\ m$	$10^6\ m$	$10^6\ m$	$10^6\ m$	$10^6\ m$	$10^6\ m$	$10^6\ m$	$10^6\ m$	$10^6\ m$
0.5	0.676	0.789	0.823	0.832	0.840	0.872	0.969	1.039	1.163
2.987	**4.307**	**5.027**	**5.243**	**5.301**	**5.352**	**5.556**	**6.173**	**6.619**	**7.409**
1	0.823	0.961	1.005	1.016	1.026	1.067	1.182	1.270	1.410
5.974	**5.243**	**6.123**	**6.403**	**6.473**	**6.537**	**6.798**	**7.531**	**8.091**	**8.983**
2	0.990	1.164	1.220	1.230	1.250	1.300	1.440	1.540	1.710
11.95	**6.307**	**7.416**	**7.773**	**7.836**	**7.964**	**8.282**	**9.174**	**9.811**	**10.89**
4	1.176	1.400	1.470	1.490	1.500	1.570	1.740	1.850	2.050
23.90	**7.492**	**8.919**	**9.365**	**9.493**	**9.557**	**10.00**	**11.09**	**11.79**	**13.06**

Table 2.7: Surface gravity values calculated with equation (2.6) and following the Mass-radius relationships in Table 2.6

	100%Fe	50%Fe	30%Fe	25%Fe	20%Fe	Rock	25%H_2O	50%H_2O	100%H_2O
M, $M_\oplus$	Surface gravity g, $m\,s^{-2}$								
0.5	**10.748**	**7.890**	**7.252**	**7.096**	**6.961**	**6.460**	**5.231**	**4.550**	**3.631**
1	**14.503**	**10.637**	**9.726**	**9.517**	**9.332**	**8.629**	**7.031**	**6.091**	**4.941**
2	**20.046**	**14.501**	**13.200**	**12.986**	**12.574**	**11.626**	**9.475**	**8.284**	**6.719**
4	**28.413**	**20.048**	**18.184**	**17.699**	**17.464**	**15.942**	**12.979**	**11.481**	**9.350**

In this study, I am interested in exploring the impact of varying mass and radius on a specific internal composition. From the literature review of the interior composition of TRAPPIST-1 planets, I chose the bi-layer composition 20% Fe (Agol et al., 2021; Turbet et al., 2020a). I used the respective radius in m in Table 2.6 and the surface gravity in $m\,s^{-2}$ in Table 2.7 as input parameters in the simulations.

2.6.2 Higher-order spin-orbit resonances

The reference simulation assumes that TRAPPIST-1 c is a synchronous rotator, which is a reasonable assumption considering the TRAPPIST-1 planetary system's orbital architecture. Nevertheless, I decided to study higher-order spin-orbit resonances, 3:2 and 2:1 cases, assuming a circular orbit. Therefore, I have updated the sidereal rotation period and rotation rate for these simulations, keeping the remaining planetary parameters of TRAPPIST-1 c (as in Table 2.1). The new sidereal rotation period, P, was calculated for each case by using its relationship with the orbital period (T_P = 209 000 s):

$$P = \frac{\texttt{orbits}}{\texttt{spins}}\, T_P \tag{2.7}$$

The proportionality factor is the ratio between the number of orbits to the number of rotations. The values (input parameters) calculated for the sidereal rotation period and rotation rate, obtained from dividing 2π by P, are presented in the Table 2.8, together with the values used in the reference simulation.

Table 2.8: Calculated planetary parameters for the spin-orbit resonances

Spin-orbit resonance	**Sidereal rotation period** P, s (Earth days)	**Rotation rate** Ω, $rad\, s^{-1}$
1:1 (reference)	209 000 (2.42)	$3.00 \cdot 10^{-5}$
3:2	139 200 (1.61)	$4.50 \cdot 10^{-5}$
2:1	104 600 (1.21)	$6.00 \cdot 10^{-5}$

2.7 Synthetic Observables

One objective of this work is the production of two kinds of synthetic observables from the model's outputs: phase curves and transmission spectra. The former is computed for reflection and emission planetary fluxes. The transmission spectra are computed for TRAPPIST-1 c for two cases: (i) radiatively active Venus-like aerosols with a global cloud deck; and (ii) without clouds, i.e., clear-sky conditions.

2.7.1 Phase Curves

The Generic-GCM uses radiative transfer calculations to produce outgoing radiative fluxes at the TOA. These fluxes are produced for each spectral band and cell. Two types of fluxes are computed: reflected stellar radiation and planetary infrared emission. The TOA GCM fluxes are produced in pre-selected, specific spectral bands, with the model using 36 spectral bands (between 0.25 μm and $\sim$ 5.13 μm) for the reflected stellar radiation and 32 spectral bands (between 3.51 μm and $\sim$ 25.20 μm) for planetary infrared emission. Each flux type is then saved into a separate Generic-GCM output file at the end of each simulation.

The reflection (or emission) phase curves, i.e., planet-to-star contrast, are calculated as the ratio between the planet's reflected (emitted) flux and the stellar flux. Their calculation from GCM outputs requires the disk integration of the reflected (emitted) fluxes from the planet's hemisphere facing the Earth. To compute the phase curves (reflection or emission), I developed a *Python* script, available in the **Appendix II**. In order to calculate the planetary disk-integrated outgoing flux for a given orbital phase of the planet, the PCAR routine uses a formula similar to equation (7) in Von Paris et al. (2016). This formula yields the outgoing flux from a cell and received by the observer, $F_{r,o,cell}$:

$$F_{r,o,cell} = cos\; z_s \cdot F_{*,P} \cdot \frac{A_s}{\pi} \cdot cos\; z_o \cdot \frac{\Delta S}{d_o^2} \tag{2.8}$$

Where z_s is the local stellar zenith angle, $F_{*,P}$ is the stellar flux at the planet's orbital distance, A_s is the planetary scattering albedo, z_o is the local observer zenith angle, ΔS is the surface element area of the cell, and d_o is planet-observer distance. In the PCAR routine, the planetary disk-integrated intensity is calculated for each orbital phase and bandwidth. The outgoing TOA fluxes by the Generic-GCM consider already the local stellar zenith angle, the stellar flux at the planet's distance and the planetary scattering albedo. Thus, for each grid cell, the PCAR code only needs to multiply the model's outgoing TOA fluxes by the cell's surface area ΔS (a model output), and the cosine of the local observer zenith angle, $cos\; z_0$.

Furthermore, I imposed a *geometric condition* that considers only the fluxes incoming from cells located in the planet's Earth-facing hemisphere at each orbital phase for the calculation of the disk-integrated planetary flux. To calculate the planet-to-star contrast, and hence the phase curves, the code needs to consider the stellar intensity. According to Von Paris et al. (2016), the stellar flux at observer, $F_{*,o}$, is calculated according to:

$$F_{*,o} = \pi \left(\frac{R_*}{d_o} \right)^2 \int_{\lambda_{\mathtt{low}}}^{\lambda_{\mathtt{high}}} I_{*,s} q_I(\lambda) \, \mathrm{d}\lambda \tag{2.9}$$

Where R_* is the stellar radius, $I_{*,s}$ is the stellar intensity in $W\, m^{-2}\, sr^{-1}\, \mu m^{-1}$ at the stellar surface, q_I is a filter function, and $\lambda_{\mathtt{low}}$ and $\lambda_{\mathtt{high}}$ are the wavelength limits of the spectral band. The PCAR routine solves the integral in equation (2.9). Additionally, the planetary flux disk-integration considers the sub-observer latitude in the planet, allowing for exploration of different observational geometries (i.e., inclination) of the planetary system. Figure 2.4 displays two of these observing geometries. For the 90° inclination, the planet's orbit is edge-on for an Earth observer, and the planet transits (at orbital phase $-\pi$ or π) and undergoes a secondary eclipse (at orbital phase 0).

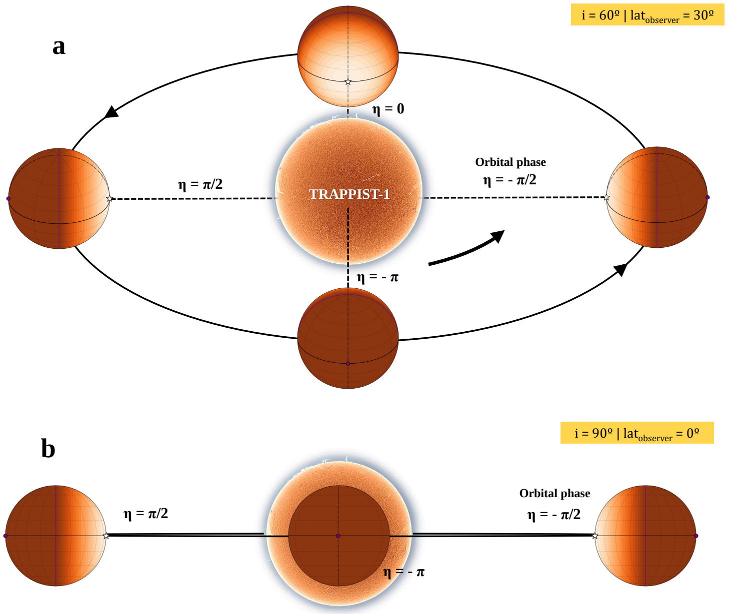

Figure 2.4: Orbital phases nomenclature used for phase curve computation for two observing geometries (inclination i and sub-observer latitude, $lat_{observer}$ in Figure): **(a)** inclination 60° (sub-observer latitude 30°); and **(b)** inclination 90° (sub-observer latitude 0°). The solid black arrow in panel **(a)** indicates the orbital phase η progression, from $-\pi$ to $-\pi/2$, followed by subsequent phases. Planetary transits and secondary eclipses only occur in the configuration depicted in panel **(b)**, respectively at orbital phases $-\pi$ and 0. The 90° inclination panel is closer to the inclination values of TRAPPIST-1 planets. A white star (purple dot) represents the substellar (antistellar) point in both panels. Note that the planet and star dimensions and the orbital distances are not to scale.

Calculating the phase curves in higher-order spin-orbit resonances The radiative transfer can be computed at a given physical time step interval. For the 2:1 and 3:2 spin-orbit resonances, I updated the radiative time step to match specific orbital phases allowing me to define the location of the sub-observer point (see the example in Figure 2.5). I then checked the position of the incoming stellar radiation maximum at each given instant to confirm the validity of the assumption. In the following example, in Figure 2.5, the star-planet-observer geometry is described for a planet in a 2:1 spin-orbit resonance. The example depicts a quarter of the orbit of this planet, which corresponds to half spin. In the example the number of radiative time steps per orbit set in Generic-GCM is 8, which allow the user to select the sub-observer longitude at each radiative time step, necessary for the PCAR routine to identify the Earth-facing hemisphere of the planet.

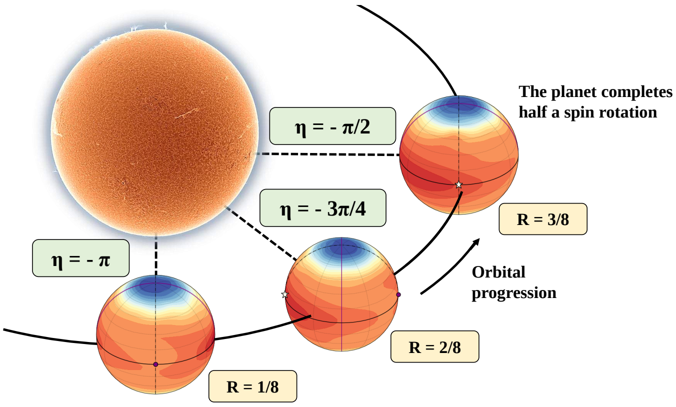

Figure 2.5: Star-planet-observer geometry of a planet under a 2:1 spin-orbit resonance. The orbital phases are represented by green boxes. The number of radiative time steps per orbit is 8 (yellow boxes). The white star marks the sub-stellar point at the beginning of the orbit (and simulation).

2.7.2 Transmission Spectra

To simulate the transmission spectra of TRAPPIST-1 c, I used the `Planetary Spectrum Generator` (PSG, https://psg.gsfc.nasa.gov) (Villanueva et al., 2018). The PSG is a radiative transfer code available online that computes planetary spectra for atmospheres and surfaces from Solar System objects and exoplanets. The online code covers a wide range of the electromagnetic spectrum, from UV to radio, and it can provide synthetic observables for several observatories and instruments. The PSG also provides a noise calculator (PSG imager noise model). Noise analysis in its components (source, background, detector, and telescope) will be address in future studies.

I set PSG to simulate JWST transmission spectra of the reference simulation of TRAPPIST-1 c with a Venus-like atmosphere under two cases: **(i)** Venus-like clouds; and **(ii)** clear-sky conditions. The GCM outputs: temperature, gas abundances and aerosols (modes 1 and 2) profiles, were used in the PSG to calculate the transmittance of radiation passing through the terminator of TRAPPIST-1 c with the help of *Thomas Fauchez*. In addition, the clear-sky conditions were simulated by removing the radiative contribution from the Venus-like aerosols in the PSG settings to understand the impact of the global cloud cover on the observed transmission spectra. In both simulations, with Venus-like clouds and clear-sky conditions, four *continuum* processes were considered: (i) Rayleigh molecular scattering; (ii) refraction; (iii) collision-induced absorption and emission; and (iv) ultraviolet broad absorption, for wavelengths smaller than 1.0 μm. Furthermore, transmission spectra were corrected for truncation of spectral features. Truncation emerges as a significant part of the CO_2 absorption occurs in the upper atmosphere above the cloud top (e.g., in the region sounded by transmission spectroscopy), which was not covered by the initial uploaded temperature profile. In order to include the uppermost layers, I used a PSG feature to extend atmospheric profiles from 0.05 $mbar$ to 1 $pbar$ artificially.

The JWST segmented mirror has an aperture size of 6.5 m, corresponding to a 5.64 m diameter disk, a value that I use on PSG. I computed the transmission spectra for a resolving power of 1000 from 0.6 μm to 20 μm relevant for the JWST `NIRSpec Prism` (Near-Infrared Spectrograph) and `MIRI` (Mid-Infrared Instrument) instruments. `NIRSpec PRISM` has proven to be the ideal JWST instrument for terrestrial exoplanet transmission spectroscopy characterisation, in particular in the TRAPPIST-1 planetary system, due to its combination of resolving power and relatively broad wavelength coverage (Batalha et al., 2018; Fauchez et al., 2019; Lincowski et al., 2019; Lustig-Yaeger et al., 2019a), with the TRAPPIST-1 star flux being likely under saturation levels for the detector. The `MIRI` will be used for secondary eclipse photometry studies of thermal emission detection from TRAPPIST-1 c (Lustig-Yaeger et al., 2019a).

3 Results

3.1 Modelling Venus atmosphere with the Generic-GCM

Before studying a Venus-like exoplanetary atmosphere, I decided to compare Venus simulated with the Generic-GCM and the last version of the IPSL-VGCM (Garate-Lopez and Lebonnois, 2018). This exercise follows a previous comparison study done by LMD colleagues between these models in different Venus atmospheric configurations. First, I compare the large-scale atmosphere circulation between the two models, focusing on the zonal superrotation structure and wind speeds (see Figure 3.1). The simulation run for 300 Earth days, using an initial state already in superrotation (see **section 2.3**). Finally, I analyse the Generic-GCM response to varying insolation by increasing the planet's orbital distance.

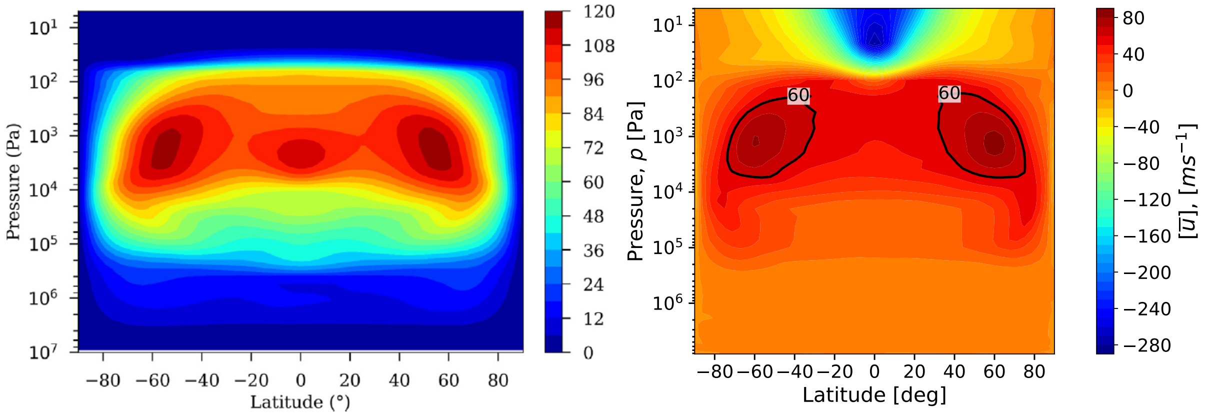

Figure 3.1: Zonal and time-averaged zonal wind field in $m\,s^{-1}$ of Venus simulated by the IPSL-VGCM (Garate-Lopez and Lebonnois (2018), in their Figure 4) (left panel) and by the Generic-GCM (this work) (right panel). In the right panel, the 60 $m\,s^{-1}$ isotach (solid black line) identifies the core of the zonal superrotation jets.

Overall, the Generic-GCM reproduces the superrotation regime's main aspects (pressure range, wind speeds) seen in the IPSL-VGCM. From Figure 3.1, there is a good agreement between the two models for the pressure range of the zonal superrotation, which extends between $\sim 10^4\ Pa$ (100 $mbar$) and $\sim 10^2\ Pa$ (1 $mbar$). The Generic-GCM reproduces the high-latitudes jets (see the 60 $m\,s^{-1}$ isotach in the right panel) at similar latitudes (centred at ∼ 60° N/S) and pressure level ($\sim 2 \cdot 10^3\ Pa$ or $\sim 20\ mbar$). The jets' wind speed in the Generic-GCM is $\sim 90\ m\,s^{-1}$, lower than the 120 $m\,s^{-1}$ value obtained in the IPSL-VGCM by Garate-Lopez and Lebonnois (2018). In opposition, the Generic-GCM simulation does not reproduce the equatorial jet documented in Garate-Lopez and Lebonnois (2018). Besides, in the Generic-GCM, there is an equatorial retrograde zonal jet in the uppermost layers of the atmosphere ($p \lesssim 10^2\ Pa$ or 1 $mbar$), not seen in the simulation by the IPSL-VGCM.

The model-model comparison in Figure 3.1 reveals that the Generic-GCM can reproduce the most significant large-scale atmospheric circulation features of a slow-rotator planet with a large mean molecular atmospheric weight like that of Venus. To assess how the Generic-GCM responds to varying a specific parameter with impact in Climate, I decided to decrease the insolation value by increasing orbital distance while adjusting the planetary rotation rate. Insolation is a critical parameter to understand how the modelled Climate system responds. To assess the model's response, I compare the zonal and time-averaged zonal wind field for four orbital distances of the simulated planet Venus in Figure 3.2.

The simulations show an overall *decrease* in zonal wind speed with *decreasing* insolation. The zonal wind speed slowdown occurs as the energy input in the Climate system reduces for larger orbital distances. Consequently, there is less need for day-night energy advection, leading to a decrease in wind momentum.

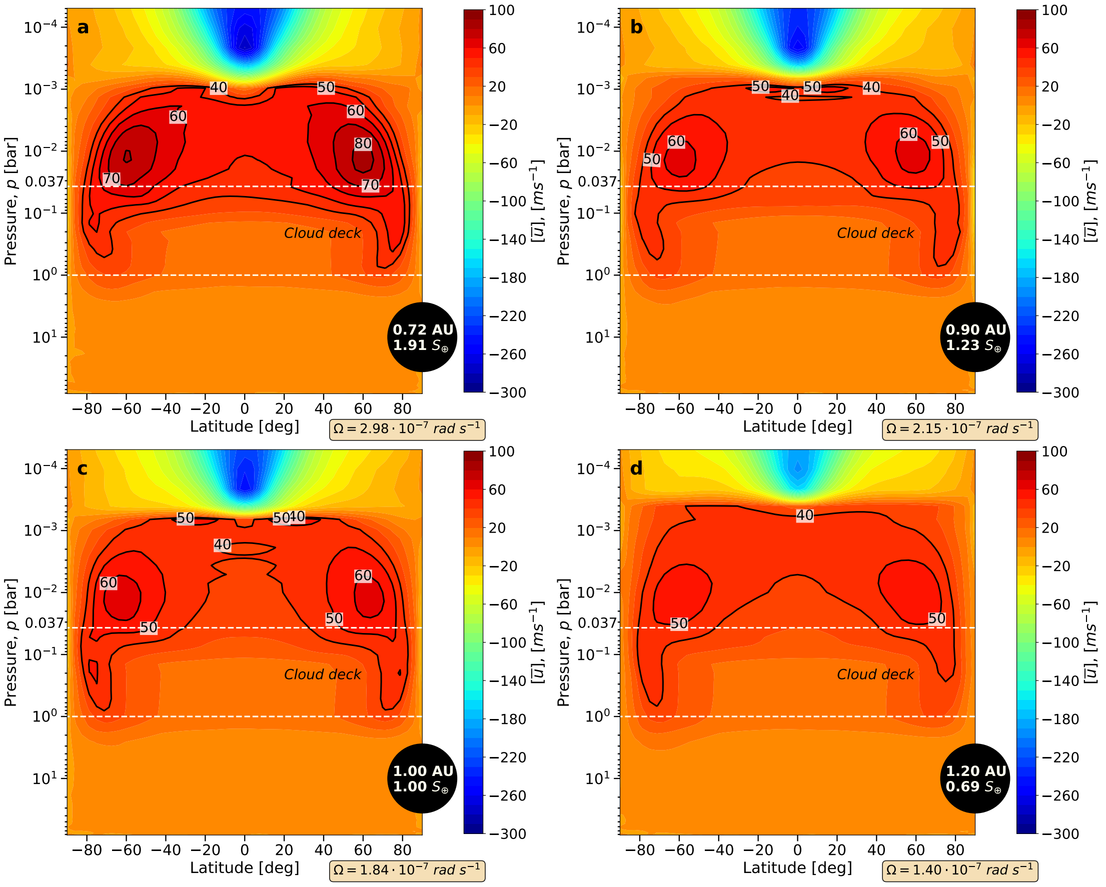

Figure 3.2: The zonal and time-averaged zonal wind field for four insolation values, resulting from varying the orbital distance of Venus orbiting the Sun simulated with the Generic-GCM. Data is time-averaged for the final simulation after 300 Earth days. Insolation values decrease from **(a)** to **(d)** following the increment in orbital distance, as shown in the inset black circle. The planetary rotation rate Ω in $rad\, s^{-1}$ is depicted below each figure. Solid black lines identify isotachs with a 10 $m\, s^{-1}$ step, depicting the superrotation structure, in particular the high-latitudes jets. White dashed lines identify the global cloud deck extending between cloud base (1 bar) and top (0.037 bar).

The zonal wind speed decrease with decreasing insolation is significant (see Table 3.1). The maximum zonal wind speed decreases from $\sim$ 84 $m\, s^{-1}$ at present-day Venus' orbital distance (0.72 AU) to $\sim$ 58 $m\, s^{-1}$ at 1.20 AU. However, the zonal wind structure remains present in all four studied orbital distances: the location of the high-latitudes jets is consistent, and the superrotation structure occupies the same pressure range with its core's base located just above the cloud top ($p \sim 0.037$ bar). Superrotation is a robust dynamical feature for the range of insolation values explored (ratio $[\overline{u}] : v_t$ in Table 3.1).

Table 3.1: Maximum zonal wind speed at four orbital distances of Venus simulated with the Generic-GCM

Orbital distance r, $[AU]$	Rotation rate Ω, $[rad\, s^{-1}]$	Tangential velocity $^{(1)}$ v_t , $[m\, s^{-1}]$	Maximum zonal wind speed $^{(2)}$ $[\overline{u}]$, $[m\, s^{-1}]$	Ratio $[\overline{u}] : v_t$
0.72	$2.98 \cdot 10^{-7}$	1.80	83.8	46.6
0.90	$2.15 \cdot 10^{-7}$	1.30	63.9	49.2
1.00	$1.84 \cdot 10^{-7}$	1.11	65.8	59.3
1.20	$1.40 \cdot 10^{-7}$	0.85	57.5	67.6

Notes: (1) At the planet's equator; (2) GCM wind speeds are relative to the planetary surface.

The following section will expand these initial considerations by simulating the same Venus-like atmosphere in a different astronomical setting.

3.2 3D Climate modelling of TRAPPIST-1 c with a Venus-like atmosphere

This section will present the result of modelling exoplanet TRAPPIST-1 c with a Venus-like atmosphere and assuming that the planet is a synchronous rotator. Unless contrary information is given, all data in this section is time-averaged over a period of 10 orbits of TRAPPIST-1 c (one orbit of TRAPPIST-1 c equals 209 000 s or approximately 2.42 Earth days). Moreover, all results in this section correspond to the reference simulation, obtained after one thousand orbits of TRAPPIST-1 c, initialised with a global-mean temperature profile obtained from the quasi-convergent simulation described in **section 2.4.1**.

3.2.1 Thermal structure

The global temperature profile of TRAPPIST-1 c in Figure 3.3 represents the mean thermal structure of the planet's atmosphere. Since I am assuming TRAPPIST-1 c to be tidally-locked, I decided to better represent the planet's thermal structure by comparing the global temperature profile with the nightside hemisphere, substellar region, and nightside equatorial temperature profiles.

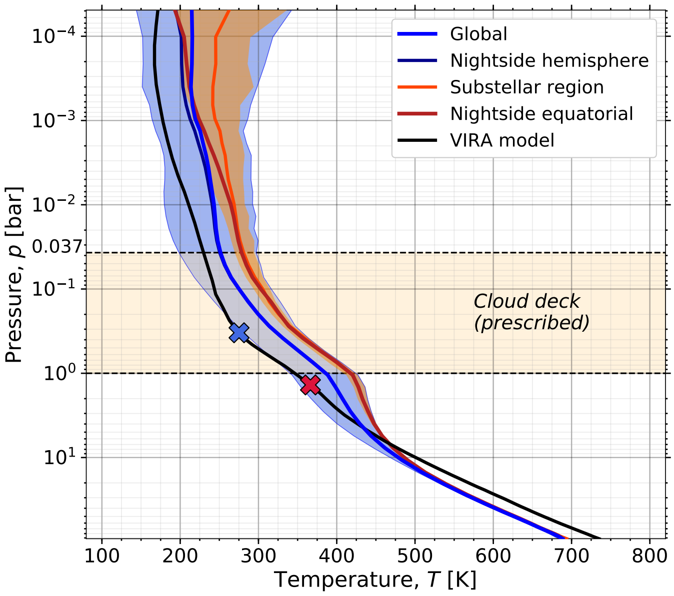

Figure 3.3: Temperature profiles in K for the reference simulation of TRAPPIST-1 c with a Venus-like atmosphere: (i) global (solid blue curve); (ii) nightside hemisphere (solid dark blue curve); (iii) substellar region (solid orange curve), spatially averaged over latitudes [22.5° S x 22.5° N] and longitudes [22.5° W x 22.5° E]; and (iv) nightside equatorial (solid dark red curve), latitudinally-averaged over [22.5° S x 22.5° N]. The data is time-averaged throughout ten TRAPPIST-1 c orbits (one orbit equals 209 000 s, approximately 2.42 Earth days). The shaded areas represent the temperature value range (the maximum and minimum value amongst *all* latitudes) per pressure level for the global and substellar region profiles. For comparison with Venus, a solid black line represents the Venus International Reference Atmosphere (VIRA) temperature profile (Keating et al., 1985; Seiff et al., 1985). The red (blue) cross over the VIRA profile indicates the approximate pressure level of the condensation (freezing) point (see text for details) of sulphuric acid on Venus. Additionally, two dashed black lines limit the prescribed global cloud deck (pale orange background) between cloud base (1 bar) and top (0.037 bar).

The largest temperature differences occur between the global and substellar region temperature profiles. The two profiles are adiabatic and very similar below $\sim$ 15 bar (temperature difference of $\sim$ 5 K and lapse rate of $\sim$ 9.2 K/km); however, the two diverge above $\sim$ 15 bar. Between this level and the cloud base (1 bar), the substellar region lapse rate is smaller ($\sim$ 4.5 K/km) than the global's

($\sim$ 5.8 K/km). Above the cloud base, the two lapse rates become similar, with the substellar region temperature profile being consistently *warmer* (on average, $\sim$ 27 K warmer) than the global profile. Above the cloud top ($p \sim$ 0.037 bar), the temperature variations are slight for both profiles (less than 2 K/km).

The global and nightside hemisphere temperature profiles are very similar for pressures higher than $\sim$ 10 $mbar$, with a maximum temperature difference of $\sim$ 2 K (on average 0.3 K) between the two profiles. The largest temperature difference occurs in the top-of-the-atmosphere, reaching $\sim$ 20 K. In contrast, the nightside equatorial temperature profile is remarkably similar to the substellar region profile from the ground to $\sim$ 10 $mbar$ (temperature differences are lower than 5 K). Moreover, between $\sim$ 15 bar and $\sim$ 10 $mbar$, the nightside equatorial region is *warmer* than the remaining nightside hemisphere, which as a whole, is closer to the global temperature profile. A warmer nightside equatorial region suggests warm air advection from the dayside. The heat advection is so efficient that it brings the temperatures in the equatorial nightside region to values close to those of the substellar region for a significant part of the atmosphere. Between 10 $mbar$ and 1 $mbar$, the nightside equatorial temperature profile approaches the global and nightside hemisphere temperature profiles, remaining close to the nightside hemisphere profile above $\sim$ 1 $mbar$.

The Venus International Reference Atmosphere (VIRA) temperature profile is plotted for comparison in Figure 3.3. This temperature profile (Keating et al., 1985; Seiff et al., 1985) is overall *colder* than the temperature profiles of TRAPPIST-1 c, except for the deep atmosphere where it becomes *warmer* at $\sim$ 5 bar (versus the global and nightside hemisphere temperature profiles) and $\sim$ 7 bar (versus the substellar region and nightside equatorial temperature profiles). The VIRA and TRAPPIST-1 c's global lapse rates have similar values, except between 1 bar and $\sim$ 10 bar, where the VIRA lapse rate is larger.

The results point out to a globally warmer TRAPPIST-1 c atmosphere than Venus's VIRA (see the blue shaded area in Figure 3.3). Therefore, a *warmer* TRAPPIST-1 c atmosphere requires a validity assessment on the prescribed cloud model. For this purpose, understanding the atmospheric levels where sulphuric acid aerosols (a major component of the prescribed cloud deck aerosol modes) undergo phase transition is essential to set the cloud base altitude, defined by the limit where sulphuric acid droplets evaporate.

The sulphuric acid phase transitions are represented under Venus-like sulphuric acid weight per cent conditions at approximate altitudes in the VIRA profile for condensation and freezing (respectively red and blue crosses on Figure 3.3). Sulphuric acid condensation in Venus takes place near the cloud base at $\sim$ 48 km (corresponding to p = 1.375 bar, T = 366.4 K in the VIRA temperature profile) (Titov et al., 2018), while sulphuric acid freezing (Gable et al., 1950; Keating et al., 1985; McGouldrick et al., 2011; Pollack et al., 1993; Seiff et al., 1985; Titov et al., 2018) occurs at $\sim$ 58 km (corresponding to p = 0.331 bar, T = 275.2 K in the VIRA temperature profile). According to Titov et al. (2018) (Figure 36, pp. 49, and associated text), this region between $\sim$ 48 km and $\sim$ 58 km constitutes the Venusian lower and middle cloud deck (condensational), while above it (until $\sim$ 70 km) is the Venusian upper (photochemical) cloud deck. While the TRAPPIST-1 c temperature profiles are *warmer* than VIRA's throughout the cloud deck, the temperature is particularly relevant for setting the cloud base level (personal discussion with *Emmanuel Marcq*).

The temperature in the prescribed cloud base level (Figure 3.3) is *warmer* than the sulphuric acid condensation point for any TRAPPIST-1 c temperature profile compared to VIRA (assuming a sulphuric acid weight per cent of $\sim$ 80%). Thus, the warmer cloud base suggests that sulphuric acid cloud formation and stability at this level is unlikely under TRAPPIST-1 c conditions. Additionally, the overall warmer substellar temperature profile suggests that cloud base level might be displaced upwards in this region and that cloud formation might occur at lower levels in the nightside hemisphere (comparatively to the substellar point), given its overall lower temperature. However, a realistic cloud formation and evolution would require a simple cloud model, including condensation and evaporation under a fixed particle size (i.e., a cloud model with macroscopic thermodynamical conditions without simulating growth at the droplet level). The simple cloud model is also crucial for defining the cloud top pressure, which arises from concurrent physical processes such as the photochemical production of upper haze, sedimentation and coalescence; however, such a model is out of scope for this work but foreseen in follow-up studies.

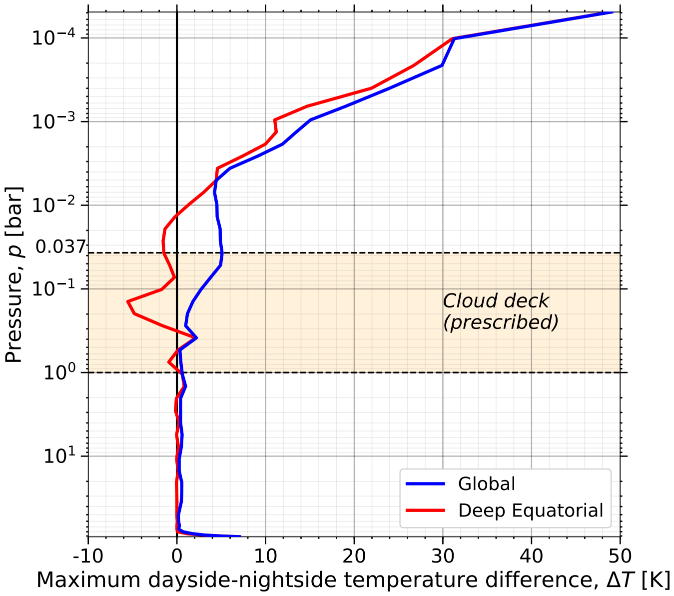

Figure 3.4: Maximum dayside-nightside temperature difference in K as a function of pressure for the global (all latitudes, solid blue curve) and the deep equatorial region (between 3.75° S and 3.75° N, solid red curve). Temperature differences are calculated at each latitude and pressure level, with the maximum latitudinal difference at a given pressure level shown in the figure. The data is time-averaged for ten TRAPPIST-1 c orbits. The solid vertical black line marks the zero temperature difference. The contribution from the terminators (90° W and 90° E) is not considered in the calculations. Two black dashed lines limit the prescribed global cloud deck (pale orange background) between the cloud base (1 bar) and cloud top (0.037 bar).

The modelled TRAPPIST-1 c Venus-like atmosphere also experiences significant day to night temperature differences, as seen in Figure 3.4. The maximum day-night temperature difference occurs at 0.05 $mbar$, the uppermost layer of the atmosphere, reaching almost 50 K. The stellar irradiation dominates the radiative balance above the clouds, creating a large day-night temperature contrast. Additionally, the large day-night temperature difference in the uppermost layers suggests a less efficient heat transport due to lower atmospheric density. The substantial day-night temperature variation starts at altitudes inside the cloud deck, reaching $\sim$ 5 K for the global profile. For the deep equatorial (between 3.75° S and 3.75° N) profile, there is a cloud deck region between 0.1 bar and 0.3 bar where nightside temperatures are larger (peaking at $\sim$ - 5.5 K) than dayside temperatures. At these levels, the larger nightside temperatures could result from a net heat redistribution by the equatorial zonal superrotation jet.

3.2.2 Radiative tendencies

Figure 3.5 identifies the net cooling and heating (solid black dashed lines) regions of the atmosphere for two different latitudinal bands: the deep equatorial region (from 3.75° S to 3.75° N) and the mid-northern latitudes (from 45° N and 60° N). The aim is to evaluate the impact of the expected dynamical regimes in the atmosphere's energy balance, particularly in the equatorial zonal superrotation jet and high-latitudes jet regions.

The short-wavelength (SW) heating rate (orange curves in Figure 3.5) contribute to the warming of the atmosphere. The SW heating rate gradually decreases from the top to the ground by more than four orders of magnitude. The long-wavelength (LW) heating rate (red curves in Figure 3.5) contributes to the overall cooling of the atmosphere, except for a region inside the cloud deck, where the LW heating rate leads to local warming in the vicinity of the cloud base. While the LW local warming is present in both latitudinal regions, it only extends below the limits of the cloud base for the mid-northern latitudes. As for the deep equatorial region, an additional layer of LW heating is located at about 4 bar. These LW warming layers are not present in simulations without clouds (i.e., clear-sky simulations), suggesting that aerosol particles might be contributing to this local warming. The causing mechanism involves the emission of LW radiation by the hot planetary surface, followed by its absorption at the cloud base, in an agreement to the results in Lebonnois et al. (2010) and Lebonnois et al. (2015).

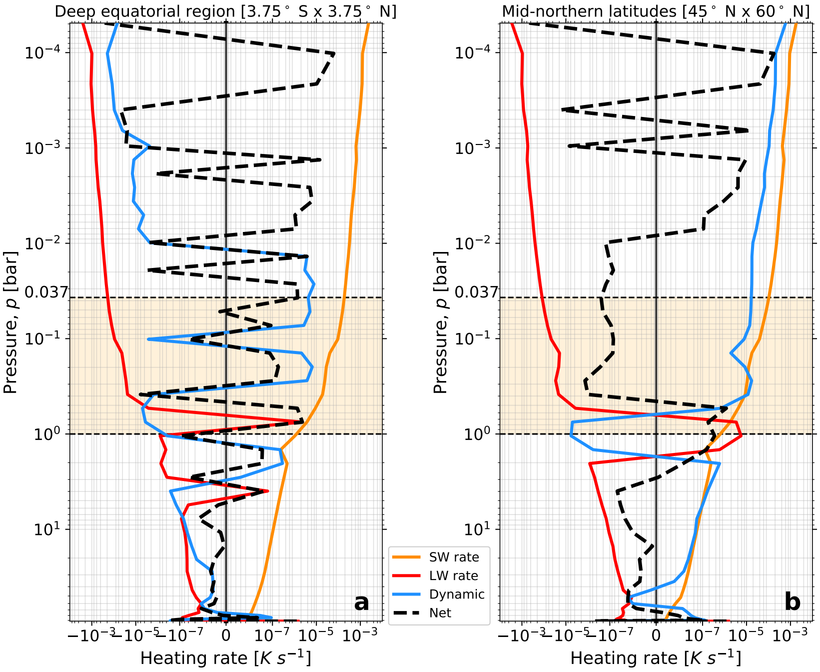

Figure 3.5: Zonal and time-averaged heating rates in Ks^{-1} for TRAPPIST-1 c as a function of pressure for cases: short-wavelength (SW rate), long-wavelength (LW rate) and dynamical rates (Dynamic), depicted as orange, red, and solid blue lines, respectively. Additionally, the net heating rate is represented by a dashed black line. The radiative tendencies are time-averaged throughout ten TRAPPIST-1 c orbits. The data is also zonally-averaged for two latitudinal regions: (i) the deep equatorial region (between 3.75° S and 3.75° N) in the left panel **(a)**; (ii) the mid-northern latitudes (between 45° N and 60° N) in the right panel **(b)**. Positive (negative) heating rate values correspond to warming (cooling) regions. Two black dashed lines limit the pressure range of the global cloud deck (pale orange background) between cloud base (1 bar) and cloud top (0.037 bar).

The dynamics heating rate (solid blue curves in Figure 3.5) show a complex behaviour in the deep equatorial region, with alternating warming and cooling layers. This complexity adds to the significant variations seen in the net heating rate (dashed black curves in Figure 3.5). In opposition, the dynamic heating rate in the mid-northern latitudes contributes to the atmosphere's overall warming, with the most notable exception being the cooling in the cloud base region.

To interpret these warming/cooling transitions, I decided to compare the dayside and nightside heating rates, as shown in Figure 3.6. For simplicity, I will focus the analysis on the cloud base level in the vicinity of 1 bar. The net warming in the dayside deep equatorial region (panel **a**) results from LW and dynamical contributions, which peak at different pressure levels. Conversely, at the dayside mid-northern latitudes (panel **b**), there is net warming at 1 *bar* resulting from a local maximum in the LW heating rate, overcoming the local dynamical cooling. In the same latitudinal range, the net warming seen below the cloud deck results from a dynamical effect.

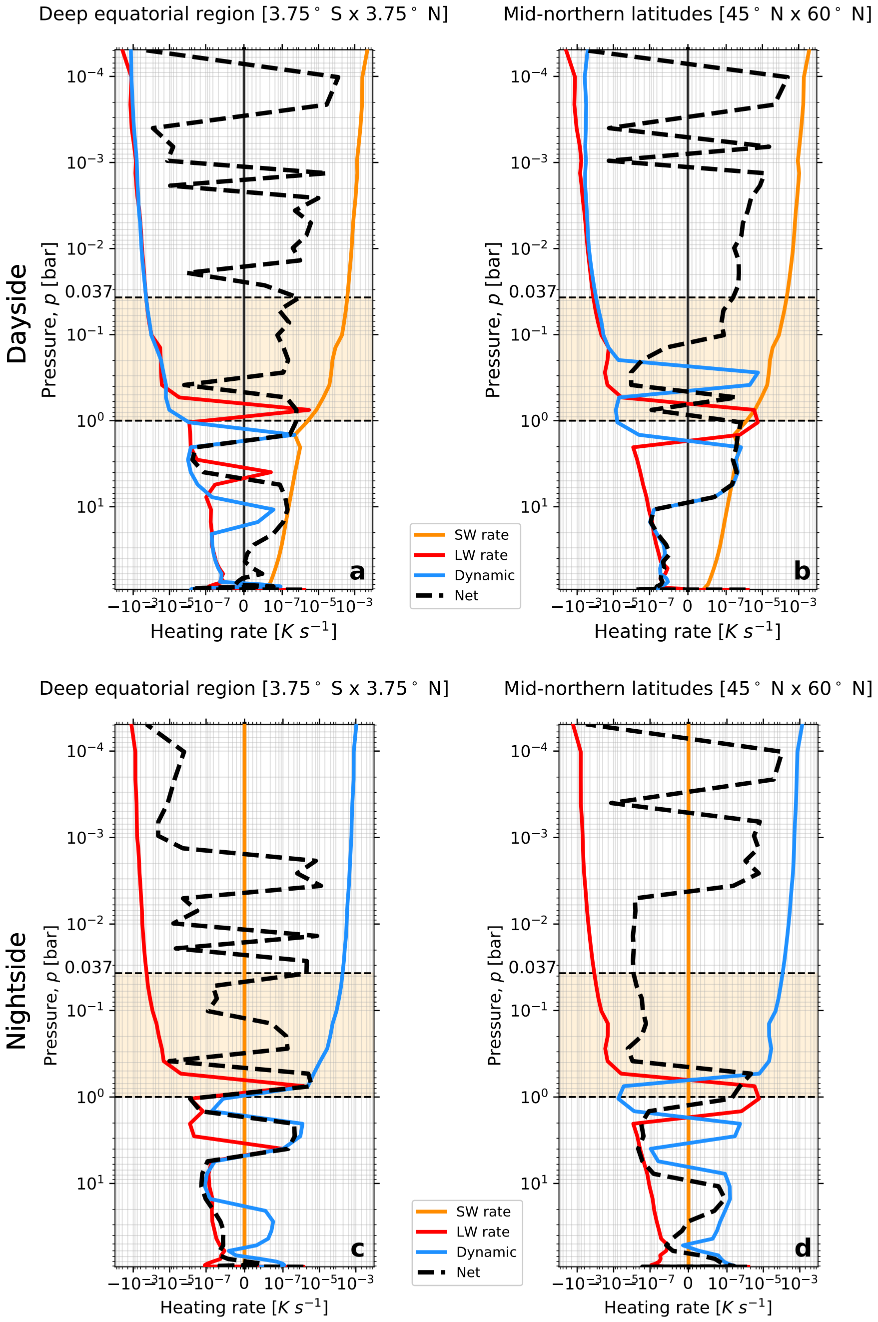

Figure 3.6: Same as Figure 3.5 but with zonal and time-averaged dayside (panels **(a, b)**) and nightside (panels **(c, d)**) radiative tendencies for TRAPPIST-1 c, at two different latitudinal regions.

On the nightside (panels **(c, d)**), the contribution from the SW heating rate is zero. The LW and dynamical heating rates balance at each level, as the net warming and cooling regions are probably the result of random fluctuations: the net warming and cooling values are orders of magnitude smaller than the LW and dynamical heating rates. Another aspect is that the LW warming at the cloud base is a feature present in both hemispheres (dayside, nightside) and on the two latitudinal ranges. As previously discussed, this local warming agrees with a global cloud cover absorbing the LW radiation emitted by the hot surface. The division between dayside and nightside has not explained the 4 *bar* LW heating seen in the deep equatorial region, whose origin will require further investigation.

3.2.3 Temperature field and variability at the cloud tops

The time-mean temperature field at the cloud top has a distinctive **chevron-shaped pattern** (see Figure 3.7). The feature is symmetric around the equator, with an apex centred in the substellar point (white star) region, extending towards the evening terminator (90° E) in the northeast and southeast directions. Additionally, there is an **eastward shift of the temperature maximum** along the equator from the substellar point towards the region east of the evening terminator. The highest temperatures occur along a band centred at the equator, between longitudes $\sim 20°$ E and $\sim 120°$ E. These two structures: the chevron-like pattern and the eastward shift of the temperature maximum, are characteristic from simulations of tide-locked planets (Showman and Polvani, 2011). Furthermore, the normalised horizontal wind field (black arrows in Figure 3.7) shows a chevron-like pattern coherent with the temperature field.

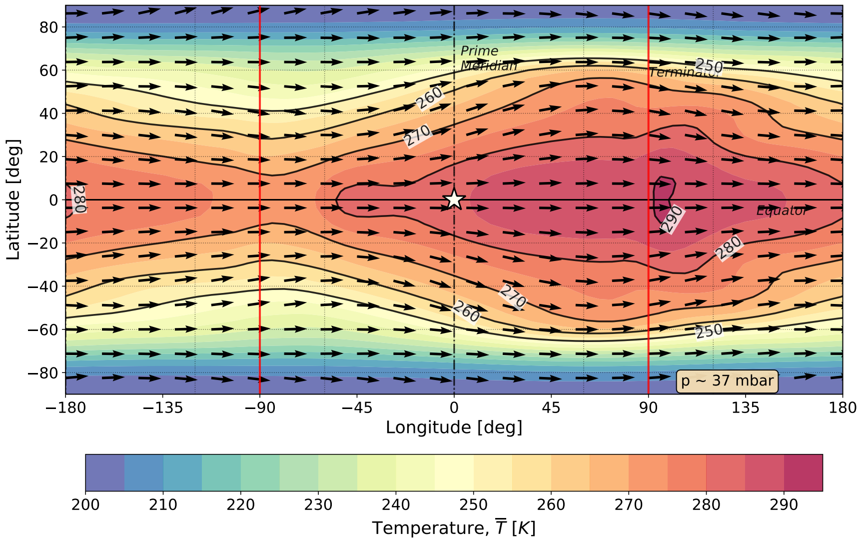

Figure 3.7: Time-mean temperature field in K at the cloud top (p $\sim$ 0.037 bar) averaged over ten orbits of TRAPPIST-1 c. The solid black lines represent the isothermals from 250 K to 290 K, with a step of 10 K. Black arrows represent the normalised horizontal wind vectors at the cloud top. The solid red lines depict the terminators at 90° W and 90° E, while the equator (prime meridian) is identified by a solid (dashed) black line. The white star marks the location of the substellar point (at 0° latitude and 0° longitude).

In addition to the eastward shift of the temperature maximum, regions of relative temperature maxima emerge in the cloud tops centred at $\sim 45°$ W and $\sim 150°$ E, and on the equator. These regions might be the result of adiabatic warming from local subsidence.

The cloud top temperature field also experiences variability, as represented in the *Hovmöller* diagram for the temperature perturbation along the equator (see Figure 3.8 panel **(a)**). Absolute maxima and minima of temperature perturbation occur in the vicinity of the 50° W region. In general, for the same longitude value, alternating maxima and minima of the temperature perturbation field suggest a distinctive **wave-like pattern**. This wave-like structure emerges from 50° W, and it propagates throughout the planet's equator in the *eastward* direction. While this structure is evident in the dayside, *west* of the 50° W region, its signature in the nightside can be *transient* (e.g., at the beginning of the ninth orbit of TRAPPIST-1 c).

A wave-like feature is identified in the panel **(b)** of Figure 3.8 by a blue arrow representing longitudinal and time ranges (between points A and B). The wave phase speed c can be estimated from the ratio between longitudinal and time differences, respectively: $\sim 140°$ and ~ 0.66 orbits of TRAPPIST-1 c, yielding $c \sim 212°/\ orbit$. Multiplying c for the equivalent distance to 1° at the equator ($\sim 122.1\ km$)

and converting it to SI units provides an estimate of this wave phase speed, $c \sim 124\ m\,s^{-1}$. Extending this analysis to several waves in a similar longitudinal range (from ~ 50° W to ~ 100° E) and throughout ten orbits of TRAPPIST-1 c, I estimate the average wave phase speed to be $\bar{c}$ = (129.6 ± 0.2) $m\,s^{-1}$. Additionally, the wave period can be estimated by measuring the time interval between two consecutive crests located at the same longitude. The analysis of several waves across the ten orbits period revealed a mean period, $\overline{T_w}$, of ~ 17.5 hours or ~ 30% of the orbital period of TRAPPIST-1 c.

The instantaneous temperature perturbation field (tenth orbit time-instant) in the panel (**c**) of Figure 3.8 shows, as expected, a series of positive and negative temperature anomalies spanning along the planet's equator cloud tops from the substellar to the antistellar point. The maximum latitudinal extension of these features is ~ 20° N/S, and each temperature anomaly has its maximum typically located at the equator or within ~ 10° N/S.

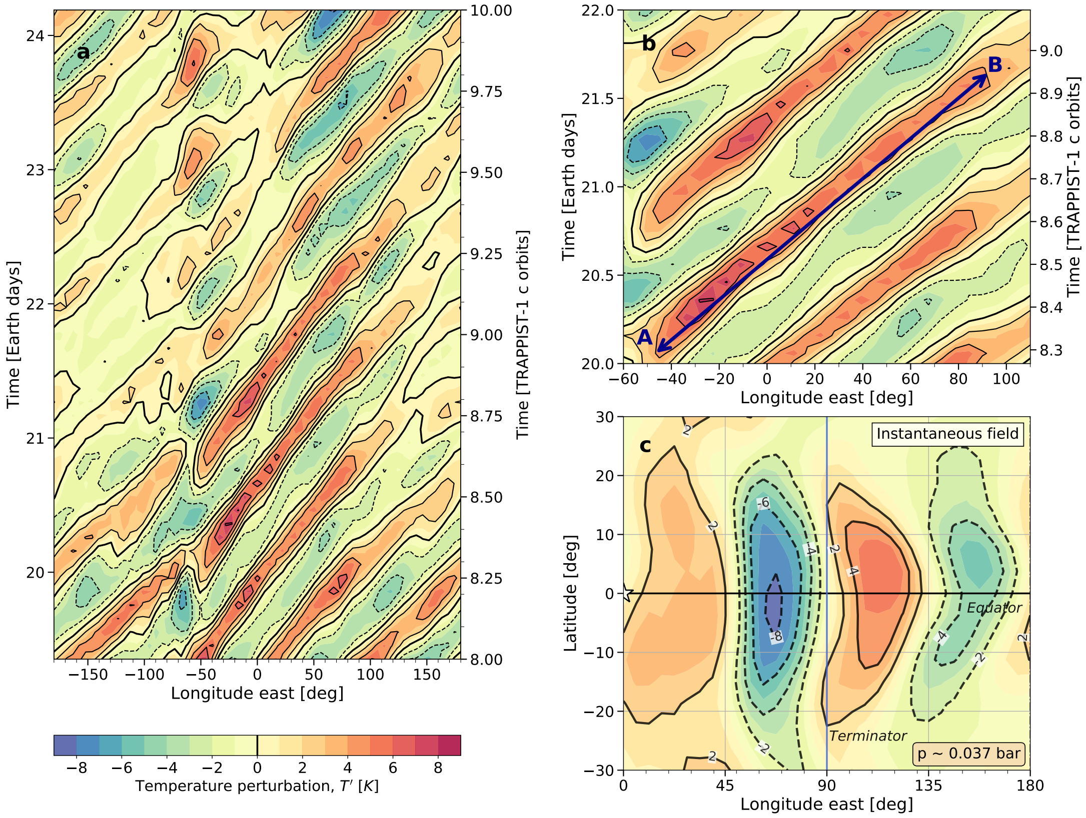

Figure 3.8: Hovmöller diagram of the temperature perturbation T' in K at the equator and cloud top ($p \sim 0.037$ bar): **(a)** along all longitudes and during two orbits of TRAPPIST-1 c; and **(b)** from 60° W to 110° E and from Earth day 20 to 22. Both panels represent time in the vertical axis in Earth days (left) and TRAPPIST-1 c orbits (right). In panel **(b)**, a two-head blue arrow represents the longitudinal and time extremes (points A and B) of a wave-like feature. In panel **(c)**, the cloud top instantaneous temperature perturbation field is depicted in latitude versus longitude. In all panels, the solid (dashed) black lines represent the temperature perturbation's positive (negative) isothermals. The thickest line in panels **(a, b)** represents the zero perturbation line, also depicted in the colour bar.

3.2.4 Zonal wind field

The main characteristics of the zonal wind field are the development of an **equatorial zonal superrotation jet** and two **high-latitudes jets**, both directed eastwards. These jets are dynamical features predicted for highly-irradiated synchronous rotators (Showman and Polvani, 2011). Both jets are present in the zonal and time-averaged zonal wind field, with their cores located in the uppermost layers of the atmosphere (Figure 3.9 **(a)**). Both jets are present at the cloud top layer, while the high-latitudes jets have a deeper penetration in the atmosphere, well within the cloud deck. Meridional gradients of the zonally-averaged zonal wind field are weak in the mid-latitudes between the jets above the cloud top and strong in the poleward flanks of the high-latitudes jets.

The equatorial zonal superrotation jet has a well-delimited core centred at equator between pressure layers 0.4 $mbar$ and 0.06 $mbar$, with a maximum speed slightly larger than 230 $m\,s^{-1}$. This jet extends down to the cloud deck level, gradually reducing its zonal-mean speed to $\sim$ 150 $m\,s^{-1}$ at the cloud top.

The high-latitudes jets have cores located between 60° to 70° latitude whose maximum speeds are less intense than the equatorial jet, having zonally-averaged speeds peaking at $\sim$ 210 $m\,s^{-1}$ at $\sim$ 0.1 $mbar$. In addition, unlike the equatorial jet, the high-latitudes jets have an equatorward tilted structure and their cloud top zonally-averaged speeds are faster ($\sim$ 165 $m\,s^{-1}$) than those in the equatorial zonal superrotation jet.

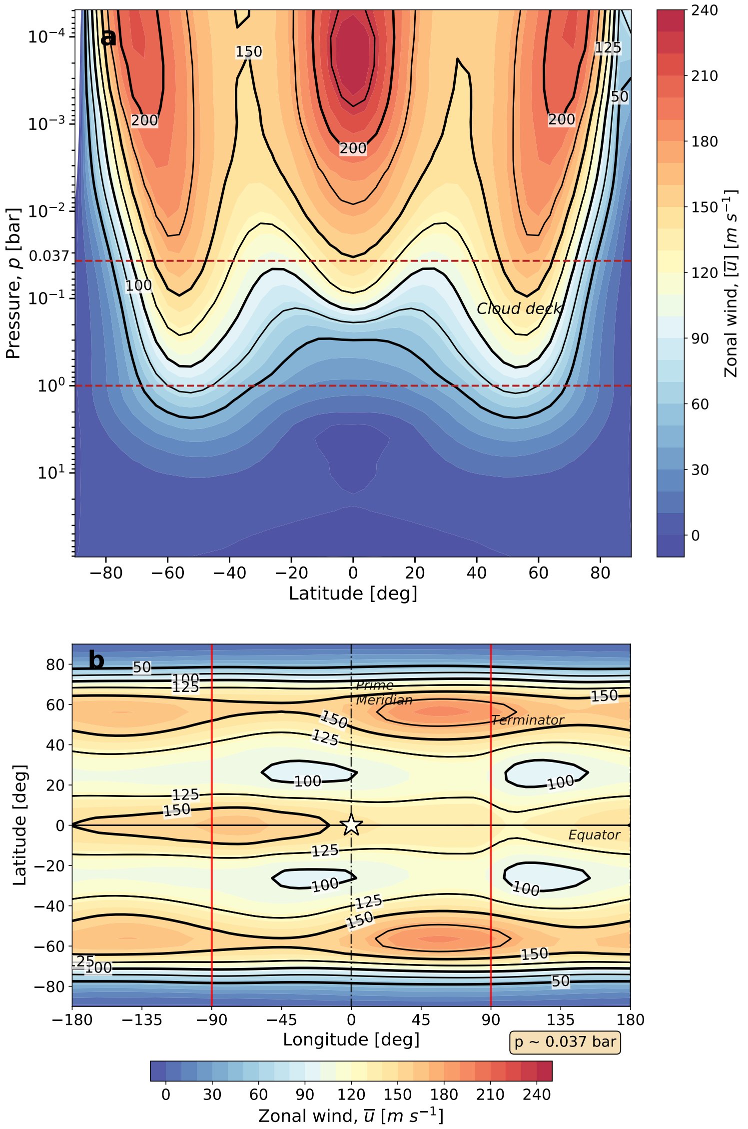

Figure 3.9: Time-mean zonal wind field in $m\,s^{-1}$ averaged over ten orbits of TRAPPIST-1 c: **(a)** zonally-averaged; and **(b)** at the cloud top ($p \sim 0.037$ bar). The solid thick (thin) black lines represent isotachs with a 50 $m\,s^{-1}$ (25 $m\,s^{-1}$) interval. In panel **(a)**, the red dashed lines represent the cloud deck located between 1 bar and 0.037 bar. In panel **(b)**, the solid red lines represent the terminator and the white star marks the substellar point (at 0° latitude and 0° longitude). The solid (dashed) black line marks the equator (prime-meridian).

Both jets are present in the cloud top, time-mean zonal wind field (Figure 3.9 **(b)**) and, as suggested by the zonally-averaged field (Figure 3.9 **(a)**), the high-latitudes jets are stronger at this level than the equatorial zonal superrotation jet. The former peaks at $\sim 190\ m\,s^{-1}$ just west of the evening terminator (90° E), while the latter peaks at $\sim 160\ m\,s^{-1}$ east of the morning terminator (90° W). The jets are well-defined and separated by a mid-latitude transition region ($\sim$ 30° N/S), where the zonal wind speeds decrease to as low as $\sim 100\ m\,s^{-1}$. The 125 $m\,s^{-1}$ isotach is particularly relevant for describing the width of each jet. For instance, the equatorial jet narrows at $\sim$ 100° E, keeping an almost constant width at remaining longitudes extending to about 20° latitude. The zonal wind speed reaches its minimum value at the jet's narrowest point, steadily increasing in speed until it reaches $\sim$ 60° W and gradually decelerates east of this region.

In opposition, the high-latitudes jet width variation is more substantial, with maximum equatorward expansion at $\sim$ 70° E in the dayside and $\sim$ 140° W in the nightside. The jet's zonal speed increases during this equatorward expansion (particularly in the dayside) and decreases as the jet narrows (at longitudes $\sim$ 45° W and $\sim$ 135° E).

The zonal variation in the jets' zonal wind speed occurs mainly above the cloud deck, as shown in the pressure versus longitude diagrams (see Figure 3.10). Therefore, to study the behaviour of the jets in altitude, I decided to represent four latitudes in Figure 3.10: (i) at the equator (0°), to capture the zonal modulations of the equatorial zonal superrotation jet; (ii) at 30° N, where there is a weakening of the time-mean zonal wind field; and (iii) at 45° N and 60° N, to capture the high-latitudes jet equatorward expansion (at $\sim$ 70° E and $\sim$ 140° W) and maximum speed (at $\sim$ 60° E) at the cloud top level.

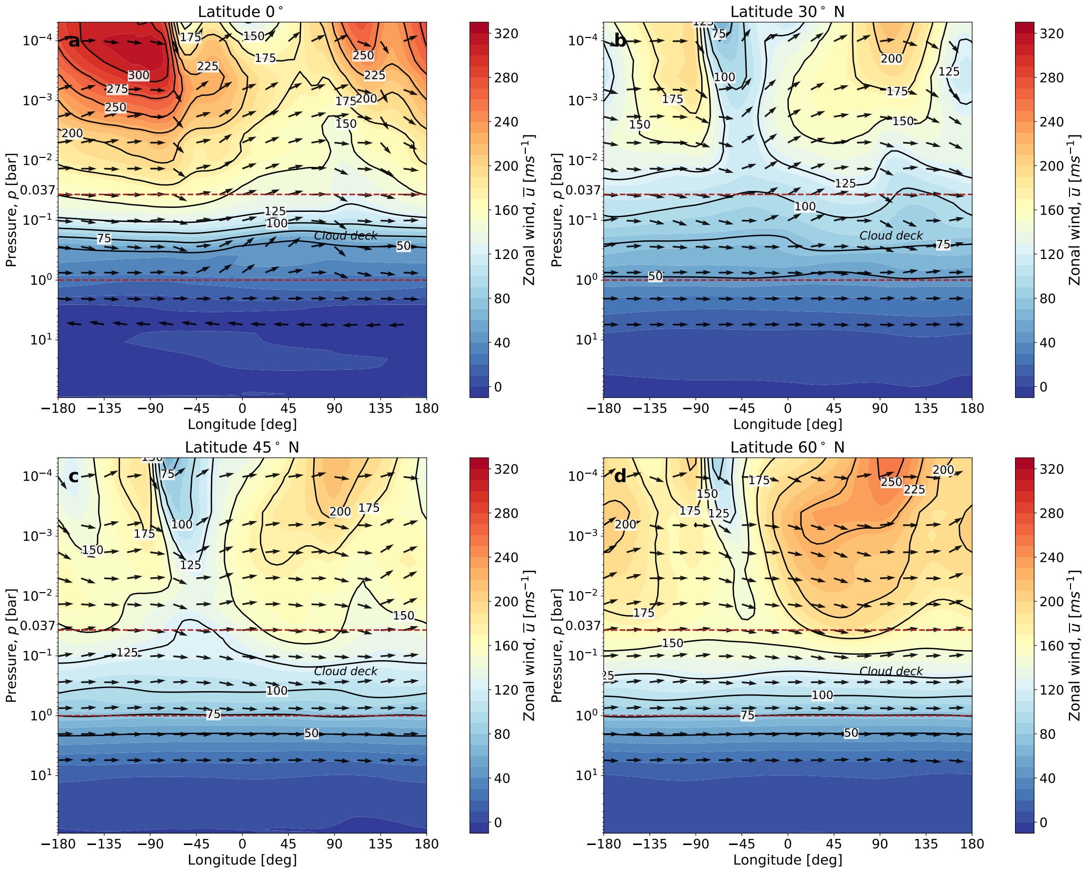

Figure 3.10: Time-mean zonal wind fields in $m\,s^{-1}$, averaged for ten orbits of TRAPPIST-1 c, as a function of pressure and longitude for four selected latitudes: **(a)** at 0°; **(b)** at 30° N; **(c)** at 45° N; and **(d)** at 60° N. The solid black lines represent isotachs with a 50 $m\,s^{-1}$ interval. The colour scheme is the same for every plot, with zonal wind speeds ranging from -10 $m\,s^{-1}$ to 330 $m\,s^{-1}$. The solid black arrows represent the normalised wind vectors of zonal, u, and vertical, w, components (the vertical component is multiplied by the ratio between the horizontal and vertical spacings). The cloud deck extends between 1 *bar* and 0.037 *bar*, represented by red dashed lines.

All selected latitudes in Figure 3.10 show an overall increase in zonal and vertical wind speeds in altitude due to the lower atmospheric mass. However, there is a more significant vertical wind shear $\mathrm{d}u/\mathrm{d}z$ at the equator than at higher latitudes. In addition, all panels show a more significant zonal wind shear $\mathrm{d}u/\mathrm{d}x$ above the cloud deck, which is strongest east of the morning terminator (centred at $\sim$ 60° W) associated with downward motion (black arrows), particularly in the uppermost levels of the atmosphere. At the equator, the zonal wind shear increases again in the vicinity of the evening terminator. In contrast, at 60° N significant zonal wind shear is present in the substellar region, leading to larger zonal wind speed values of the high-latitude jet east of the substellar point than other selected latitudes.

The largest zonal wind speeds occur at the equator in the nightside between the antistellar point and the morning terminator. In the uppermost levels (centred at $\sim 0.1\ mbar$), the equatorial zonal superrotation jet speeds can reach up to $\sim 310\ m\,s^{-1}$, followed by strong zonal wind shear east of the morning terminator. This wind shear leads to a decrease in zonal wind speed in the substellar point region. Still, most of the atmosphere above the cloud deck in the equatorial substellar region has zonal wind speeds that exceed 150 $m\,s^{-1}$. In the evening terminator, the jet speed increases for altitudes above $\sim 2\ mbar$ and decreases for altitudes below it. Thus, the decrease in the equatorial jet speed seen at the cloud top level for the evening terminator (Figure 3.9 **(b)**) is not accompanied by the uppermost levels of the atmosphere. East of the evening terminator, jet speeds in altitude are significant, reaching $\sim 270\ m\,s^{-1}$, however smaller when compared to the morning terminator region.

Inside the equatorial cloud deck, there is a strong vertical wind shear $\mathrm{d}u/\mathrm{d}z$ occupying its top half section, leading to a rapid decay in zonal wind speed towards lower altitudes. This strong vertical wind shear is present only at the equator. For instance, comparing the 50 $m\,s^{-1}$ isotach position between latitudes provides an assessment of the magnitude of the zonal wind speed decay with altitude. Consequently, the 50 $m\,s^{-1}$ isotach location is shallower at the equator ($\sim 0.3\ bar$), becoming progressively deeper for higher latitudes, eventually reaching the 2 bar level at 60° N. Additionally, for all selected latitudes, zonal and vertical wind shear decrease with decreasing altitude inside the cloud deck. This decrease in wind shear results from less SW radiation reaching the deepest levels of the atmosphere.

All panels, excepting the 30° N, show that the equatorial and high-latitudes jets have deep penetration in the atmosphere, reaching well within the cloud deck. Furthermore, the zonal wind speeds above the cloud deck in the 0° and 60° N cases are, with a few exceptions, faster than 150 $m\,s^{-1}$. The systematically larger zonal wind speeds across all longitudes highlights the equatorial and high-latitudes jets' potential for zonal momentum transport across the planet and throughout a significant portion of the atmosphere.

Unlike the equatorial jet, the high-latitudes jet at 60° N has the largest speeds in the region between the substellar point and 135° E, peaking slightly above 250 $m\,s^{-1}$ just east of the evening terminator. The equatorward expansion of the high-latitudes jet is visible in the 45° N panel, where an increase in zonal wind speed occurs at $\sim$ 70° E and $\sim$ 140° W.

In the latitudes between the two jets, at 30° N, the zonal wind field is directed eastwards, but it is overall less intense as suggested in Figure 3.9 **(b)**. However, even at this latitude, day-night zonal wind speed contrasts are visible in the uppermost layers (above $\sim 3\ mbar$), where zonal wind shear is substantially larger compared to the cloud top.

Finally, two main characteristics of the vertical wind field seen in Figure 3.10 are the upward motion present in the substellar region and the two downdrafts close to the terminators (at the equator, there is an additional downdraft at $\sim$ 135° E). The substellar region upwelling is relevant at the equator and mid-latitudes, and it is replaced at 60° N by downward motion. The downdraft near the morning terminator is present at all selected latitudes, although stronger at the equator (maximum downdraft speeds reach

$-40\ cm\,s^{-1}$ at the equator). This downdraft coincides with the strong zonal wind shear feature east of the morning terminator. These downdrafts will lead to adiabatic warming, explaining the temperature maxima seen at the equator cloud top (in Figure 3.7) at $\sim 45°$ W and $\sim 150°$ E. These hot spots are eastward of the downdrafts, suggesting warm air advection by the equatorial zonal superrotation jet.

3.2.5 Meridional circulation

For a tide-locked planet, the day-night heat redistribution is mostly done by the superrotation jets (Charnay et al, 2015). However, understanding the large-scale circulation and heat redistribution in a synchronous rotator requires a further study of the meridional day-night circulation. To do so, I calculated the zonal mean mass streamfunction and represented it in Figure 3.11.

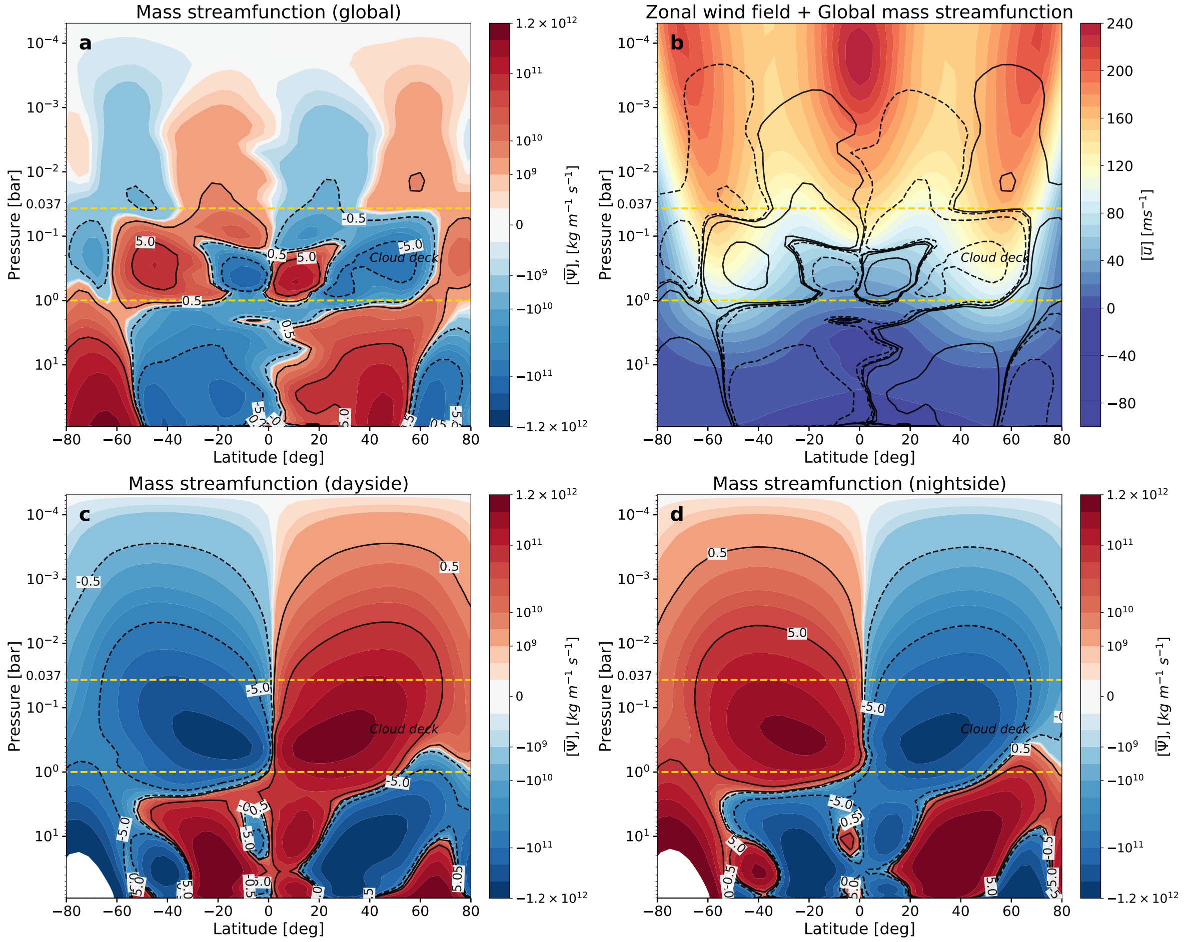
Mass streamfunction (global)
Zonal wind field + Global mass streamfunction
Mass streamfunction (dayside)
Mass streamfunction (nightside)

Figure 3.11: Zonal and time-averaged mass streamfunctions, $[\overline{\Psi}]$, in $kg\ m^{-1}\ s^{-1}$ over ten orbits of TRAPPIST-1 c, for three cases: global **(a, b)**; dayside **(c)**; and nightside **(d)**. The dayside and nightside mean mass streamfunctions exclude the terminator longitudes (90° E and 90° W) in their integration, while the global mean mass streamfunction includes all longitudes. The global mean mass streamfunction is the sum of the dayside and nightside longitudes, plus the contribution from the two terminators. Positive (negative) values, i.e., in red (blue), correspond to clockwise (anti-clockwise) circulation. Black contours in solid (dashed) lines represent positive (negative) values: $\pm 5\cdot 10^{10}$ or $\pm 0.5\cdot 10^{10}\ kg\,m^{-1}\,s^{-1}$. An additional contour of $\pm 0.05\cdot 10^{10}\ kg\,m^{-1}\,s^{-1}$ in panel **(b)** helps representing the mean mass streamfunction in the upper atmosphere. Also, for panel **(b)**, the colour scheme is replaced by the zonal and time-averaged (all longitudes, ten orbits) zonal wind field. The yellow solid lines represent the cloud deck, extending between cloud base ($1\ bar$) and cloud top ($\sim 0.037\ bar$).

Two large **Hadley cells** are present in the dayside hemisphere, penetrating deep in the atmosphere below the cloud deck level ($\sim 2\ bar$), with each cell extending from the equator to the pole. Conversely, the nightside hemisphere also shows two large cells; however, the mean meridional circulation in this hemisphere is reversed compared to the dayside. Thus, an **Hadley type circulation** characterises the dynamics of the dayside hemisphere, while an **anti-Hadley type circulation** characterises the dynamics of the nightside hemisphere. This large-scale circulation has been described by Charnay et al. (2015) when simulating the Climate of a warm sub-Neptune planet.

Furthermore, the dayside hemisphere has a zonally-averaged poleward circulation, while in the nightside hemisphere, the zonally-averaged circulation is equatorward. Both circulations are symmetrical concerning the equator. Thus, the mean meridional circulation drives warm air away from the equatorial dayside region. As a result, the air masses are carried across the poles, descending towards the equatorial region in the nightside.

The mean meridional circulation division in dayside and nightside hemispheres reveals a large-scale atmospheric circulation dominated by one large cell per hemisphere. The mean meridional circulation comprises two large cells, one in the northern and the other in the southern hemisphere. Each cell crosses the polar region, redistributing heat from dayside to nightside.

Since the dayside and nightside hemispheres have large circulations in opposite directions, the global mean mass streamfunction allows the interpretation of which circulation dominates locally. The dayside circulation is dominant above the cloud top for latitudes above $\sim$ 40° N/S. In opposition, the nightside circulation is dominant in the lower latitudes, extending deep into the cloud deck (at $\sim$ 0.2 bar). As a result, the interpretation of the dominant circulation inside the cloud deck is more complex. In the cloud deck's equatorial region (latitudes lower than 20° N/S), the dayside circulation dominates only between 1 bar and 0.2 bar. In the cloud deck mid-latitudes (between 20° N/S and 60° N/S), the nightside circulation dominates, while the dayside circulation dominates in the polar regions (latitudes above 60° N/S).

The global mass streamfunction follows the time and zonally-averaged zonal wind field (Figure 3.11 **(b)**) as the equatorial and high-latitudes jets form at the boundary of the cells, according to conservation of angular momentum.

Globally, the meridional circulation will transport energy from the low to high latitudes. Figure 3.12 **(a)** shows the impact from the meridional atmospheric energy transport in the zonal mean difference between the outgoing long-wavelength radiation (OLR) emitted by the planet and the absorbed stellar radiation (ASR). Positive (negative) values in Figure 3.12 **(a)** correspond to regions with net energy income (outcome) by the meridional circulation compared to the radiative equilibrium (black dashed line in the Figure 3.12 **(a)**). The meridional circulation leads to a net heat redistribution from ASR excess regions (negative values, low latitudes) to OLR excess regions (positive values, higher latitudes).

The total heat flux transported by the meridional circulation can be decomposed into three main components of the heat flux transported by the: (i) mean meridional circulation; (ii) stationary waves; and (iii) transient perturbations; the respective terms in the right-hand of expression:

$$[\overline{sv}] = [\overline{s}]\,[\overline{v}] + [\overline{s}^{*}\,\overline{v}^{*}\,] + [\,\overline{s'v'}\,] \tag{3.1}$$

Where s is the dry static energy, $s = (c_pT + gz)$, and v is the meridional wind. The overbars are time averages and the primes are the deviations from time averages. The square brackets are zonal averages and the asterisks are departures from zonal averages (following the nomenclature in Peixoto and Oort (1992)). The total heat flux and its components are vertical (ground to top-of-the-atmosphere) and zonally-integrated in Figure 3.12 **(b)**.

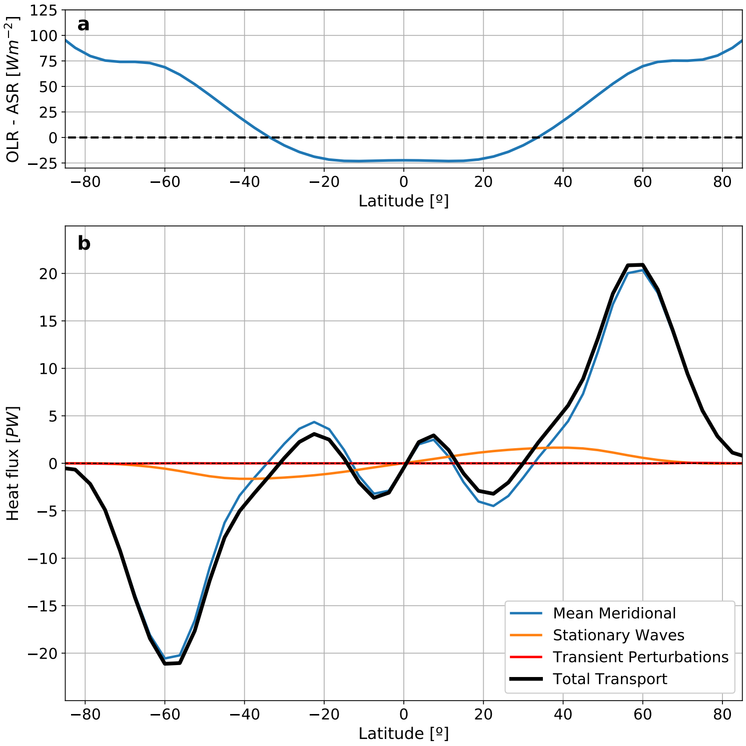

Figure 3.12: Mean heat transport by the meridional circulation averaged throughout ten orbits of TRAPPIST-1 c. In the upper panel **(a)**, the zonal-mean difference between the outgoing long-wavelength radiation (OLR) and the absorbed stellar radiation (ASR): positive (negative) OLR - ASR values correspond to regions globally warmed (cooled) by the meridional circulation. The bottom panel **(b)** presents the vertical and zonally-integrated total heat transport in PW (i.e., 1 $PW = 10^{15}$ W) (solid black line) and its decomposition in the three main components of the heat flux transported by the: (i) mean meridional circulation (solid blue line); (ii) stationary waves (solid orange line), and (iii) transient perturbations (solid red line). Positive (negative) values correspond to northward (southward) heat fluxes.

The heat flux transported by the mean meridional circulation mainly explain TRAPPIST-1 c total meridional heat transport. The stationary waves significantly impact the mid-latitudes by enhancing the poleward energy transport. On the other hand, the heat flux transported by transient perturbations has a negligible impact, being about three orders of magnitude lower than the other two heat flux components.

3.2.6 TRAPPIST-1 c synthetic observables

To address the observational prospects of TRAPPIST-1 c, I used the GCM outputs to obtain two types of synthetic observables: the emission and reflection phase curves and the transmission spectra. Since TRAPPIST-1 c is a transiting planet (Gillon et al., 2016, 2017), transmission spectroscopy is a valuable technique that can complement results from emission and reflection phase curves.

Reflection and emission phase curves Reflection phase curves help detect and analyse inhomogeneities in the cloud system as clouds impact the albedo as discussed in Turbet et al. (2016). However, I have assumed a global cloud deck and no photochemistry reactions in this work, which could have impacted the time and local cloud formation, imposing variability in the system. Therefore, the reflection phase curves presented in this work are a first approximation of what we can expect from a cloudy, Venus-like exoplanet. Figure 3.13 presents the computed reflection phase curves for TRAPPIST-1 c, under the assumption of a synchronous rotator.

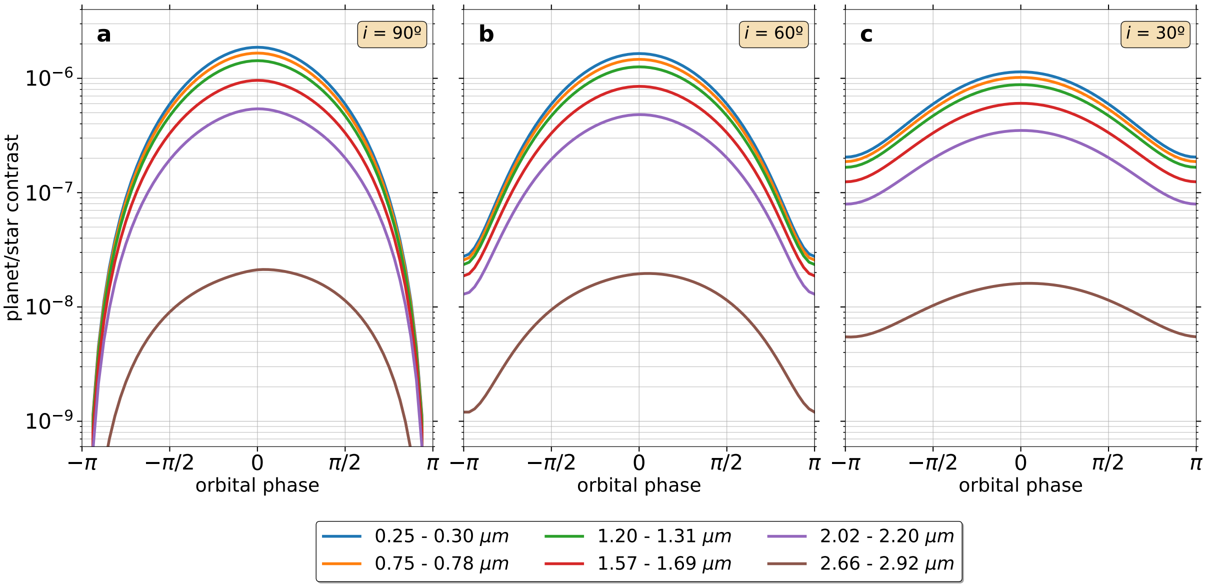

Figure 3.13: The reflection phase curves presented in planet-to-star contrast ratio as a function of the orbital phase of TRAPPIST-1 c with a Venus-like atmosphere. The data is time-averaged for ten orbits and presented for three inclinations (i): **(a)** 90°; **(b)** 60° ; and **(c)** 30°. Six spectral bands are represented, ranging from the UV to the MIR region of the electromagnetic spectrum.

The planet-to-star contrast in the reflection phase curves will depend on the illumination fraction of the planet's Earth-facing hemisphere. The largest planet-to-star contrast occurs in the orbital phase 0([20]), i.e. when the Earth-facing hemisphere is fully illuminated. Conversely, the lowest planet-to-star contrast happens when the planet is at the orbital phase $-\pi$ or π, corresponding to the planetary transit. Moreover, if the planet's albedo is isotropic, the reflection phase curves are expected to be symmetric around the orbital phase 0. This phase curve symmetry occurs for most of the spectral bands in Figure 3.13, except for the 2.66 - 2.92 μm phase curve. This asymmetry is caused by the 2.8 μm carbon dioxide absorption band. However, not every carbon dioxide absorption band is strong enough to cause reflection phase curve asymmetry: the weaker 2.2 μm carbon dioxide absorption band has a negligible impact on the symmetry of the 2.02 - 2.20 μm spectral band.

Overall, the reflection phase curves of TRAPPIST-1 c show, as expected, a higher planet-to-star contrast in the short wavelengths. Additionally, the largest contrast values obtained for TRAPPIST-1 c in this study are on the order of 10^{-6}. The reflection contrast values are almost one order of magnitude larger than the ones calculated by Turbet et al. (2016) for Proxima Centauri b (thus considering a different exoplanet, orbital distance and stellar irradiance from the host star([21])) with a Venus-like atmosphere (Lebonnois et al., 2015) (Figure B.14 in Turbet et al. (2016)). The high contrast values of the reflection phase curves highlight the importance of studying planetary atmospheres with sulphuric acid aerosols. These aerosols are responsible for a high albedo in the visible wavelengths, strengthening the case for studying Venus-like atmospheres in the future. Adding cloud formation and evolution will enhance the prospects for characterising the atmospheric dynamics.

The order of magnitude of the contrast confirms the possibility of detection by the JWST and the *European Extremely Large Telescope* (E-ELT), whose instruments are planned to obtain contrasts on the order of 10^{-7} - 10^{-8}. However, TRAPPIST-1 c is a close-in planet orbiting TRAPPIST-1, located at $\sim$ 12.4 pc from the Earth. The combination of a minor semi-major axis and a considerable distance from the system to Earth leads to a maximum angular separation between TRAPPIST-1 c and TRAPPIST-1 of

---

[20] In fact, for an inclination of 90° the planet is not observed from the Earth as it goes under secondary eclipse.

[21] Proxima Centauri b is an M-dwarf star, but it is brighter than TRAPPIST-1 - which is a late-type M-dwarf star.

just 1.27 mas(22) at orbital phase $\pm\pi/2$. Such small angular separation makes detection under current instrumentation on 10-m class telescopes (e.g., GPI/Gemini(23) or SPHERE/VLT(24)) extremely unlikely (as explained by Turbet et al. (2016) for the case of Proxima Centauri b).

The planet-to-star contrast as a function of wavelength is presented in Figure 3.14 for different orbital phases in the wavelength range between 0.27 μm and 5.1 μm and inclination 90°. Overall, there is a larger contrast in the shorter wavelengths, in agreement with the phase curves in Figure 3.13. The spectra have two dips, at 2.8 μm and 4.3 μm, caused by the corresponding carbon dioxide absorption bands. The contrast values in the vicinity of these wavelengths will depend on the orbital phase. It has lower values for the negative orbital phases (compared to the corresponding positive orbital phase: e.g., $-3\pi/4$ versus $3\pi/4$). This result suggests a slightly more carbon dioxide absorption at the negative orbital phases.

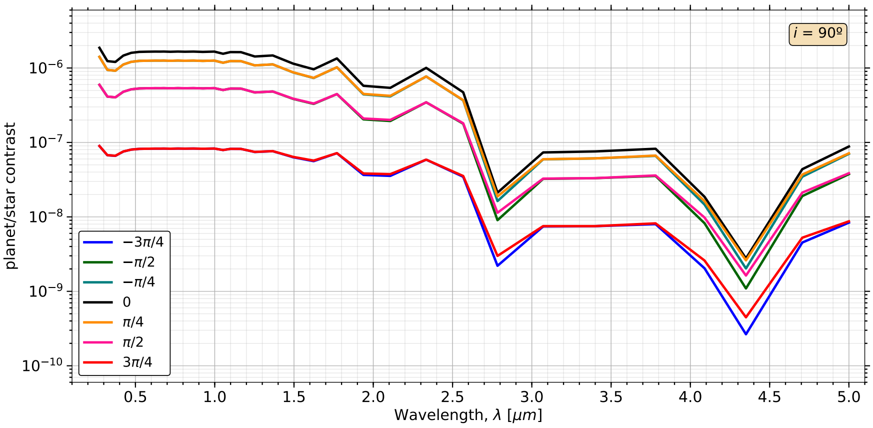

Figure 3.14: Planet-to-star contrast as a function of wavelength in μm (range: 0.27 - 5.1 μm) for the reference simulation of TRAPPIST-1 c with a Venus-like atmosphere. The reflection spectra are presented for seven orbital phases from $-3\pi/4$ to $3\pi/4$, for a 90° inclination and averaged throughout ten orbits. The orbital phase order depicts the planet's progression on its orbit around TRAPPIST-1, with the orbital phase 0 corresponding to the secondary eclipse. On the other hand, the orbital phase $-\pi$ or π (not represented in the figure) corresponds to the planetary transit. At this orbital phase, the received planet's reflected light is zero. Furthermore, since the reflection spectra are computed for an inclination of 90°, the orbital phase 0 depict the maximum theoretical contrast an observer can see.

The emission phase curves in the MIR (mid-IR) are presented in Figure 3.15 for the same inclinations: 90°, 60°, and 30°, and for nine spectral bands. Of particular interest in Figure 3.15 is the comparison between the *continuum* (i.e., spectral bands outside the strong absorption carbon dioxide bands) and regions inside the carbon dioxide absorption bands. The 4.3 μm and 15.0 μm carbon dioxide absorption bands (see Figure 3.16) have a strong impact in some of the selected thermal phase curves, respectively: 4.08 - 4.45 μm (solid blue line in Figure 3.15) and 14.99 - 16.21 μm (solid red line in Figure 3.15). Compared to the *continuum*, these spectral bands' thermal phase curves have larger amplitudes and later orbital phase for peak emission.

The emission phase curves allow for an exploration of the large-scale atmospheric dynamics, as the peak emission of all phase curves does not occur at the orbital phase 0 (as one would expect of a planet without a significant atmosphere) but earlier in the planet's orbit, between orbital phases $-\pi/2$ and 0. Therefore, the maximum emission occurs *east* of the substellar point: at a sub-observer longitude between the substellar point and the evening terminator. The eastward shift in peak emission suggests the advection of warm air masses from the substellar point towards the evening terminator, likely caused by the equatorial zonal superrotation jet. However, since there are at least two distinct orbital phases for

---

[22] 1 mas or 1 milliarcsecond is equivalent to $\sim 4.848 \cdot 10^{-9}$ radians.

[23] GPI - Gemini Planet Imager.

[24] Spectro-Polarimetric High-contrast Exoplanet REsearch instrument - Very Large Telescope.

peak emission, I decided to explore possible physical mechanisms supporting the two different eastward shifts in peak emission.

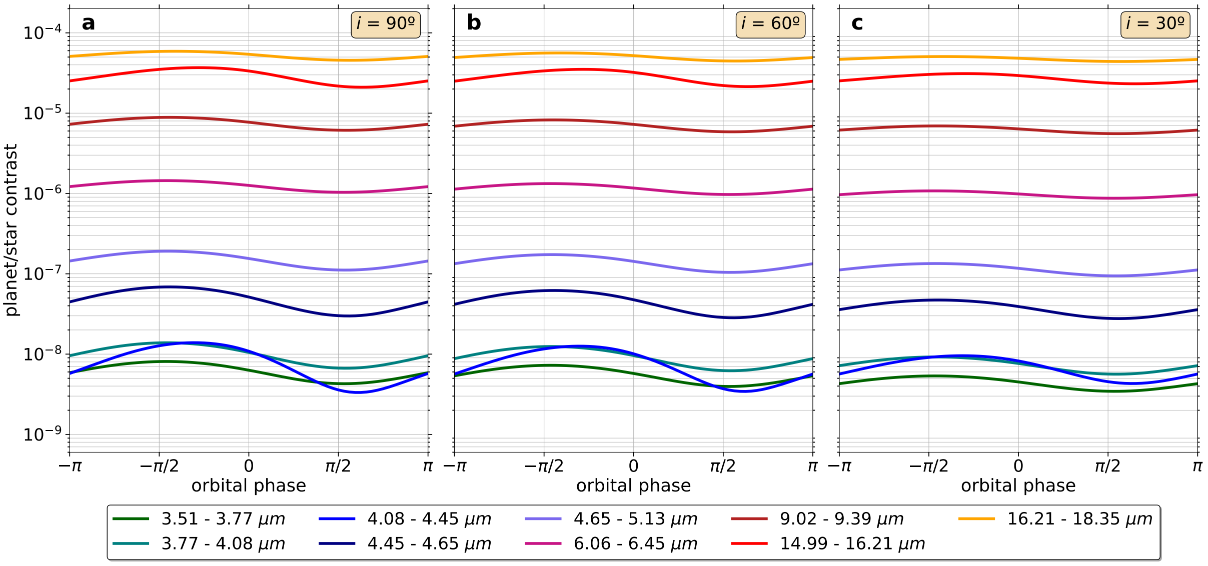

Figure 3.15: Emission phase curves (MIR) in planet-to-star contrast as a function of orbital phase for the reference simulation of TRAPPIST-1 c with a Venus-like atmosphere. The data is averaged over ten orbits, for three different inclinations (*i*): **(a)** 90°; **(b)** 60°; and **(c)** 30°. Nine different spectral bands are represented in each subplot.

The emission spectra of TRAPPIST-1 c are presented in Figure 3.16 in planet-to-star contrast as a function of wavelength for an inclination of 90°. The contrast increases for longer wavelengths as the planetary emission increases. In the longer wavelengths ($\lambda \gtrsim 22\ \mu m$), the contrast is $\mathcal{O}\left(10^{-4}\right)$, two orders of magnitude higher than the largest contrast values in the reflected wavelengths (see Figure 3.14). Two strong 4.3 μm and 15 μm carbon dioxide absorption bands contribute to a decrease in emission spectra's contrast. In these regions, the magnitude of contrast's decrease depends on the orbital phase (e.g., 14.99 - 16.21 μm, the red spectral band in Figure 3.17), leading to a larger spread of the emission spectra in opposition to the *continuum* (e.g., 11.43 - 12.50 μm in Figure 3.17).

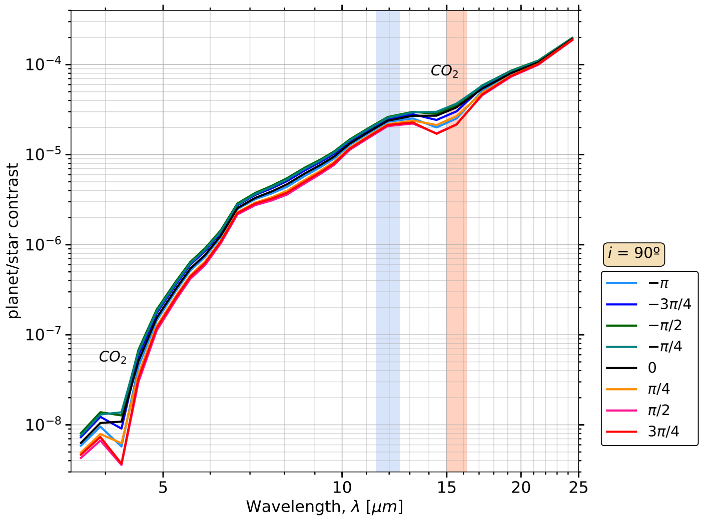

Figure 3.16: Emission spectra as a function of wavelength (range: 3.51 - 24.39 μm) computed at eight orbital phases for TRAPPIST-1 c (averaged throughout ten orbits) with a Venus-like atmosphere and an inclination i of 90º. The background colours represent spectral bands 11.43 - 12.50 μm (blue) and 14.99 - 16.21 μm (red).

To analyse the thermal phase curves amplitude and peak emission's orbital phase, I compare two phase curves: the 11.43 - 12.50 μm and 14.99 - 16.21 μm, and their respective OLR maps in Figure 3.17.

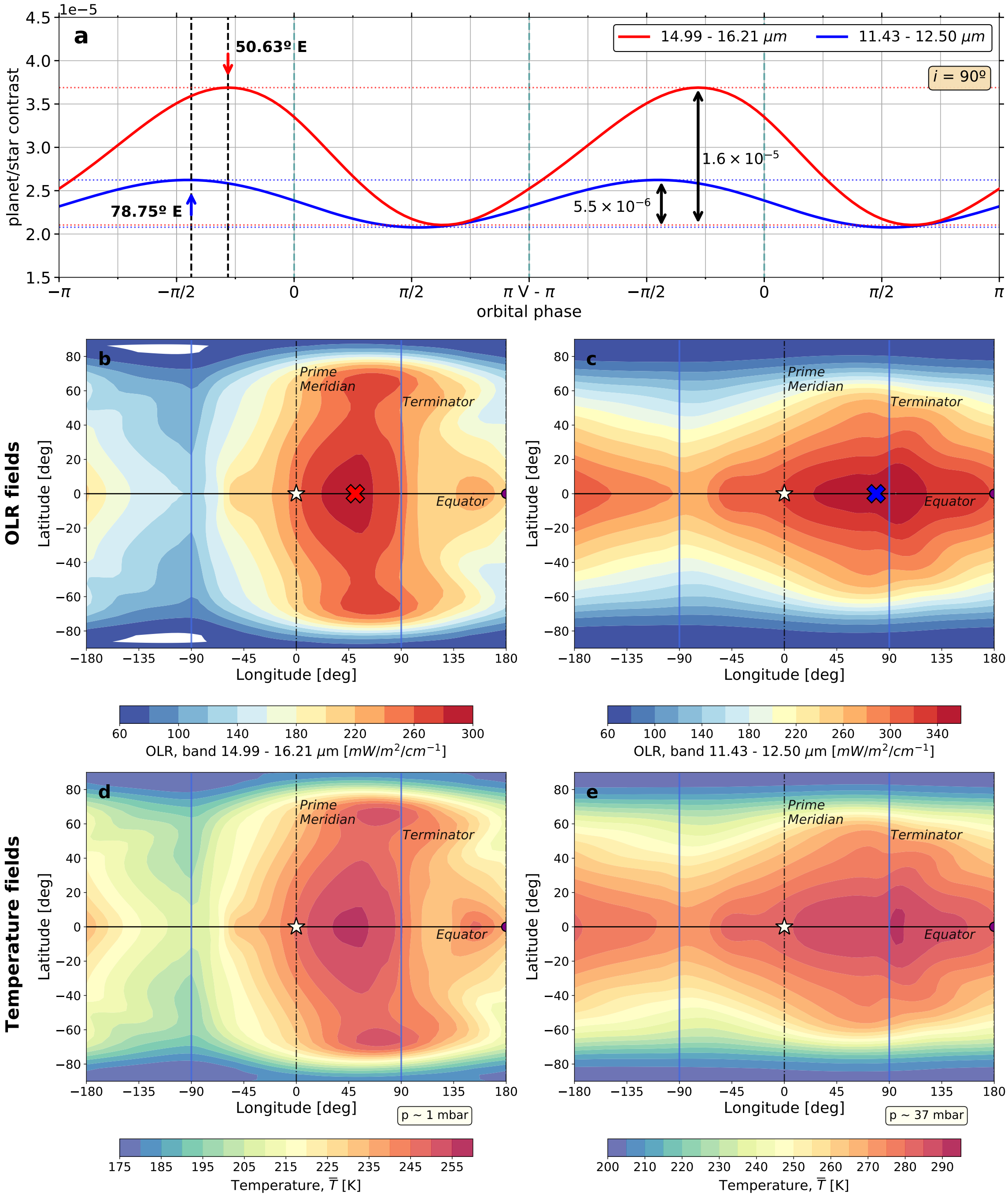

Figure 3.17: Relation between thermal phase curves, OLR and temperature fields and remote sensing of different TRAPPIST-1 c atmospheric levels. The two emission phase curves in panel **(a)** planet-to-star contrast as a function of the orbital phase, for an inclination i of 90° are the: (i) 14.99-16.21 μm (solid red line); and (ii) 11.43-12.50 μm (solid blue line). The coloured arrows identify each phase curve peak emission's orbital phase and corresponding longitude, while the two head black arrows point out the amplitude of each phase curve. The green vertical dashed lines mark the orbital phases 0 and $-\pi$. Panels **(b)** and **(c)** represent the time-mean OLR fields in $mW/m^2/cm^{-1}$ (latitude vs. longitude) for the 14.99-16.21 μm and 11.43-12.50 μm spectral bands, respectively. The red/blue cross pinpoint the longitudinal location of the maximum peak emission over the equator. Panels **(d)** and **(e)** represent the time-mean temperature fields at two different pressure levels: 1 $mbar$ and 37 $mbar$, respectively. A white star (purple dot) identifies the substellar (antistellar) point. A solid (dashed) black line represents the equator (prime meridian), while the terminators are in solid blue lines. Data in all panels are time-averaged for ten orbits of TRAPPIST-1 c.

The emission phase curves represent the longitudinal integration of the OLR field. Thus, the phase curve amplitude and peak emission's orbital phase suggest the structure of the base OLR field. Conversely, the OLR field provides information on the temperature field, as the latter is a first approximation of the former. In Figure 3.17, the two different OLR fields closely match temperature fields at different atmospheric levels. The relation between thermal phase curves, OLR and temperature fields is as follows:

- The OLR 14.99-16.21 μm spectral band, inside the 15 μm carbon dioxide absorption band:
    - The OLR field shows an almost *hemispheric dichotomy* (Figure 3.17 **(b)**): the largest ($> 200\ mW/m^2/cm^{-1}$) emission values are located between longitudes $\sim 45°$ W and $\sim 180°$ E;
    - Strong modulation of the thermal phase curve: the OLR field *strongly* dependence with longitude leads to a *large* amplitude of the thermal phase curve ($1.6 \cdot 10^{-5}$) (red curve in Figure 3.17 **(a)**);
    - *Later* orbital phase for peak emission: the eastward shift of the OLR maximum occurs *closer* to the substellar point (50.63° E) (red cross in Figure 3.17 **(b)**);
    - Remote sensing of mesospheric dynamics: the closest temperature field match to the 14.99-16.21 μm OLR field occurs for $\sim 1\ mbar$ (Figure 3.17 **(d)**), i.e., where carbon dioxide absorption is the strongest.
- The OLR 11.43-12.50 μm spectral band, in the *continuum*, thus outside the 15 μm carbon dioxide absorption band:
    - The OLR field shows a **chevron-like pattern**, centred at the substellar point region (Figure 3.17 **(c)**), with lower longitudinal OLR variation than the 14.99-16.21 μm OLR field;
    - Weak modulation of the thermal phase curve: the lower longitudinal OLR variation lead to a smaller amplitude of the thermal phase curve ($5.5 \cdot 10^{-6}$) (blue curve in Figure 3.17 **(a)**);
    - *Earlier* orbital phase for peak emission: the eastward shift of the OLR maximum occurs *farther* from the substellar point (78.75° E) (blue cross in Figure 3.17 **(c)**);
    - Remote sensing of cloud top dynamics: the closest temperature field match to the 11.43-12.50 μm OLR field occurs for $\sim 37\ mbar$ (Figure 3.17 **(e)**), i.e., the global cloud top level.

The conclusions drawn for the selected thermal phase curves (14.99-16.21 μm and 11.43-12.50 μm spectral bands) can be applied to other spectral bands. Overall, the carbon dioxide absorption bands and the *continuum* allow to sound different atmospheric levels in TRAPPIST-1 c:

- **Mesospheric, above the cloud deck altitudes**: the 15 μm carbon dioxide absorption occurs high in the atmosphere, warming the region in the vicinity of $\sim 1\ mbar$. Most OLR emission occurs between the substellar point and evening terminator longitudes, with the hotspot located almost halfway between these two longitudes. As a result, the thermal phase curve peak emission occurs later in the orbit (the hotspot offset is closer to the substellar point), and its large amplitude reflects the substantial longitudinal variations of the OLR field and the **localised** carbon dioxide absorption. The considerations drawn are valid for 4.3 μm carbon dioxide absorption band.
- **Cloud top altitudes**: in the *continuum*, the OLR field shows a **chevron-like pattern**, similar to the one in the cloud top temperature field at $\sim 37\ mbar$ (see Figure 3.7). The hotspot is close to the evening terminator, suggesting a physical mechanism responsible for the advection of warm air masses from the substellar point to the evening terminator. From the analysis of the cloud top temperature and zonal wind fields, the hotspot's eastward offset is caused by the presence of an equatorial zonal superrotation jet (see Figure 3.9).

However, the OLR longitudinal disk-integration method of the phase curve limits the interpretation of certain features of the OLR fields. As an example, the 14.99-16.21 μm OLR field has two high-latitude maxima ($\sim 270\ mW/m^2/cm^{-1}$) centred at $\sim 60°$ N/S and $\sim 60°$ E. The largest ($\sim 290\ mW/m^2/cm^{-1}$) emission occurs at the equator at a similar longitude $\sim 50°$ E. The independent detection of these maxima is very unlikely, given that they share similar longitudes. I conclude that thermal phase curves will not distinguish different maxima located at similar longitudes.

Another limitation to the thermal phase curve interpretation is the $\sim 45°$ W local maximum in the 11.43-12.50 μm OLR field. The emission at $\sim 45°$ W closely resembles the hotspot in the temperature field associated with adiabatic warming (see Figure 3.7 and text). Despite being visible in the OLR and temperature field, the hotspot is not strong enough compared to the peak emission (blue cross in Figure 3.17 **c**) occurring close to the evening terminator ($\sim 80°$ E). However, if a stronger downdraft-driven adiabatic warming were present, the 45° W hotspot could have become more intense, making detection in the thermal phase curve more likely. In conclusion, the most intense longitudinal OLR patterns (e.g., chevron-like pattern) dominate the thermal phase curve interpretation.

The thermal phase curve's amplitude and peak emission evaluation, in particular comparing the phase shift between the two emission phase curves with the corresponding OLR and temperature fields, constrains the hotspot location and suggests different physical processes and dynamics are happening at two different atmospheric levels. The consequent interpretation of the large-scale circulation from thermal phase curve data is possible due to GCM outputs (e.g., temperature and wind maps). Observing the thermal phase curves' amplitude modulation can potentially be achieved with JWST.

Transmission spectra The simulated transmission spectra of TRAPPIST-1 c for JWST `NIRSpec Prism` and `MIRI` (with a resolving power of 1000) are presented in Figure 3.18 for Venus-like clouds and clear-sky conditions. Both transmission spectra in Figure 3.18 are presented in estimated effective height (transit atmospheric thickness) in km and in planet-to-star contrast (radiance ratio with respect to target parent star) in ppm. The effective height or $h(\lambda)$ is defined as the altitude threshold below which the atmosphere can be considered to be opaque, effectively blocking the background starlight (Kaltenegger and Traub, 2009). The wavelength range in Figure 3.18 (from 0.6 μm to 20 μm) nearly covers that of JWST.

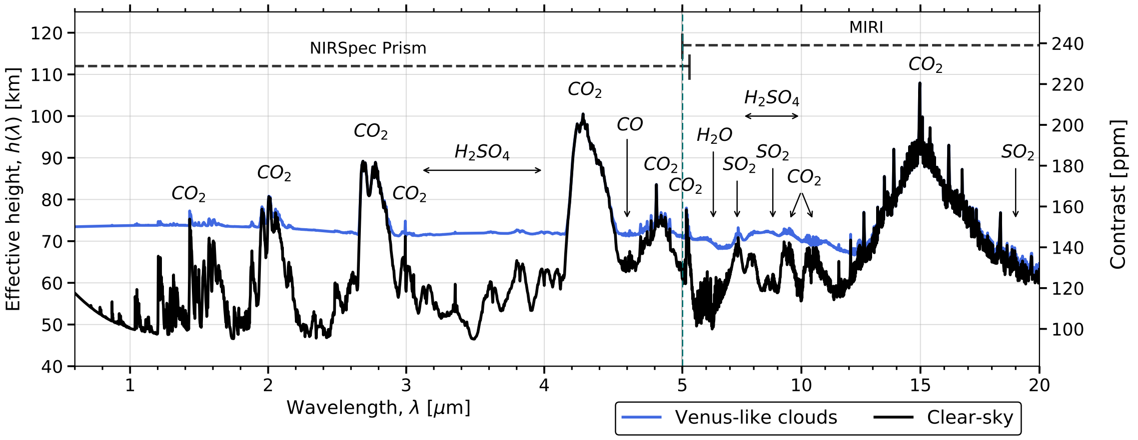

Figure 3.18: Simulated transit transmission spectra of TRAPPIST-1 c for JWST's `NIRSpec Prism` (0.6 - 5.3 μm in the figure) and `MIRI` (5.0 - 20.0 μm in the figure) with a resolving power $R_p = 1000$ for two cases: **(a)** Venus-like clouds (solid blue line) and **(b)** clear-sky conditions (solid black line). The transmission spectra are simulated with the `Planetary Spectrum Generator` (Villanueva et al., 2018) and are presented in effective height $h(\lambda)$ (transit atmospheric thickness) in km and relative transit depth in ppm as a function of wavelength λ in μm. Note the two different linear scales in the wavelength x-axis (separated by the dashed vertical green line). The main Venus-like clouds spectral features are identified in the figure.

The two TRAPPIST-1 c transmission spectra, with Venus-like clouds and clear-sky conditions, show strong carbon dioxide absorption spectral features centred at 2.0, 2.8, 4.3 and 15 μm. Both spectra show weaker CO_2 spectral bands and features from other chemical species such as water vapour, sulphur dioxide, and carbon monoxide. In the case of Venus-like clouds, the sulphuric acid aerosols lead to a flattening and rising of the *continuum* level (Figure 3.18, solid blue line). Table 3.2 introduces the main transmission spectral features for the two TRAPPIST-1 c transmission spectra.

Table 3.2: TRAPPIST-1 c transmission spectral features

Transmission Spectra	**Chemical species**	**Wavelengths in μm**
Case: Venus-like clouds	CO_2	1.5, 2.0, 2.8, 3.0, 4.3, 4.8, 5.2, 7.3, 9.5, 10.5, 15.0
	H_2O	6.3
	SO_2	7.3, 8.8, 19.0
	CO	4.6
	H_2SO_4	3.1-4.0, 7.5-10
Case: Venus-like clear-sky	CO_2	1.05, 1.2, 1.3, 1.5, 1.6, 2.0, 2.8, 3.0, 3.2, 3.4, 3.6, 3.8, 4.0, 4.3, 4.8, 5.2, 7.3, 7.9, 9.5, 10.5, 15.0
	H_2O	1.4, 1.8, 2.6, 6.3
	SO_2	4.0, 7.3, 8.8, 19.0
	CO	2.35, 4.6

As expected in the clear-sky case, absorption features are deeper, particularly the CO_2 features. In the cloudy case's short wavelengths (< 4 μm), the effective height is $\sim$ 74 km, corresponding to the high altitude haze above the cloud deck, simulated with the Generic-GCM. For longer wavelengths (> 4 μm), the effective height for the *continuum* decreases ($\sim$ 69 km at 7 μm). Thus, longward of 4 μm, identifying chemical species like water vapour, carbon monoxide, and sulphur dioxide might become possible, although still challenging given the shallow effective height of these spectral features. The relative depth in ppm and effective height in km of some spectral bands are shown in Table 3.3.

Table 3.3: Relative transit depth (ppm) and effective height (km) of spectral lines of TRAPPIST-1 c simulated with a Venus-like atmosphere

Spectral feature	**Venus-like clouds**		**Clear-sky conditions**	
	Depth [ppm]	Thickness [km]	Depth [ppm]	Thickness [km]
CO_2, 2.0 μm	14	7	60	29
CO_2, 2.8 μm	36	18	63	31
CO_2, 4.3 μm	57	28	74	38
CO_2, 4.8 μm	17	8	31	15
SO_2, 7.3 μm	3	5	4	9
CO_2, 15 μm	84	41	104	50

Lincowski et al. (2018) who compared atmospheres with different carbon dioxide abundances, describe that these strongest carbon dioxide spectral features are present in transmission spectra whether carbon dioxide is a main atmospheric component or a trace gas. Therefore, the strongest CO_2 bands can only be indicators of a *terrestrial* planetary atmosphere: they are not an effective observational discriminant for a Venus-like atmosphere or Climate (Venus-like versus Earth-like or other). However, the same authors point out that additional weaker CO_2 spectral features in the transmission spectra suggest a high abundant carbon dioxide atmosphere closer to Venus values. In the TRAPPIST-1 c transmission spectra, it is possible to observe several CO_2 weaker features. Additionally, we interpret the presence of the weaker 4.8 μm CO_2 band as a consequence of the pressure broadening effect on the spectral bands - an expected result given the high-pressure atmosphere.

Other spectral features like sulphur dioxide and sulphuric acid aerosols might help discriminate a Venus-like atmosphere. For example, the 7.3 μm sulphur dioxide absorption is visible in both TRAPPIST-1 c transmission spectra. Nonetheless, the relative effective height of this spectral band is relatively shallow (see Table 3.3), which will make its detection difficult. Furthermore, the impact of sulphuric acid aerosols is noticeable from 3.1 μm to 4.0 μm, leading to a flattening of the transmission spectrum (blue curve in Figure 3.18), which could help to identify cloudy, Venus-like atmospheres. However, Lincowski et al. (2018) further adds that sulphuric acid clouds formation also occurs in outgassing, oxygen-dominated atmospheres, which limits the conclusions on the kind of Climate. Given these arguments, the possible detection of weaker CO_2 spectral bands, particularly the 4.8 μm, seems to be a promising method for identifying a high-pressure Venus-like atmosphere.

The minor components included in the simulated Venus-like atmosphere: carbon monoxide, carbonyl sulfide, sulphur dioxide, and water vapour, have larger mixing ratios at and below the global cloud deck (see Figure 2.1). Consequently, their respective spectral features tend to be screened by the *continuum* level imposed by the sulphuric acid aerosols and atmospheric refraction for the case of the Venus-like clouds. Minor components are not as well-mixed as carbon dioxide (whose abundance is constant throughout the entire atmospheric column), and their concentrations above the cloud tops are very low for them to produce strong spectral features that can be detected through transmission spectroscopy. Accordingly, their detection is more challenging than the carbon dioxide spectral lines, with larger relative effective height and contrast values. Furthermore, even in the case of clear-sky conditions, detection of minor components' spectral features is challenging, as suggested from Figure 3.18.

Overall, the simulation of TRAPPIST-1 c with Venus-like clouds leads to elevated *continuum* levels that tend to suppress or challenge the detection of spectral features from atmospheric constituents whose concentrations are non-significant above the cloud opacity level. For example, since carbon dioxide is a well-mixed gas throughout the atmospheric column (i.e., enough gas will remain above the cloud deck and the upper haze), detection of carbon dioxide's spectral lines might be likely, in particular, the strongest 4.3 and 15 μm carbon dioxide absorption features. However, even the relative transit depth of these strong CO_2 spectral lines will be reduced by the high *continuum* level raised by Venus-like aerosols.

Following our synthetic transmission spectra, detecting such an atmosphere is within reach of JWST capabilities. However, simulated noise for observations with JWST instruments is required to understand the number of transits needed to detect spectral features. Lustig-Yaeger et al. (2019a) calculated the number of TRAPPIST-1 c transits necessary to detect the strongest CO_2 features in a Venus-like atmosphere by simulating noise in `NIRSpec Prism` observations. Overall, the authors concluded that Venus-like aerosols require five times more transits to detect the same spectral features as clear-sky conditions. The need for a larger number of transits bring out the challenges of characterising a cloudy, Venus-like atmosphere to the same level of detail as the one done under clear-sky conditions. Furthermore, it imposes longer observational campaigns to detect shallower bands, which might not be feasible due to limited telescope time. Nonetheless, the modelling studies by Lustig-Yaeger et al. (2019a) point out that identification of CO_2 absorption features by future JWST transmission spectroscopy is possible given that this gas is well-mixed throughout the atmospheric column.

A dedicated photochemical cloud model, sensitive to M-dwarf conditions, coupled with the Generic-GCM, should be implemented in future studies. This model would help recreate Venus-like atmospheric sulphur photochemistry by simulating sulphuric acid cloud formation. In addition, the studies should explore how these reactions impact the relative abundances of chemical species such as water vapour and sulphur dioxide throughout the atmospheric column (in particular at the uppermost levels where transmission spectroscopy will be able to probe them, in the event clouds or hazes are being considered) and, consequently, their respective spectral bands in the transmission spectra. Moreover, a self-consistent cloud model dependent on temperature could modify the effective height of the transmission spectra and the conditions where deeper spectral features can become visible should also be explored.

3.3 3D Climate modelling of TRAPPIST-1 c under clear-sky conditions

The removal of Venus-like clouds has a significant impact on the thermal structure of TRAPPIST-1 c's deep atmosphere (i.e., $p \geq 1\ bar$), with an increase of surface temperature by 160 K (the red curve in Figure 3.19). The shape of the clear-sky adiabat is closer to the one seen for Venus, represented here by the VIRA model (the black curve in Figure 3.19).

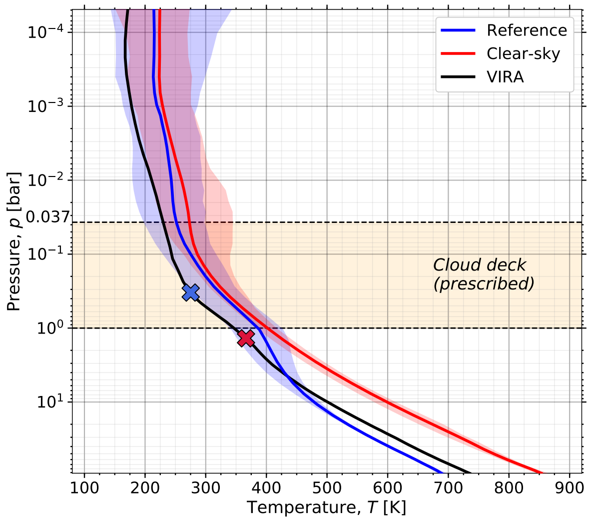

Figure 3.19: The global time-mean temperature profiles for the reference simulation of TRAPPIST-1 c with Venus-like clouds (solid blue line) and the clear-sky simulation (solid red line). The VIRA profile model is depicted by a solid black line. The shaded areas represent the temperature value range (the maximum and minimum value amongst all latitudes) per pressure level for the reference and clear-sky profiles. The red (blue) cross over the VIRA profile indicates the approximate pressure level of the condensation (freezing) point of sulphuric acid on Venus. Additionally, two dashed black lines limit the prescribed global cloud deck (pale orange background) between cloud base (1 bar) and top (0.037 bar).

The zonal and time-averaged temperature maps in Figure 3.20 show a distinct thermal structure between the TRAPPIST-1 c's Venus-like clouds and clear-sky simulations. As shown by the temperature profile in Figure 3.19, the surface temperature in the clear-sky case is substantially elevated by 160 K (from $\sim$ 690 K to $\sim$ 850 K). The isothermals in the reference simulation (Figure 3.20 (a)) show a large equator-pole temperature gradient for altitudes above $\sim$ 10 bar, which becomes more intense in the uppermost layers of the atmosphere. Consequently, the polar regions are much colder than the latitudes lower than $\sim$ 60° N/S. Above the cloud deck and for latitudes above $\sim$ 80 ° N/S, the polar atmosphere is colder than 200 K.

In the clear-sky simulation, the equator-pole temperature gradient is only significant between $\sim 100\ mbar$ and $\sim 1\ mbar$. However, in contrast with the Venus-like clouds simulation, the polar regions are warmer than the lower latitudes. The **polar warming** feature (see the isothermal 300 K in Figure 3.20 **(b)**) is seen in both hemispheres for latitudes higher than $\sim 70°$ N/S. Overall, the clear-sky TRAPPIST-1 c atmosphere is warmer than in the case of the Venus-like clouds.

I have also explored the differences between dayside and nightside temperatures (not shown), which in the case of Venus-like clouds, are similar to the globally averaged temperature shown in Figure 3.20. For the clear-sky conditions, outside the polar regions, the dayside upper atmosphere (above $\sim 10\ mbar$) is approximately 50 K warmer than the nightside. The polar warming feature is preserved both in the dayside and nightside hemispheres.

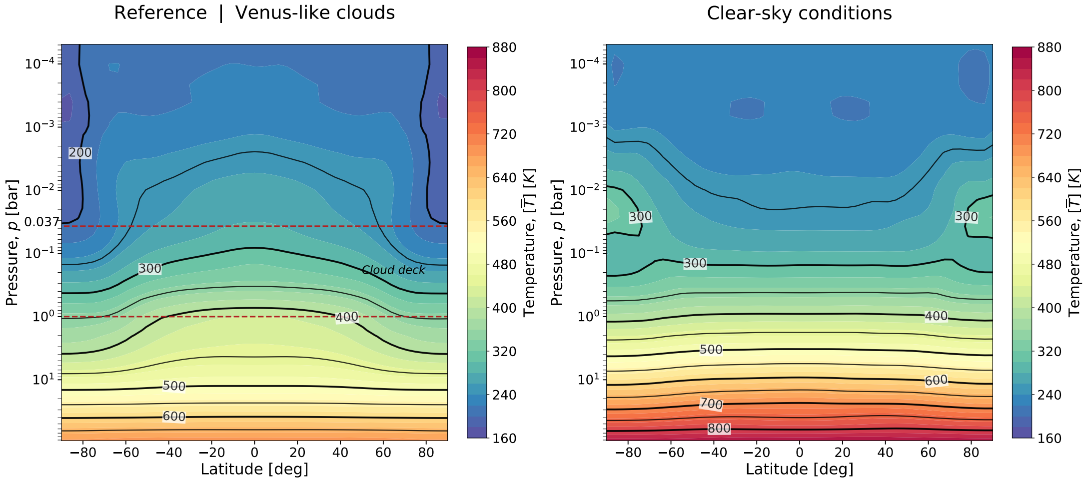

Figure 3.20: Zonal and time-averaged temperature fields in K for the reference Venus-like clouds **(a)**, and clear-sky conditions **(b)**, averaged over ten orbits of TRAPPIST-1 c. Isothermals are represented with a step of 100 K (thick solid black lines) or 50 K (thin solid black lines).

The zonal wind fields are substantially distinct between the two simulations as shown in Figure 3.21 suggesting a different global circulation. In contrast to the Venus-like clouds simulation, which is dominated by a zonal superrotation equatorial and high-latitudes eastward jets (see Figure 3.21 **(a)**), the clear-sky simulation reveals two mid-latitudes *westward* jets centred at $\sim 40°$ N/S and above $\sim 10\ mbar$ with speeds larger than - 100 $m\,s^{-1}$. These mid-latitudes westward jets flank a less intense ($\sim 75\ m\,s^{-1}$) equatorial *eastward* jet (see Figure 3.21 **(b)**). Unlike the Venus-like clouds simulation, the mid-latitudes westward jets do not extend as deep in the atmosphere, halting their motion at $\sim 10\ mbar$. Below this pressure level, there are high-latitudes *eastward* jets whose cores are located at higher latitudes ($\sim 60°$ N/S) and are less intense ($\sim 75\ m\,s^{-1}$) than the higher altitude westward jets.

The time-mean zonal wind fields at 0.037 bar (Figure 3.21 **(c, d)**), cloud top altitude for the Venus-like clouds simulation) show a westward equatorial jet east of $\sim 45°$ W in the clear-sky simulation. This jet is stronger in the substellar region, reaching maximum speeds of $-60\ m\,s^{-1}$. In opposition, in the morning terminator region, there is an eastward jet, reaching speeds as large as 80 $m\,s^{-1}$. The zonal wind field is completely different from the Venus-like clouds simulation, where the zonal wind at the equator is always eastward (see Figure 3.21 **(e)**). Moreover, in the clear-sky simulation (Figure 3.21 **(f)**), the equatorial zonal wind flow is westward in the dayside region, reaching $-200\ m\,s^{-1}$ in the uppermost layers of the atmosphere. Despite being dominant on the nightside, the speeds of the eastward equatorial flow are lower in the clear-sky simulation compared to the Venus-like clouds simulation. The vertical wind field (shown by the black arrows in the panels **(e, f)**) is also substantially different in the clear-sky simulation, with a stronger upwelling, namely on the dayside and west of the substellar point.

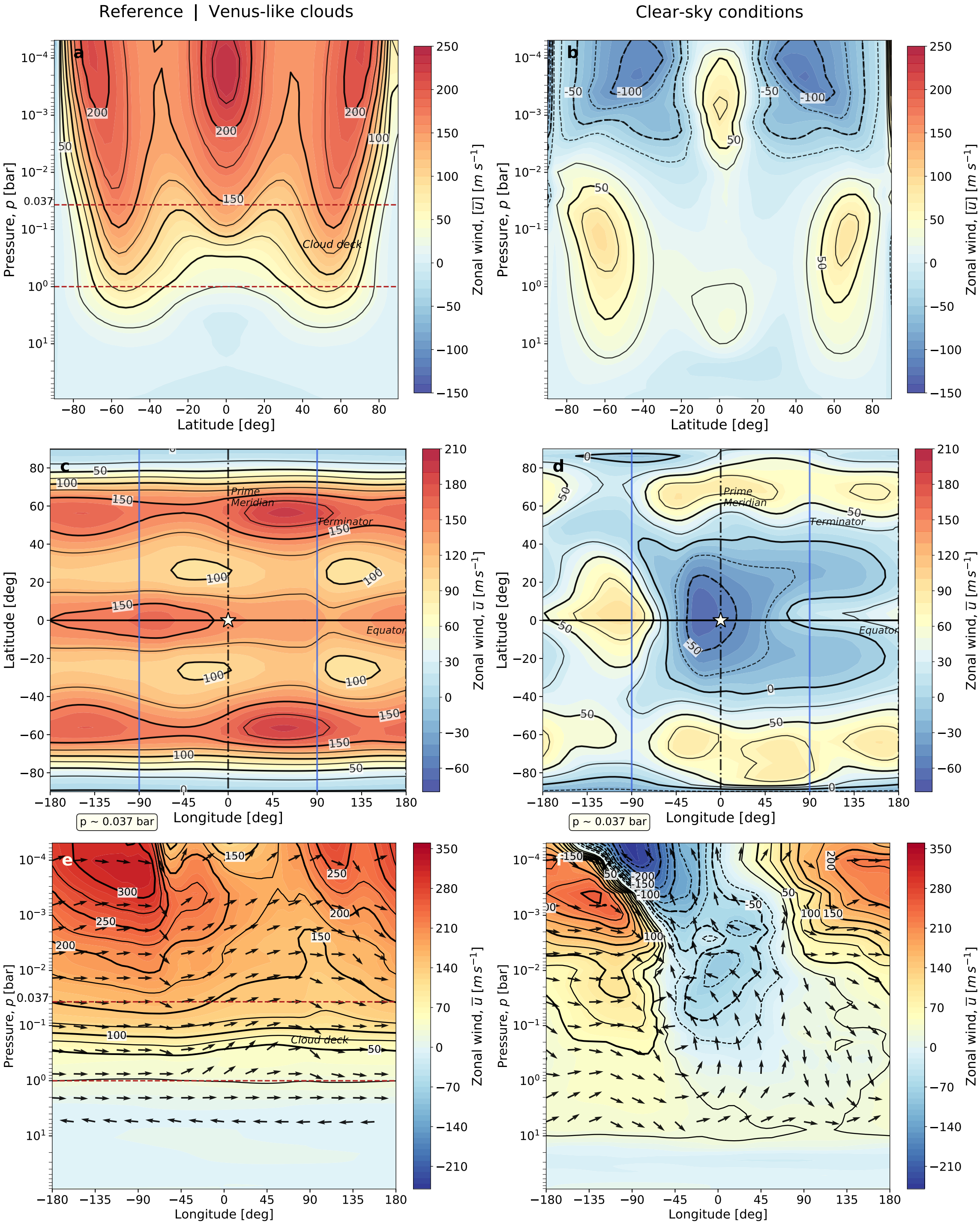

Figure 3.21: Three different perspectives over the zonal wind field on the reference simulation with Venus-like clouds of TRAPPIST-1 c **(a, c, e)** and the clear-sky simulation **(b, d, f)**. The top panels **(a, b)** represent the pressure versus latitude zonal and time-averaged zonal wind field, $[\overline{u}]$ in $m\,s^{-1}$. The mid-panels **(c, d)**, the latitude versus longitude time-mean zonal wind field, $\overline{u}$ in $m\,s^{-1}$ at p $\sim$ 0.037-bar (cloud tops in the Venus-like clouds simulation). The substellar point is depicted as a white star, while the terminators, equator and prime meridian are represented by solid blue, solid black and dashed black lines, respectively. The bottom panels **(e, f)** represent the pressure versus longitude time-mean zonal wind field, $\overline{u}$ in $m\,s^{-1}$, at planet's equator. The normalised wind vectors are represented by black arrows (the vertical component is multiplied by the ratio between the horizontal and vertical spacings). For all panels, isotachs are depicted with a step of 25 $m\,s^{-1}$ (thin solid black lines) and 50 $m\,s^{-1}$ (thick solid black lines). The cloud deck extends from 1 bar to 0.037 bar (dashed red lines), depicted in the panels **(a, e)**.

Concerning the observables, the reflection planet-to-star contrast is significantly impacted by the clear-sky conditions (see Figure 3.22). The overall reflection phase curves contrast is reduced by several orders of magnitude (except for the spectral bands 0.25 - 0.30 μm and 0.75 - 0.78 μm where the decrease in contrast is smaller than one order of magnitude). As discussed in the case of Venus-like clouds, the reflection phase curves are useful for detecting inhomogeneities arising from cloud-related albedo variability. In the clear-sky simulation, the absence of clouds leads to a symmetry of the reflection phase curves around the orbital phase 0 (secondary eclipse), as commented above.

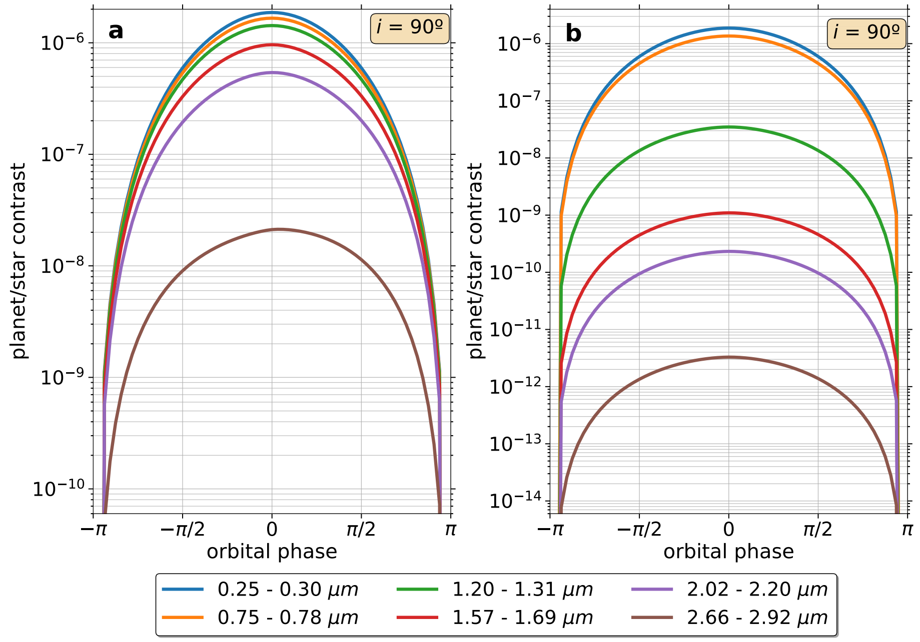

Figure 3.22: The reference, Venus-like clouds **(a)**, and clear-sky **(b)** reflection phase curves for TRAPPIST-1 c for an inclination i of 90° and for six spectral bands.

The emission phase curves are substantially impacted in the clear-sky conditions, with the peak emission of spectral bands centred around the 4.3 μm and 15 μm carbon dioxide absorption bands (blue and red phase curves in Figure 3.23, respectively) moving closer to the substellar region compared to the Venus-like clouds simulation (see Figure 3.23 **(a)**). All the other spectral bands tend to be flattened in clear-sky conditions.

At a first approach, comparing the results between the thermal phase curves of the two simulations can be done by looking at the OLR fields calculated for two different spectral bands in Figure 3.24: 14.99 - 16.21 μm and 9.02 - 9.39 μm (corresponding respectively to the red and brown phase curves in Figure 3.23). For the clear-sky conditions, the 14.99 - 16.21 μm spectral band's associated peak emission occurs in the vicinity of the substellar point. This is responsible for a small eastward shift seen in the thermal phase curve (Figure 3.23 **(b)**), compared to the one seen in the Venus-like clouds simulation for the same spectral band (Figure 3.23 **(a)**). Moreover, the OLR field day-night contrast is large enough to produce a large amplitude of this thermal phase curve compared to the *continuum* thermal spectral bands.

The much lower amplitude of the thermal phase curves for the *continuum* under clear-sky conditions is explored in the OLR map of Figure 3.24 **(d)**. Despite showing two polar maxima, the longitudinal variation of the OLR field for latitudes lower than 60° N/S is minimal. This small longitudinal variation of the OLR field might be responsible for a small amplitude of the thermal phase curves in the clear-sky scenario. In contrast, the Venus-like clouds simulation shows a larger longitudinal variation of the OLR field (see Figure 3.24 **(c)**), and a thermal emission peak located at approximately orbital phase $-\pi/2$, matching the maximum emission at 90° E in the respective OLR map. This eastward shift of thermal emission might be caused by the equatorial zonal superrotation jet as discussed in **section 3.2.6**.

The *continuum* thermal phase curves in the case of the clear-sky simulation do not show evidence for an eastward shift of peak emission. Together with the described zonal wind fields for the clear-sky simulation, this result suggests a different heat redistribution mechanism in the clear-sky simulation. Further analysis revealed that *continuum* spectral bands sound lower atmospheric levels ($\sim 101\ mbar$) in the clear-sky scenario compared to the Venus-like clouds simulation ($\sim 37\ mbar$).

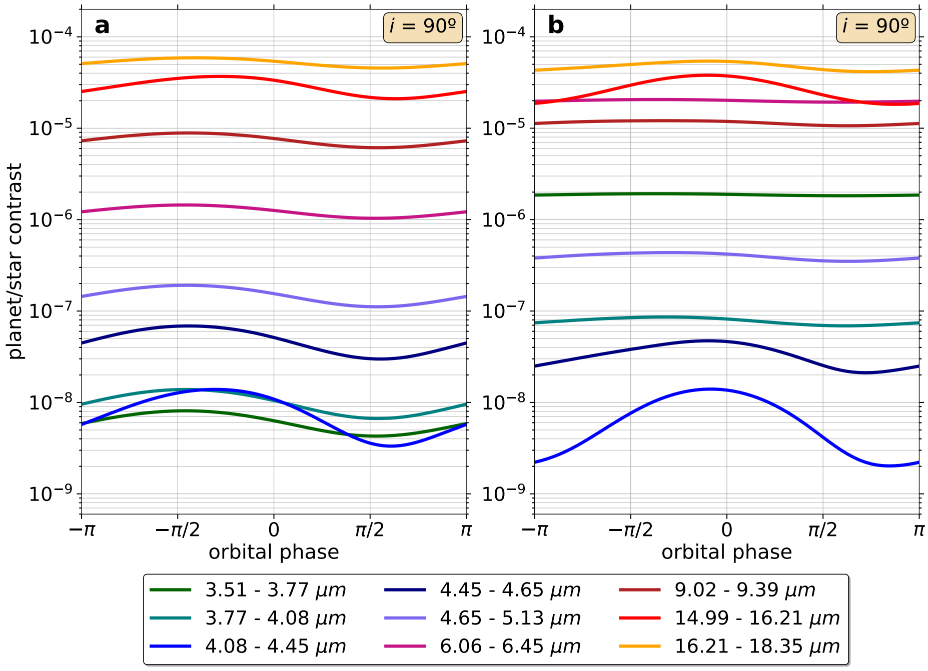

Figure 3.23: The Venus-like clouds **(a)** and clear-sky **(b)** thermal emission phase curves for TRAPPIST-1 c for an inclination i of 90° and for nine spectral bands.

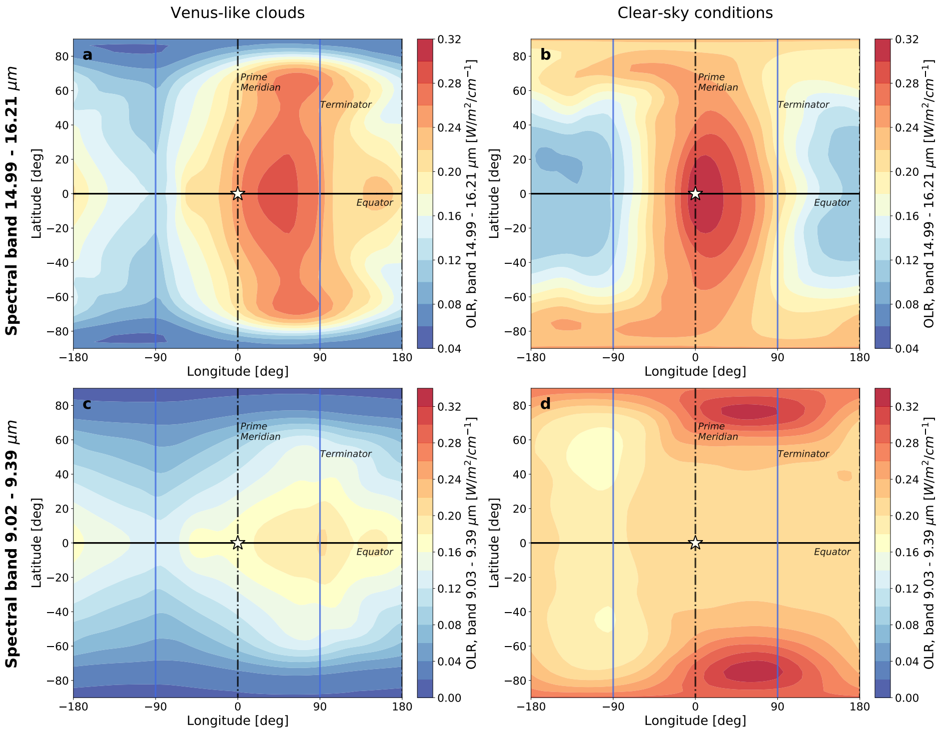

Figure 3.24: The OLR maps for the reference **(a, c)** and clear-sky simulations **(b, d)** of TRAPPIST-1 c for two spectral bands: 14.99 - 16.21 μm **(a, b)** (close to the 15 μm carbon dioxide absorption bands); and 9.02 - 9.39 μm **(c, d)** (to represent the *continuum*).

3.4 Parametric study of the Venus-like exoplanetary population

3.4.1 Mass-radius relationships

The cloud top temperature fields of the four studied cases of the 20% Fe mass-radius relationship reveal gradual warming for larger planetary radii. In all studied scenarios shown in Figure 3.25, the temperature maximum is located in the equator, in the vicinity of the evening terminator (90° E). The temperature maximum eastward shift seems to be slightly smaller for larger planetary radii. Moreover, as the planetary radii increases, the chevron-like pattern becomes more obvious and two temperature maxima appear in the high latitudes (at $\sim 60°$ N/S and $\sim 45°$ E), flanking the equatorial maximum (see panels **(c, d)** in Figure 3.25). In all simulations, there is a local maximum west of the substellar point (at $\sim 50°$ W), possibly related to local adiabatic warming, as discussed for the reference simulation of TRAPPIST-1 c (see **section 3.2.3.** and **section 3.2.4.**).

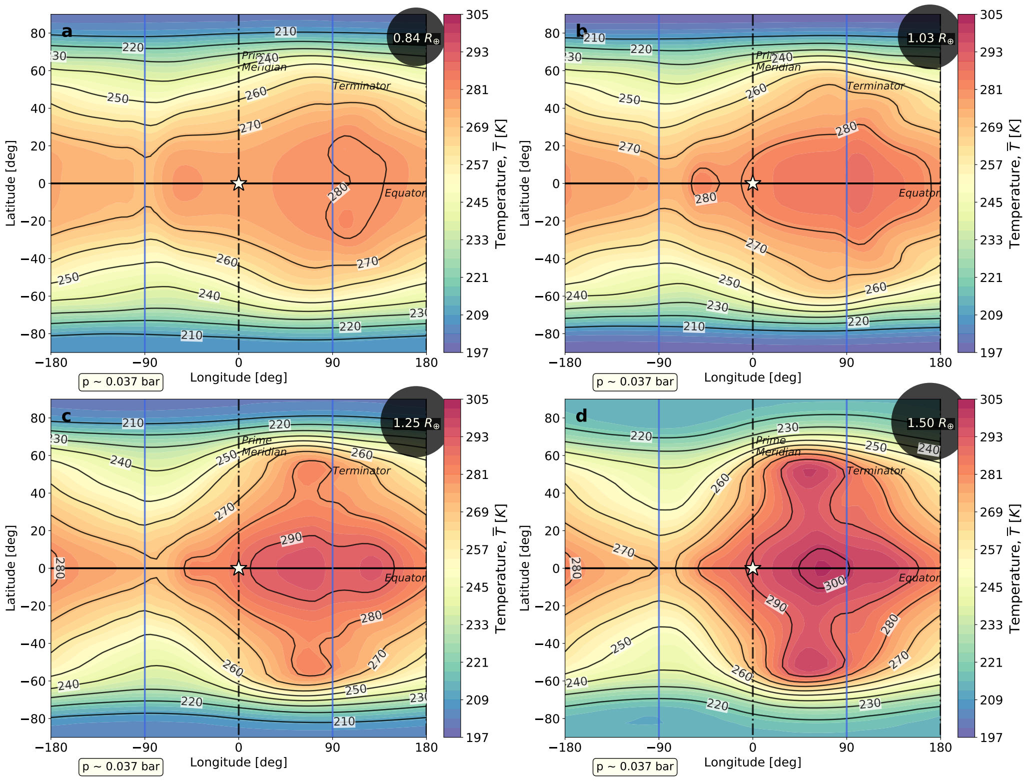

Figure 3.25: Time-averaged temperature fields in K in latitude versus longitude for the clouds tops at $p \sim 0.037\ bar$ for four different planets following the 20% Fe mass-radius relationship with the same instellation value as TRAPPIST-1 c. Data is averaged for 10 orbits. The isothermals are represented by solid black lines. The substellar point is marked with a white star. The terminators, equator and prime meridian are identified by the solid blue, solid black and dashed black lines, respectively. The planetary radius is displayed inside the black dot in the upper right corner, representing the relative size of each modelled planet.

The impact of the four studied cases in the zonal wind is visible in Figure 3.26. All simulations reveal the presence of three zonal jets in the zonal and time-averaged zonal wind field: an equatorial and two high-latitudes jets, similar to the reference simulation of TRAPPIST-1 c. The cores of these jets are centred at the equator and about 60° N/S, respectively. The jet cores are located in the upper atmosphere at pressure levels between 1 $mbar$ and 0.1 $mbar$. For smaller planetary radii (see panels **(a, b)**), all three jets have similar maximum speeds. However, for larger planetary radii (see panels **(c, d)**) the equatorial jet becomes more intense, reaching maximum speeds of $\sim 260\ m\,s^{-1}$ in the 1.25 $R_\oplus$ case (Figure 3.26

(c)). For comparison, the high-latitudes jets' maximum speeds are $\sim 190\ m\,s^{-1}$ for the same simulation. Additionally, for the largest planetary radii, 1.50 $R_\oplus$, the core of the equatorial jet extends deeper in the atmosphere, reaching below the cloud top pressure level.

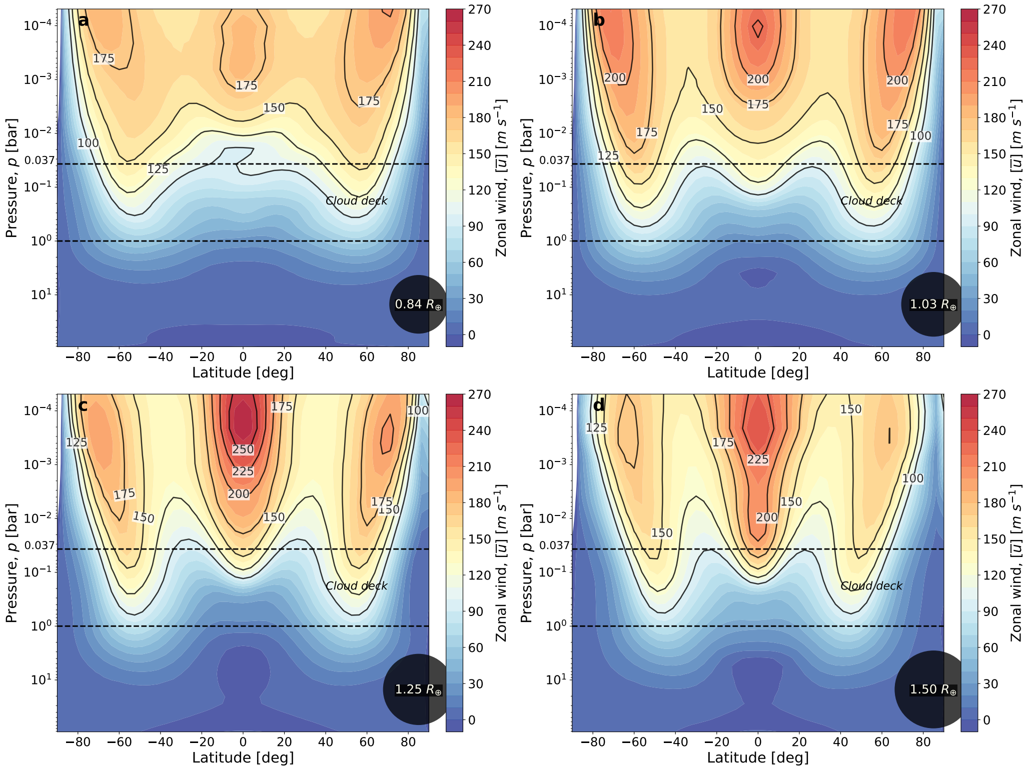

Figure 3.26: The zonal and time-averaged zonal wind fields in $m\,s^{-1}$ in pressure versus latitude for four different planets following the 20% Fe mass-radius relationship with the same instellation as TRAPPIST-1 c. Data is time averaged for 10 orbits. The isotachs are marked with solid black lines. The cloud deck extends from 1 to 0.037 *bar* and is defined by two dashed black lines. The planetary radius is displayed inside the black dot in the lower right corner, representing the relative size of each modelled planet.

The zonal wind field at the cloud top levels can be seen in Figure 3.27 for the four selected cases. As suggested by Figure 3.26, the equatorial jet is only present in the three largest planetary radii. For the largest planetary radii, the equatorial jet maximum speed increase from $\sim 150\ m\,s^{-1}$ (in the 1.03 $R_\oplus$ case) to $\sim 210\ m\,s^{-1}$ (in the 1.5 $R_\oplus$ case). In contrast, the maximum speed of the high-latitudes jets is more stable, peaking $\sim 190\ m\,s^{-1}$ in the 1.03 $R_\oplus$ and 1.25 $R_\oplus$ cases. The high-latitudes jet maximum speeds decrease from the 1.25 $R_\oplus$ to the 1.5 $R_\oplus$ simulation. In all studied planetary radii, the maximum speed of the high-latitudes jets occurs at about 45° E, while the maximum speed of the equatorial jet occurs just east of the morning terminator ($\sim$ 80° W - 60° W). In the three largest planetary radii, the intensity of the equatorial jet decreases in the vicinity of the evening terminator region and increases at the morning terminator. Additionally, as the planetary radius increases, the high-latitudes jets are displaced to lower latitudes.

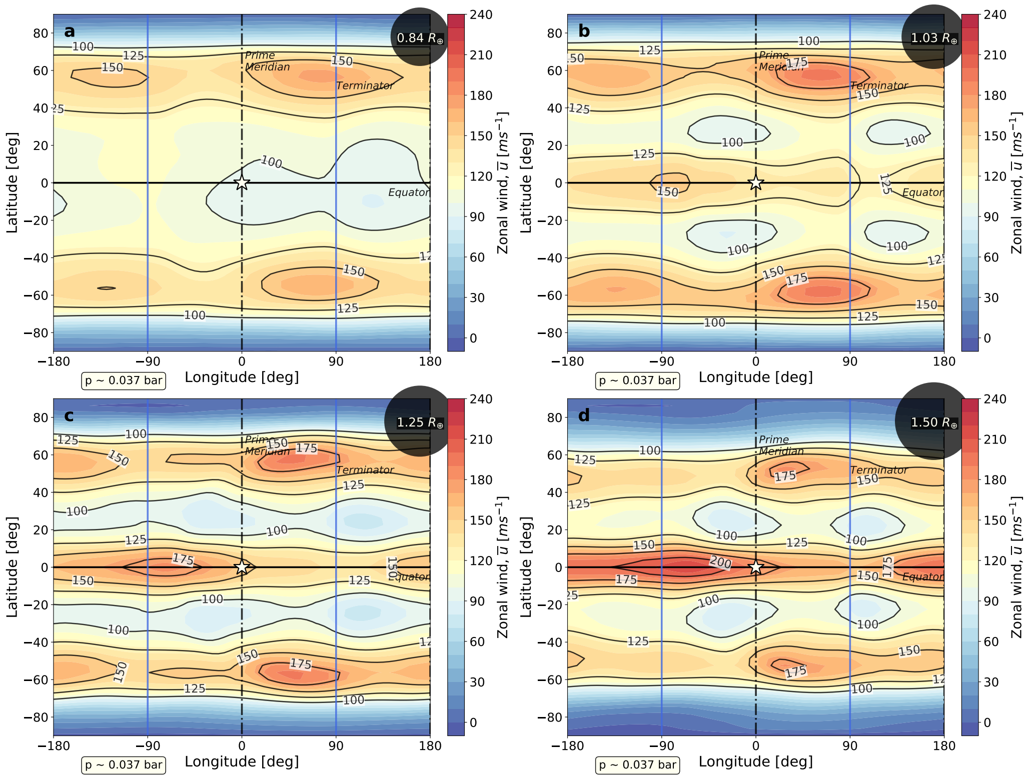

Figure 3.27: Time-averaged zonal wind fields in $m\,s^{-1}$ in latitude versus longitude for the clouds tops at $p \sim 0.037\ bar$ for four different planets following the 20% Fe mass-radius relationship with the same instellation value as TRAPPIST-1 c. Data is averaged for 10 orbits. The isothermals are represented by solid black lines. The substellar point is marked with a white star. The terminators, equator and prime meridian are identified by solid blue, solid black and dashed black lines, respectively. The planetary radius is displayed inside the black dot in the upper right corner, representing the relative size of each modelled planet.

The overall impact of increasing planetary radius in the synthetic observables can be seen for the reflection (Figure 3.28) and emission (Figure 3.29) phase curves. The increment in planetary radius will lead to a larger surface area available to either reflect or emit radiation. As a consequence, the major impact from increasing planetary radius will be an overall increase in planet-to-star contrast values for both the reflection and emission phase curves (see Table 3.4). For instance, the asymmetry discussed for the reflection phase curve 2.66 - 2.92 μm (**section 3.2.6.**) will remain in all studied cases (Figure 3.28).

As for the thermal phase curves, the increase in planetary radius will lead to an increase in the amplitude value of each phase curve (see Figure 3.29 and data in Table 3.4), with significant changes regarding the peak emission. For instance, the *continuum* thermal phase curves for the largest planetary radius (1.5 $R_\oplus$) (e.g., 9.02 - 9.39 μm spectral band in Figure 3.29 **(d)**) will have its peak emission occurring closer to orbital phase 0 in comparison with the smallest planetary radii (see Table 3.4). Since the OLR field responds in first approximation to the temperature field, this result can be interpreted as a consequence of a displacement of the cloud top temperature maximum towards the substellar region and the appearance of strong high-latitude temperature maxima around 60° N/S (see Figure 3.25 **(d)**), both seen in the 1.5 $R_\oplus$ case.

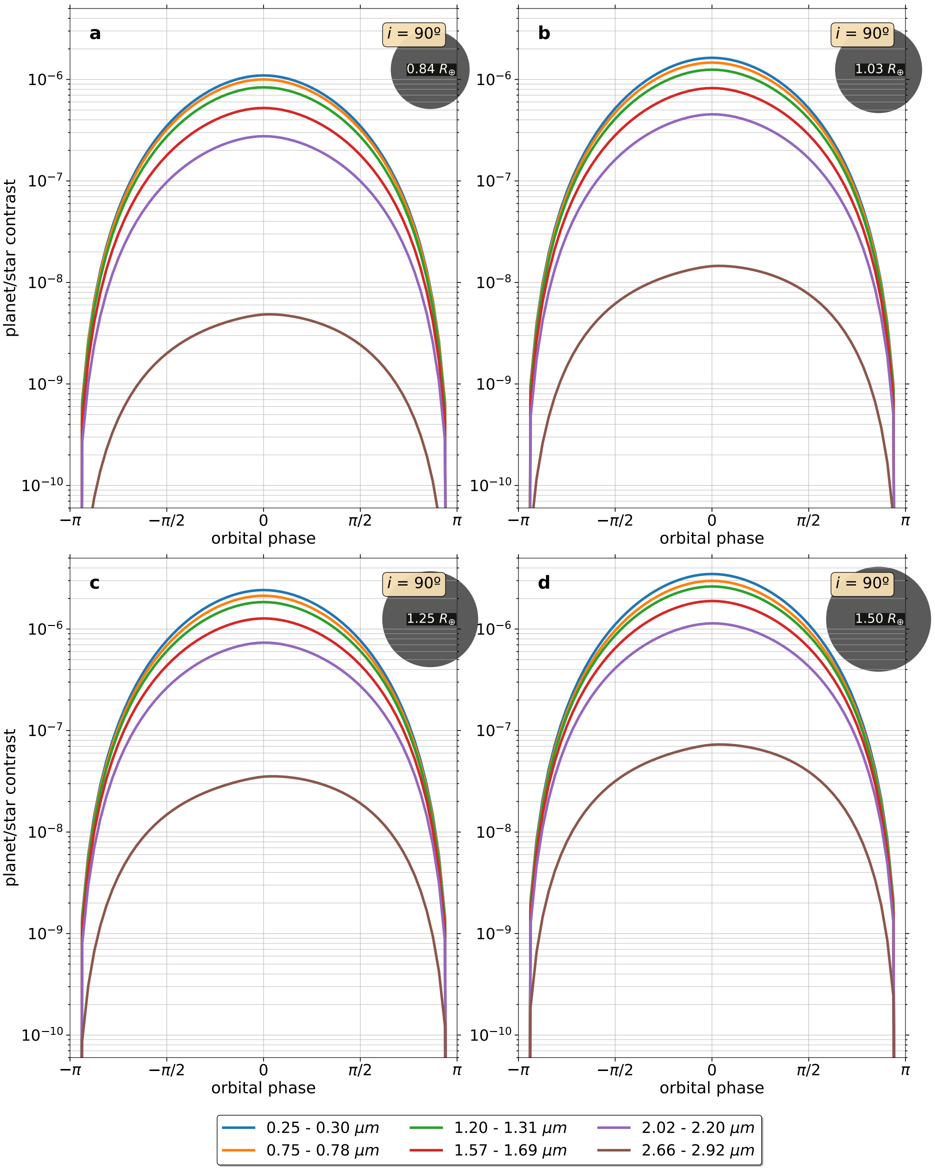

Figure 3.28: Reflection phase curves for an inclination i of 90° for four different planets following the 20% Fe mass-radius relationship with the same instellation as TRAPPIST-1 c and for six spectral bands.

Table 3.4: Reflection and emission phase curves parameters calculated for four different planets following the 20% Fe mass-radius relationship and compared with the reference simulation (TRAPPIST-1 c)

Phase Curve	**Reflection**	**Emission**		
Test	**Maximum**	**Maximum**	**Amplitude**	**Peak emission**
Reference	$1.87 \cdot 10^{-6}$	$8.87 \cdot 10^{-6}$	$2.75 \cdot 10^{-6}$	78.7° E
0.84 $R_\oplus$	$1.10 \cdot 10^{-6}$	$5.19 \cdot 10^{-6}$	$1.61 \cdot 10^{-6}$	78.7° E
1.03 $R_\oplus$	$1.63 \cdot 10^{-6}$	$7.63 \cdot 10^{-6}$	$1.98 \cdot 10^{-6}$	84.4° E
1.25 $R_\oplus$	$2.42 \cdot 10^{-6}$	$1.21 \cdot 10^{-5}$	$5.01 \cdot 10^{-6}$	73.1° E
1.50 $R_\oplus$	$3.49 \cdot 10^{-6}$	$1.93 \cdot 10^{-5}$	$1.08 \cdot 10^{-5}$	56.3° E

Notes: Selected spectral bands: **(i)** reflection: 0.25 - 0.30 μm; **(ii)** emission: 9.02 - 9.39 μm.

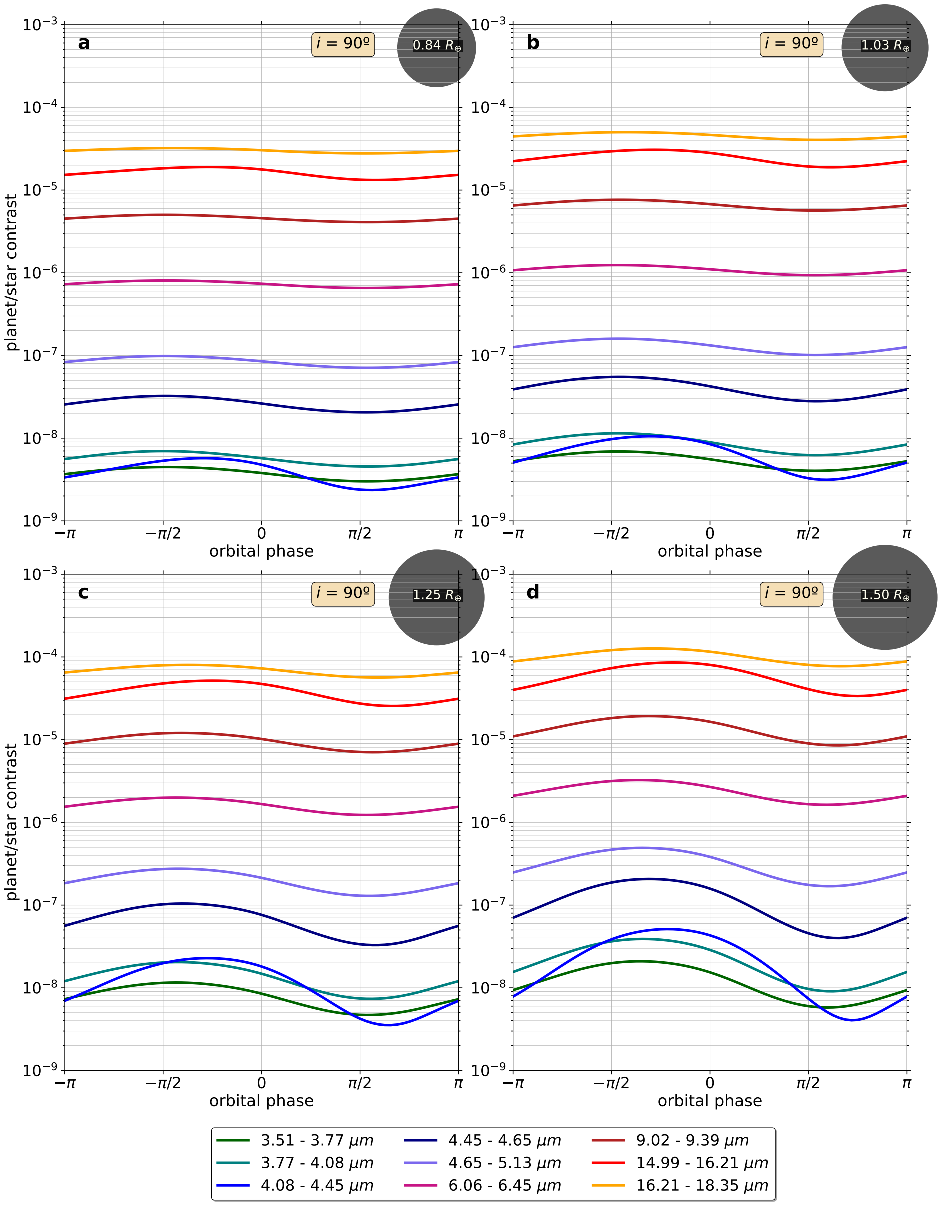

Figure 3.29: Emission phase curves for an inclination i of 90° for four different planets following the 20% Fe mass-radius relationship with the same instellation as TRAPPIST-1 c and for nine spectral bands.

3.4.2 Spin-Orbit resonances

In this section, I compare the large-scale circulation and observables (emission phase curves), assuming that TRAPPIST-1 c is either a synchronous rotator (i.e., the reference) or is captured into a 2:1 spin-orbit resonance (2 rotations per one orbit). In addition, the 3:2 spin-orbit resonance was also studied, and its thermal field and dynamical results (zonal wind fields) are similar to the 2:1 spin-orbit resonance case.

The time-mean temperature field at the cloud top ($p \sim 0.037\ bar$) is represented in Figure 3.30 **(a, b)**. Unlike the synchronous rotator, where the maximum of the thermal emission occurs *east* of the substellar point (see panel **(a)**), the temperature maximum in the 2:1 spin-orbit resonance occurs in the vicinity of the *instantaneous* substellar point. The chevron-like pattern seen in the synchronous rotator is absent in the 2:1 spin-orbit resonance.

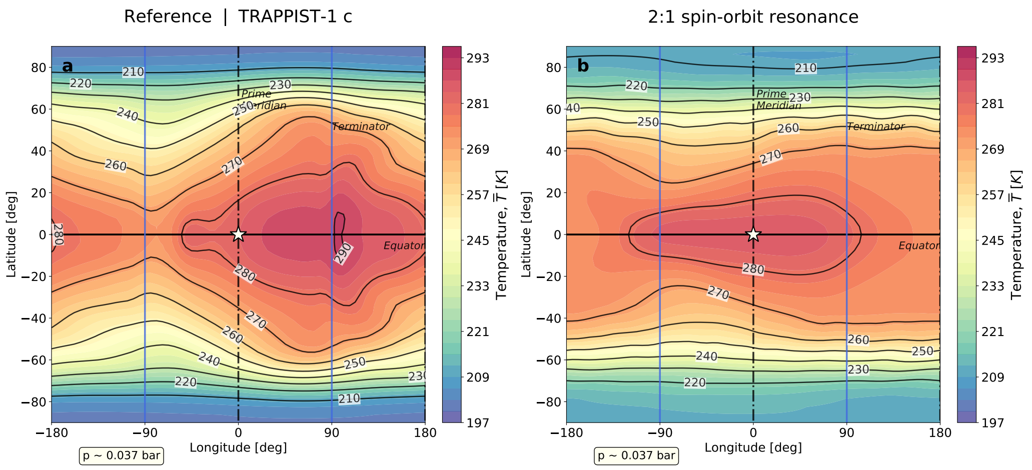

Figure 3.30: Time-mean temperature fields in K in latitude versus longitude at the cloud top ($p \sim 0.037\ bar$) for: **(a)** the synchronous rotator; and **(b)** and the 2:1 spin-orbit resonance case. The data is time averaged for ten orbits of TRAPPIST-1 c in the synchronous rotator case. In the 2:1 spin-orbit resonance, the time average is done considering the instants where the substellar point is located at longitude 0°. Isothermals are depicted by solid black lines in both panels. The substellar point is marked by a white star, while the terminators, equator and prime meridian are identified by solid blue, solid black and dashed black lines, respectively.

The zonal wind field shows significant differences between the synchronous rotator and the 2:1 spin-orbit resonance case. The major dynamical difference is the absence of the eastward zonal superrotation jet in the 2:1 spin-orbit resonance (see Figure 3.31 **(b)**). Instead, at the equator, there are two regions of westward motion: a slightly stronger (maximum speeds of $-25\ m\,s^{-1}$) in the uppermost levels of the atmosphere and a second weaker one (maximum speeds of $-20\ m\,s^{-1}$) centred at the cloud base level ($1\ bar$). Between these two regions, centred at $\sim 10\ mbar$, there is an eastward motion region with speeds reaching $\sim 75\ m\,s^{-1}$. The 2:1 spin-orbit resonance case also shows two strong (maximum speed: $\sim 180\ m\,s^{-1}$) eastward high-latitudes jets, nevertheless less intense than the synchronous rotator case (maximum speed: $\sim 210\ m\,s^{-1}$). In both cases, the high-latitudes jets have a similar, deep penetration through the cloud deck.

At the cloud top ($p \sim 0.037\ bar$) the time-mean zonal wind field in the 2:1 spin-orbit resonance (see Figure 3.31 **(d)**) is characterised by an overall *eastward* motion. The two high-latitudes jets are centred at $\sim 50°$ N/S with maximum speeds of $\sim 125\ m\,s^{-1}$. These jets assume a zonal band shape, unlike the zonal wind isotachs in the synchronous rotator case (see Figure 3.31 **(c)**). The zonal wind isotach disposition in zonal bands is a consequence of the fast and asynchronous rotation (the rotation period equals 1.21 Earth days). As suggested by panel **(b)**, the equatorial jet at the cloud top in panel **(d)** is much weaker than the high-latitudes jets.

The equatorial zonal wind field in Figure 3.31 **(f)** is still directed eastwards for most of the atmosphere, except for the westward jet west of the instantaneous substellar point in the upper atmosphere (centred at $\sim 0.1\ mbar$). Globally, the equatorial zonal wind field in the 2:1 spin-orbit resonance case is much less intense than in the synchronous rotator (see Figure 3.31 **(e)**). The normalised wind vectors in the uppermost levels depict a strong upward motion on the dayside and a strong downwelling motion on the nightside for the 2:1 spin-orbit resonance.

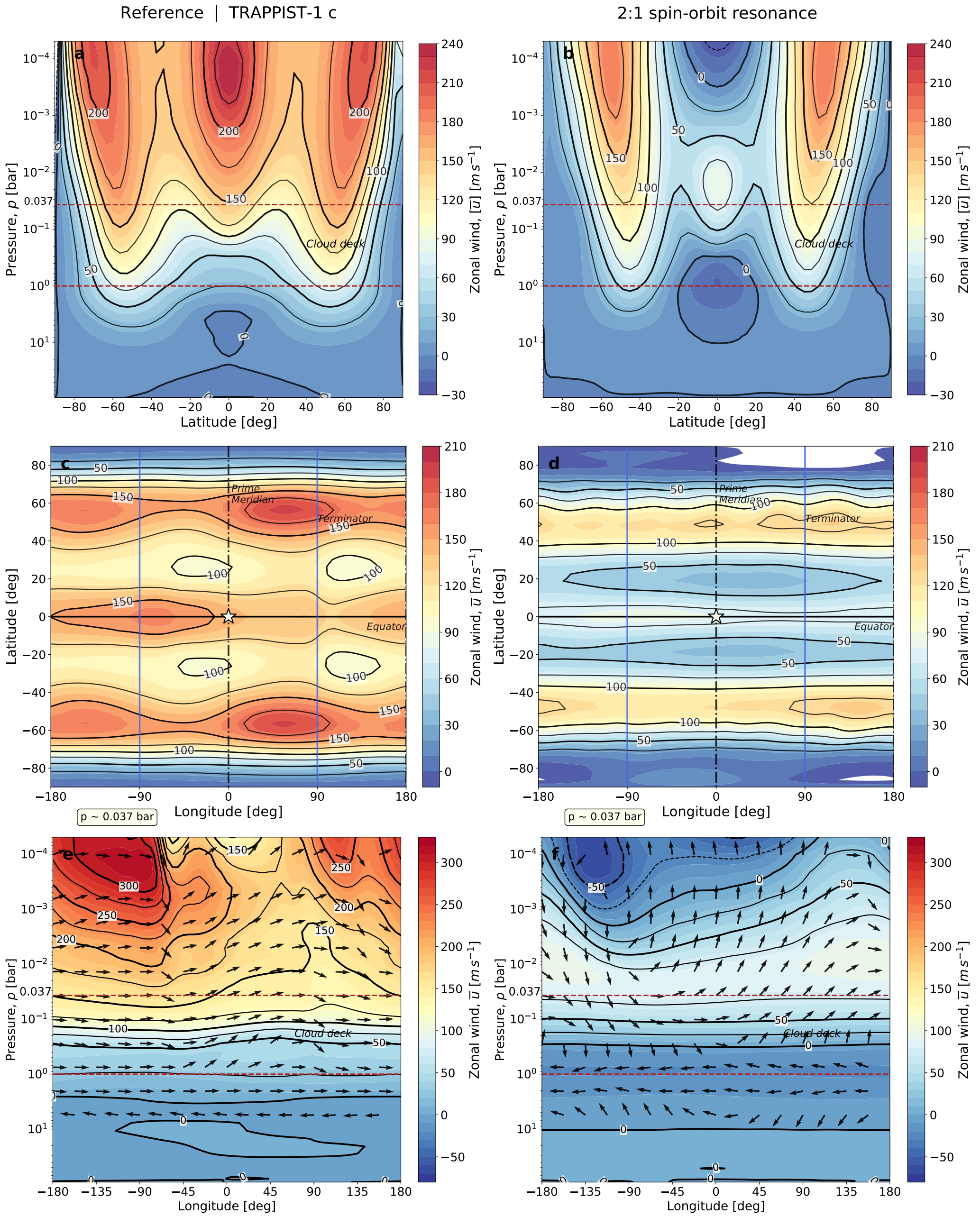

Figure 3.31: Zonal wind fields for the synchronous rotator **(a, c, e)** and the 2:1 spin-orbit resonance **(b, d, f)** simulations of TRAPPIST-1 c with Venus-like clouds. The top panels **(a, b)** depict the zonal and time-averaged zonal wind fields, $[\overline{u}]$ in $m\,s^{-1}$, in pressure versus latitude. The mid-panels **(c, d)** depict the cloud top ($p \sim 0.037\ bar$) time-mean zonal wind field $\overline{u}$ in $m\,s^{-1}$ in latitude versus longitude. The bottom panels **(e, f)** depict the time-mean zonal wind $\overline{u}$ in $m\,s^{-1}$ at the equator in pressure versus longitude. The data is time-averaged throughout ten orbits of TRAPPIST-1 c in panels **(a, b, c, e)** and for the time instants when the local substellar point is at longitude 0° in panels **(d, f)**. In panels **(e, f)** the normalised wind vectors are represented with black arrows (the vertical component is multiplied by the ratio between the horizontal and vertical spacings). The cloud deck extends from 1 bar to 0.037 bar and it is defined by the red dashed lines. In all panels, the zonal wind isotachs are represented with an interval of 50 $m\,s^{-1}$ (or 25 $m\,s^{-1}$) by thick (thin) solid black lines.

The changes in the large-scale circulation and temperature fields imposed by non-synchronous rotation will significantly impact the thermal phase curves. I represent in Figure 3.32 two thermal phase curves: the 14.99 - 16.21 μm (in the vicinity of 15 μm strong carbon dioxide absorption band) and the 11.43 - 12.50 μm (in the *continuum*) for the synchronous rotator case and two higher-order spin-orbit resonances, the 2:1 and 3:2 cases.

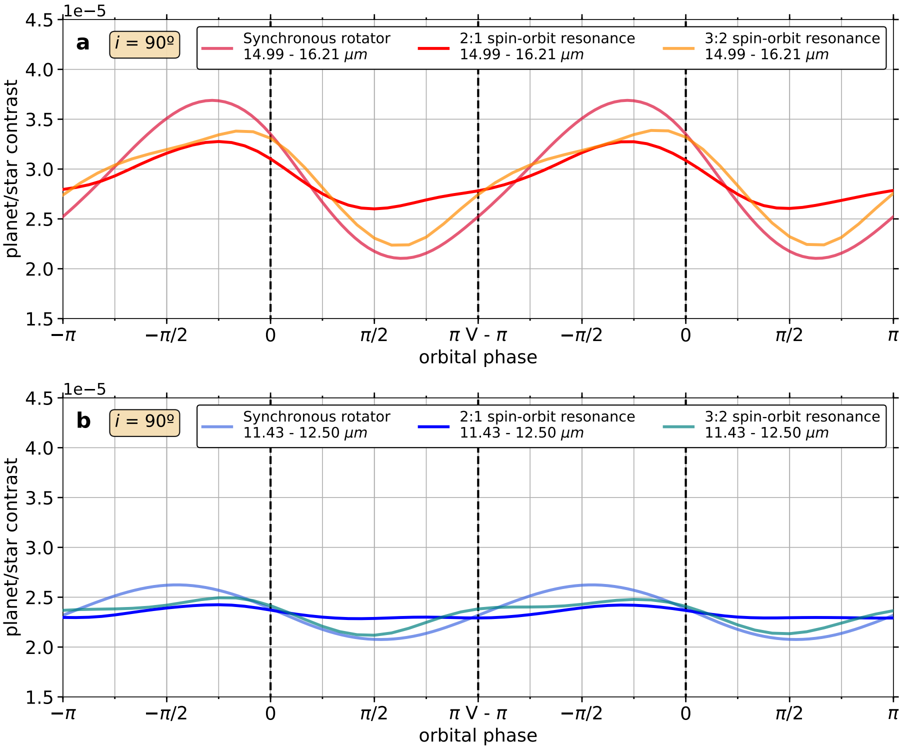

Figure 3.32: Thermal phase curves for three planetary rotation rates of TRAPPIST-1 c: synchronous rotator, 2:1 spin-orbit resonance, and 3:2 spin-orbit resonance. Two spectral bands are represented: in the upper panel **(a)** 14.99 - 16.21 μm, under the influence of the 15 μm carbon dioxide absorption band, for the synchronous rotator (pale red line), 2:1 spin-orbit resonance (deep red line) and 3:2 spin-orbit resonance (orange line); and the lower panel **(b)** 11.43 - 12.50 μm, representing the *continuum*, for the synchronous rotator (pale blue line), 2:1 spin-orbit resonance (deep blue line) and 3:2 spin-orbit resonance (green line).

The 14.99 - 16.21 μm spectral band amplitude modulation is more complex for the higher-order spin-orbit resonances compared with the symmetry found in the synchronous rotator case. Although the peak emission for the synchronous rotator and 2:1 spin-orbit resonance is almost in phase, the lowest emission is out of phase, happening earlier for the 2:1 spin-orbit resonance. In contrast, the minimum thermal emission for the synchronous rotator and 3:2 spin-orbit resonance are in phase, while the peak emission for the latter occurs at a later orbital phase. The amplitudes of the 14.99 - 16.21 μm thermal phase curves also differ between the three studied cases, with the 2:1 spin-orbit resonance having the lowest amplitude.

The 11.43 - 12.50 μm spectral band phase curves show significant differences in peak emission and amplitude between the three rotation states. The 2:1 spin-orbit resonance phase curve has the lowest amplitude, making it challenging to separate maxima and minima. In the 3:2 spin-orbit resonance thermal phase curve, the minima follow the maxima after a few orbital phases, followed by a period with low amplitude modulation. In the synchronous rotator case, the maxima and minima are equidistant, and the amplitude is larger compared to the other rotation states.

The amplitude values of the thermal phase curves in Figure 3.32 can be found in Table 3.5 together with the orbital phase of the peak emission.

The modulations found in the thermal phase curves of the higher-order spin-orbit resonances are likely the result of observing geometry and the OLR maps. More importantly, the thermal phase curves reflect the impact of the planetary rotation state in the temperature fields. In the Table 3.5 the peak thermal emission of the 2:1 and 3:2 spin-orbit resonance occurs closer to orbital phase 0, but still *east* of *instantaneous* substellar point.

Table 3.5: Emission phase curves parameters for TRAPPIST-1 c

Rotation state	**Spectral Band**	**Minimum**	**Maximum**	**Amplitude**	**Orbital phase**
	[μm]	[10^{-5}]	[10^{-5}]	[10^{-5}]	[deg]$^{(*)}$
1:1	14.99 - 16.21	2.104	3.689	1.585	$-50.6°$
2:1	14.99 - 16.21	2.601	3.276	0.676	$-45°$
3:2	14.99 - 16.21	2.237	3.388	1.151	$-30°$
1:1	11.43 - 12.50	2.076	2.624	0.548	$-78.7°$
2:1	11.43 - 12.50	2.285	2.425	0.140	$-45°$
3:2	11.43 - 12.50	2.119	2.494	0.376	$-45°$

Notes: Rotation states: **1:1**, synchronous rotator; higher-order spin-orbit resonances: **2:1**, 2 rotations per 1 orbit; **3:2**, 3 rotations per 2 orbits. (*) The orbital phases were converted from radians to degrees to ease the interpretation.

The OLR maps for the two spectral bands 14.99 - 16.21 μm and 11.43 - 12.50 μm are presented in Figure 3.33 for the three studied planetary rotation states. The analysis reveals that the maximum thermal emission occurs, in *all* cases, *east* of the (instantaneous or permanent) substellar point. Furthermore, as explained in **section 3.2.6**, these two spectral bands allow probing of two different atmospheric levels. The conclusions drawn in that previous section are valid in the 2:1 and 3:2 spin-orbit resonances.

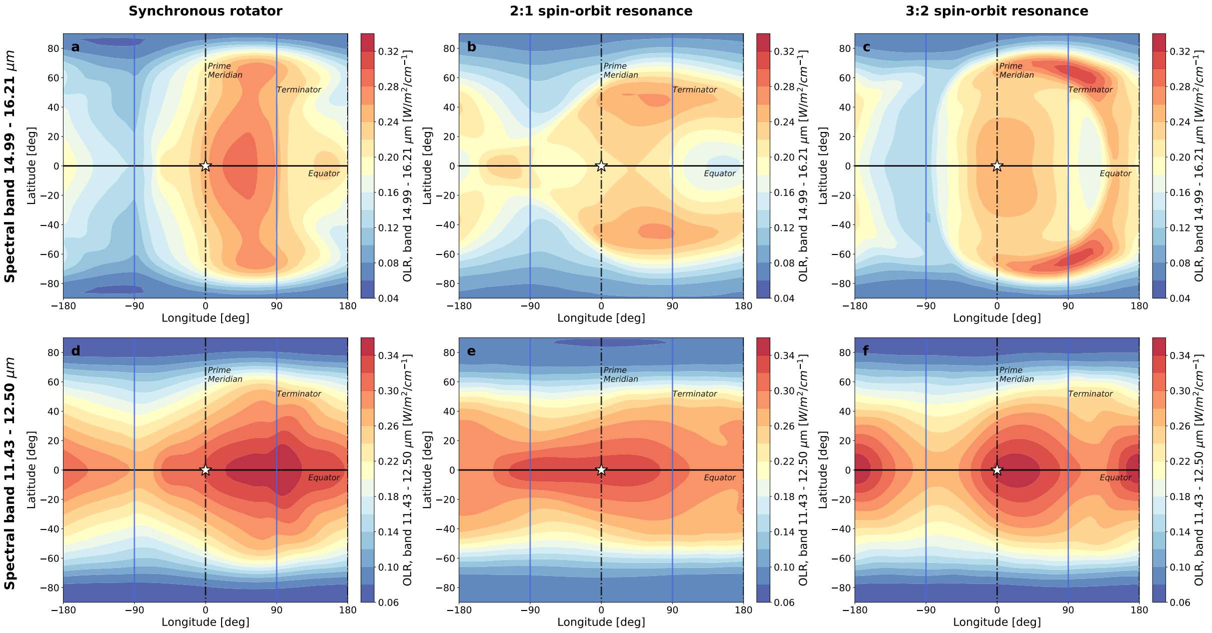

Figure 3.33: OLR maps for three planetary rotation rates of TRAPPIST-1 c. The upper panels **(a, b, c)** represent the OLR maps of the spectral band 14.99 - 16.21 μm for the: **(a)** synchronous rotator; **(b)** 2:1 spin-orbit resonance; and **(c)** and 3:2 spin-orbit resonance. The lower panels **(d, e, f)** depict the OLR maps of the spectral band 11.43 - 12.50 μm for the: **(d)** synchronous rotator; **(e)** 2:1 spin-orbit resonance; and **(f)** 3:2 spin-orbit resonance. The data for the synchronous rotator is time-averaged throughout ten orbits of TRAPPIST-1 c. The data in the higher-order resonances **(b, c, e , f)** is time-averaged for the time instants when the *instantaneous* substellar point is located at longitude 0°, allowing for comparison of the OLR fields between the three planetary rotation states. The white star marks the substellar point and the solid blue lines depict the terminators. The equator (prime meridian) is identified by a solid (dashed) black line.

4 Conclusions and Final Remarks

In this work, I performed simulations of Venus-like exoplanetary atmospheres, using TRAPPIST-1 c planetary parameters as a template, using two cases: Venus-like clouds (reference simulation) and clear-sky conditions. Finally, I performed a parametric study, following a 20% Fe mass-radius relationship and using two higher-order (3:2 and 2:1) spin-orbit resonances. I analysed the simulated thermal structure and large-scale atmospheric circulation. I produced synthetic observables from the Generic-GCM outputs: reflection and emission phase curves for all simulations and transmission spectra for TRAPPIST-1 c.

I made a series of assumptions when modelling TRAPPIST-1 c with a Venus-like atmosphere. In the first place, there is currently no evidence suggesting that TRAPPIST-1 c has an atmosphere. If the planet has an atmosphere, it might be significantly different from Venus, with a different gas mixture, aerosols or even surface atmospheric pressure. For instance, it is unknown if sulphuric acid clouds are common on other planets. Furthermore, and despite the advances in constraining the TRAPPIST-1 c's mass, radius, semimajor axis and instellation put forward by the work of Agol et al. (2021) the remaining planetary parameters are unknown. The planet's eccentricity and obliquity are assumed to be zero, which are reasonable assumptions attending the planetary system's orbital architecture. The rotation rate is not constrained, and other rotation states might occur. In this work, I modelled the 3:2 and 2:1 spin-orbit resonances, which are more likely to occur under significant orbital eccentricity (Makarov et al., 2012). However, at least other two rotation states might exist for highly-irradiated exoplanets orbiting M-dwarf stars: **(i)** synchronous state with libration, which might be occurring in the TRAPPIST-1 planetary system according to Vinson et al. (2019)); **(ii)** and non-synchronous rotation from thermal tides, less likely for TRAPPIST-1 c (Turbet et al., 2020a) (for further details see **Appendix I**).

This section highlights the main results obtained during this Master.

- **The simulated Venus zonal wind speeds progressively decrease with decreasing insolation**. The Generic-GCM was first used to simulate the atmosphere of planet Venus, using as input files an atmosphere in superrotation. The Generic-GCM reproduces the superrotation pressure range and high-latitudes jets seen in the IPSL-VGCM simulated Venus (Garate-Lopez and Lebonnois, 2018). Following this result, I decided to perform tests with the Generic-GCM by increasing the planet's orbital distance (from 0.72 *AU* to 0.9, 1, and 1.2 *AU*), leading to lower energy input in the Climate system and, consequently, to a decrease in zonal wind momentum and a weaker day-to-night energy redistribution. The superrotation is a robust dynamical feature for the range of insolation values explored.

- **The simulated TRAPPIST-1 c atmosphere is *warmer* than Venus**. TRAPPIST-1 emits more radiation in the NIR compared to the visible wavelengths. The carbon dioxide dominated atmosphere will absorb the SW radiation, effectively contributing to the overall warming of the TRAPPIST-1 c atmosphere. The dense atmosphere will be responsible for a large decrease in the SW heating rate by more than four orders of magnitude (from TOA to the surface). The LW rate contributes to *cool* the atmosphere except in the vicinity of the cloud base level. Warming at this level is probably caused by the cloud cover absorbing LW radiation emitted by the hot planetary surface (in agreement with Lebonnois et al. (2010) and Lebonnois et al. (2015)).

- **Day-night heat redistribution in TRAPPIST-1 c is done through zonal superrotation jets and meridional circulation**. The zonal circulation is characterised by **three** eastward jets (classical result of simulations of highly-irradiated synchronous rotators (Showman and Polvani, 2011)). The jets have a deep penetration below the cloud deck and cores located in the uppermost layers of the atmosphere:

- ▷ **Equatorial zonal superrotation jet**: with a core located between $\sim 0.4\ mbar$ and $0.06\ mbar$, and maximum speed slightly larger than $\sim 230\ m\,s^{-1}$. At the cloud top, the zonal and time-averaged zonal wind is $\sim 150\ m\,s^{-1}$, peaking at $\sim 160\ m\,s^{-1}$ east of the morning terminator);
- ▷ **High-latitudes jets**: with cores located between 60° N/S and 70° N/S, and speeds of $\sim 210\ m\,s^{-1}$ at $\sim 0.1\ mbar$. They have an equatorward tilted structure, deeper penetration (clear signature at the cloud base) and are faster at the cloud top than the equatorial zonal superrotation jet. These jets have a large width variation with maximum equatorward expansion at $\sim$ 70° E and 140° W.

The **Meridional circulation** comprises **two** large cells, one per hemisphere (northern and southern), crossing the pole and redistributing heat from dayside to nightside. According to the conservation of angular momentum, the jets (equatorial and high-latitudes jets) form at the cells' boundaries (shown in the global mass streamfunction). Heat transport by the meridional circulation is mainly explained by its **mean meridional circulation** component, with a minor poleward contribution of the *stationary waves* in the mid-latitudes.

The nightside equator has a similar ($\Delta T < 5\ K$) temperature profile to the substellar region from ground to $\sim 10\ mbar$. Between $\sim 15\ bar$ and $\sim 10\ mbar$, this region is *warmer* than the remaining nightside hemisphere, suggesting an efficient day-night energy redistribution mechanism is present throughout a significant part of the atmosphere.

- **TRAPPIST-1 c temperature field at the cloud top ($p \sim$ 0.037 bar) shows a distinctive chevron-like pattern and an eastward shift of the temperature maximum from the substellar point**. The two features are characteristic in simulations of tide-locked planets and can be interpreted as a result of warm air advection by the equatorial zonal superrotation jet (Showman and Polvani, 2011). In the simulations, the hotspot eastward offset is located *east* of the evening terminator at $\sim$ 100° E. In addition, two temperature local relative maxima appear at the equator at longitudes $\sim$ 45° W and $\sim$ 150° E, and might be related to **adiabatic warming** from **subsidence**.
- **Evident signature of an equatorial wave in the modelled cloud top of TRAPPIST-1 c**. The wave has an *eastward* propagation, average wave phase speed of $\sim 130\ m\,s^{-1}$ and period of $\sim$ 17.5 hours. Its signature is evident in the dayside hemisphere, east of the 50° W region, although *transient* in the nightside (in particular, east of the antistellar point).
- **Removal of Venus-like aerosols from simulations results in a warmer deep atmosphere and the development of upper atmospheric polar warming**. As a consequence of SW energy penetrating more deeply into the atmosphere, the surface temperature increases to $\sim 850\ K$ in the clear-sky conditions (an $\sim 160\ K$ increase compared to the reference simulation with Venus-like clouds). Polar warming (at latitudes higher than $\sim$ 70° N/S) replaces the cold poles in the simulation with Venus-like clouds. SW energy's nearly homogeneous absorption leads to the disappearance of the equator-pole temperature gradients seen in Venus-like clouds simulation (observed above 10 bar). Furthermore, the thermal phase curves in the CO_2 absorption bands have a peak emission closer to the orbital phase 0, compared to the reference simulation with Venus-like clouds, while the *continuum* thermal phase curves have very low amplitudes. All these points suggest a different heat redistribution mechanism is present in the clear-sky simulation with the *continuum* thermal phase curves probing deeper levels in the atmosphere.
- **Reflection phase curves of TRAPPIST-1 c reach a planet-to-star contrast on the order of 10^{-6} offering a possible detection with JWST and other future instruments**. The result highlights the

importance of studying *high albedo* sulphuric acid aerosols, strengthening the case for Venus-like atmospheres in the future.

- **Different atmospheric levels can be surveyed with different thermal spectral bands providing information into the large-scale atmospheric circulation on mesosphere and in the cloud top**. In every thermal spectral band, the planet's peak emission occurs before the secondary eclipse, corresponding to a maximum emission **east** of the substellar point. However, the eastward offset of the peak emission occurs in *different* orbital phases, suggesting that different spectral bands are probing different atmospheric levels:

  - ▷ Carbon dioxide absorption bands (e.g., 4.3 μm, 15 μm) have larger amplitudes and later peak emission. The largest OLR values are located between longitudes $\sim 45°$ W and $\sim 180°$ E, being considerably lower outside this longitudinal range. This OLR's strong dependence on longitude leads to a *larger* amplitude of the thermal phase curve. The OLR peak emission occurs *closer* to the substellar point ($\sim 51°$ E): a *smaller* eastward emission offset leads to peak emission in the thermal phase curve to occur at a *later* orbital phase. The OLR field matches the $\sim 1\ mbar$ temperature allowing for remote sensing of **mesospheric dynamics**;
  - ▷ *Continuum* spectral regions have smaller amplitudes and earlier peak emission. The OLR field has a **chevron-like pattern** with *lower* longitudinal OLR variation leading to a *lower* amplitude thermal phase curve. A *larger* eastward shift of the OLR peak emission (at $\sim 79°$ E) leads to an *earlier* (compared to carbon dioxide absorption bands) peak emission in the thermal phase curve. The OLR field structure matches the **cloud top** temperature field, allowing for remote sensing of **cloud top dynamics**: the eastward hotspot offset is likely due to warm air advection from the substellar region by the equatorial zonal superrotation jet.

- **Venus-like clouds will screen almost all but the strongest carbon dioxide absorption bands in the simulated transmission spectrum of TRAPPIST-1 c**. Two cases were explored: **(i)** Venus-like clouds (aerosol modes 1 and 2); and **(ii)** clear-sky conditions. The strongest CO_2 spectral lines (centred at 2.0, 2.8, 4.3, and 15 μm) have the largest relative effective height due to this gas being well-mixed throughout the atmospheric column, in particular above the upper haze altitude, which will be probed by transmission spectroscopy. The high *continuum* level will hide spectral features (e.g., 4.0 μm SO_2) or make detection challenging by lowering their relative transit depth (e.g., 7.3 μm SO_2 absorption features). The minor components have larger concentrations at and below the cloud deck, compromising their detection with transmission spectroscopy. The strongest CO_2 spectral lines will likely indicate a presence of a *terrestrial* atmosphere, while detection of weaker CO_2 features could suggest a higher abundant, Venus-like, carbon dioxide atmosphere (Lincowski et al., 2018). The **pressure broadening effect** might enable the detection of the 4.8 μm CO_2 spectral band, which could indicate a high-pressure CO_2 atmosphere. In contrast, future observations of transmission spectra flattened by sulphuric acid aerosols will not exclude *per se* other atmospheres (e.g., oxygen-dominated atmospheres).

- **Studying the mass-radius relationship** has had the main outcomes:

  - ○ **Cloud top temperature field**. Larger planetary radii will lead to more obvious chevron-like patterns, overall *warmer* temperature fields, and a smaller eastward shift of the temperature maximum. Two temperature maxima appear in the high-latitudes (at $\sim 60°$ N/S and $\sim 45°$ E) for the two largest planetary radii;

  - **Zonal wind field**. The equatorial zonal superrotation and the two high-latitudes jets are present across all simulations. The three jets have similar maximum speeds for the two smallest planetary radii, while for larger planetary radii, the equatorial jet becomes progressively faster than the high-latitudes jets. For larger planetary radii, the equatorial jet has a deeper penetration in the atmosphere, and in the smallest studied planetary radius, it does not reach the cloud top level;
  - **Phase curves**. The larger planetary radii will lead to a larger surface area available to reflect or emit radiation. The outcome is an *increase* in planet-to-star contrast with *larger* planetary radii. In the case of thermal phase curves, larger planetary radii will lead to larger amplitude values and smaller eastward shifts of the peak emission.

- **Studying the Spin-orbit resonances**. I modelled TRAPPIST-1 c with Venus-like clouds under higher-order spin-orbit resonances: 2:1 and 3:2 to study the impact of planetary rotation rate in the large-scale circulation and observables (thermal phase curves). The main results of the higher-order spin-orbit resonances (both 2:1 and 3:2 cases) compared to the synchronous rotator are as follows:
  - **Cloud top temperature field**. The zonal disposition of the isothermals replaces the chevron-like pattern;
  - **Zonal wind field**. The equatorial zonal superrotation jet is absent. The zonal circulation is dominated by two eastward high-latitudes jets (centred at $\sim 60°$ N/S), with maximum speeds of $\sim 180\ m\,s^{-1}$ at $\sim 1\ mbar$. These jets have deep penetration in the atmosphere, reaching the cloud deck;
  - **Thermal phase curves**. The planetary rotation rate impacts the modulation of the amplitude and peak emission's orbital phase, potentially suggesting that thermal phase curves can be used to constrain the kind of rotation state. This result is of great interest for future studies, as there is no observational evidence on exoplanets' planetary rotation rate.

As a final remark, I want to reflect on the skills learned and used to support the immense work for this project. I learned how to work independently with the Generic-GCM, solve technical problems, and analyse model outputs. I developed several `Python` codes to interpret model outputs, including for the thermal structure and large-scale circulation. One script produced is the `Phase Curves Assessment Routine` (PCAR) (see **Appendix II**), which allows the user to compute either reflection and emission phase curves, using the Generic-GCM output TOA fluxes and a stellar flux as inputs. Part of the results from this Master Dissertation has contributed to two conferences:

- **Quirino D**, Gilli G, Navarro T, Turbet M, Fauchez T, Machado P. "3D Climate modelling of TRAPPIST-1 c with a Venus-like atmosphere: large-scale circulation and observational prospects". EGU, 2022;
- Gilli G, **Quirino D**, Navarro T, Turbet M. "Planetary parameters impact in the large-scale circulation of Venus-like exoplanetary atmospheres and observational prospects". EPSC, 2021.

Furthermore, the results presented in this Master Dissertation are foreseen to be published in **two peer-reviewed publications**, currently in preparation.

5 Future Studies

The research activities done during this Master's project will be continued in future studies:

- **Implementation of a simplified sulphuric acid microphysical cloud model into the Generic-GCM.** As shown by this work, the overall *warmer* TRAPPIST-1 c atmosphere compared to Venus's VIRA temperature requires an update from the prescribed cloud model in the Generic-GCM, which currently depends only on the pressure. Developing a cloud model is an ambitious task as cloud modelling can be very complex as radiative feedbacks can profoundly impact cloud distribution. Nonetheless, the implementation of consistent cloud formation in the Generic-GCM appears to be fundamental through its impact on dynamics, radiative transfer and photochemistry. This crucial work will also rely on existing model developments done by our French collaborators, who already included a simplified condensation water cloud model in the Generic-GCM to simulate the atmosphere of a temperate sub-Neptune (Charnay et al., 2021) and early-Venus (Turbet et al., 2021). Overall, one of the goals of this future work is to evaluate the impact of the formation of **binary sulphuric acid - water vapour clouds** on the observables to provide more realistic predictions to support an interpretation of JWST measurements of Earth-sized planets.

  We will follow the scheme in the PhD Thesis by *Aurelien Stolzenbach* (Stolzenbach, 2016), who developed a condensation cloud model for the IPSL-VGCM. The produced scheme will be included in the Generic-GCM to simulate the self-consistent formation, evolution and distribution of sulphuric acid - water vapour cloud in rocky planets orbiting M-dwarf stars. The simplified cloud model will include condensation and evaporation under a fixed particle size. In addition, I want to contribute to answering some of the following research questions:

  (1) *What is the spatial and temporal distribution of sulphuric acid - water vapour clouds and hazes? What is the thickness and pressure range of the cloud and haze layers? In particular, will there be global cloud coverage?* The results from this Master's work suggest that TRAPPIST-1 c cloud base temperature is higher than the condensation point of sulphuric acid. Therefore, the simplified cloud model could indicate the local altitude of the sulphuric acid condensation level, which is needed to define the cloud base.

  (2) *What are the consequences for the thermal structure, radiative tendencies, and large-scale atmospheric circulation (e.g., jet location, speeds, vertical motion, waves)?* Self-consistent cloud formation can impact radiative balance and energy redistribution in the atmosphere.

  (3) *What is the impact of planetary parameters (e.g., planetary rotation rate, mass-radius relationship, surface atmospheric pressure, instellation) have on the cloud and haze previously enumerated parameters?* A specific development from this Master's work is the different amplitude of thermal phase curves for different planetary rotation states. A simplified cloud model will assess the robustness of this result. Constraining the planetary rotation rate of an exoplanet is a much desired outcome for the exoplanetary science community.

  (4) *What are the observational prospects resulting from new synthetic observables (reflection and thermal phase curves and transmission spectra)?* The relatively high reflection contrast values $\mathcal{O}\ (10^{-6})$ obtained with the prescribed cloud deck offer a good prospect for the exploration of albedo inhomogeneities (Turbet et al., 2016) expected from implementing cloud variability. In this sense, the selection of sulphuric acid aerosols is crucial: combining the high albedo of these aerosols, and the short orbital distance of Venus-like exoplanets, offers one of the best cases for exploring the atmosphere dynamics of a rocky exoplanet. Furthermore, preferential cloud formation (for example, eastward of the substellar point as in (Kopparapu et al., 2017; Yang et al., 2014) and nightside hemisphere) will possibly impact OLR fluxes and the thermal phase curve parameters (orbital phase of the peak emission, amplitude modulation of the phase curve), likely updating the conclusions drawn in this work. Implementing the simplified cloud model will increase the variability of the OLR fluxes. Estimating the contrast level variability will be fundamental to assessing future observational prospects with JWST and E-ELT (and other future instruments). Ultimately, this development could lead to the detection of OLR variability, whose periodicity might indicate the presence of planetary waves (e.g., Kelvin, Rossby waves). As for the transmission spectra, a better estimation of the altitude of the upper haze at the terminator will constrain the *continuum* level, allowing for a reassessment of the relative effective height of spectral features.

- **Observability and noise estimation**. To provide constraints on the observability with specific telescopes and instruments, we will model the noise according to exposure time, spectral resolution, and collecting area of the instruments. The results could be applied to reflection and thermal phase curves.

- **Transmission Spectroscopy of TRAPPIST-1 c**. Future work must focus on the estimation of the number of transits for a confidence level (sigma value) needed to achieve the detection of a relative transit depth (in ppm) of the strongest CO_2 absorption spectral lines (e.g., 4.3 μm) using our Generic-GCM outputs. The estimation of the SNR associated with the number of transits and the implementation of a **noise model** are essential to estimate the detectability of the atmosphere and (or) its gaseous spectral features. These parameters should be explored for their impact in future observations, namely JWST, as observations of the TRAPPIST-1 system by JWST are already scheduled (Lincowski et al., 2018; Morley et al., 2017). Estimates on the number of transits required for atmosphere and/or spectral features detection should be placed in the context of the nominal lifetime of the instruments. The number of transits needed to detect shallow spectral features relative to the *continuum* will likely be challenged by the prohibitively large number of transits needed for detection, which might require a large amount of telescope time.

- **Emission spectroscopy of TRAPPIST-1 c**. According to (Lustig-Yaeger et al., 2019b), secondary eclipse emission spectroscopy of TRAPPIST-1 c at 6 μm would enable sounding of deeper atmospheric layers than transmission spectroscopy (at least an order of magnitude deeper pressures), opening prospects for characterising below cloud deck pressure levels, where other chemical species might be detectable. Using the Generic-GCM outputs, it might be possible to overcome the observational constraints imposed by the upper haze. By simulating the cloud variability and gaseous species present at lower levels, future synthetic emission spectra based on these outputs could actively address the challenges of recognising a Venus-like exoplanetary atmosphere with future observations.

- **Continuation of the parametric study**. This Master's work introduced a generic parametric study that provides results on the impact of mass-radius relationships and planetary rotation rate on large-scale atmospheric circulation and observables. In addition, the implementation of a simplified cloud model will allow exploring the effect of varying the surface atmospheric pressure, instellation and stellar spectra from different spectral types (e.g., mid M dwarfs).

- **Exploration of a grid of possible Venus-like atmospheres**. The diversity of planetary climates is expected to be very large. Future work will allow for a better representation of the kind of climates we can expect and will enable us to interpret better the kind of observables expected from JWST and future missions. Of particular relevance will be the ongoing work on the TRAPPIST-1 system:

  (i) TRAPPIST-1 c, to assess whether the planet has a Venus-like atmosphere and what can we tell about its composition;

  (ii) TRAPPIST-1 b, a planet with an instellation value two times that of Venus;

  (iii) TRAPPIST-1 d, a planet that will allow testing the limits of the HZ. I already have prepared simulations of TRAPPIST-1 d with a Venus-like atmosphere (prescribed cloud deck);

  (iv) The study of runaway greenhouse atmospheres in the TRAPPIST-1 planetary system as evidence from past atmospheric escape and Ocean loss.

Overall, the tools and experience developed in this Master's will be greatly relevant for future work. For instance, one planet whose atmosphere I would like to explore will be Proxima Centauri d, discovered earlier this year (2022) by a team led by our colleague *João Faria* (Institute of Astrophysics and Space Sciences at Porto) (Faria et al., 2022). Although not a transiting planet, Proxima Centauri b has an instellation value closer to Venus' than TRAPPIST-1 c, making it the *nearest* possible Venus-like exoplanet at only 1.3 pc. In parallel, the study of Venus-like exoplanets will shed light on the nature of our neighbouring planet Venus. If Venus-like planets are common, then Venus' atmosphere could be an end product of divergent atmospheric evolution from initial Earth-like conditions. On the contrary, if Venus is unique, then a scientific debate must follow to understand the possible causes of the planet's present-day Climate.

References

E. Agol, C. Dorn, S. L. Grimm, M. Turbet, E. Ducrot, L. Delrez, M. Gillon, B.-O. Demory, A. Burdanov, K. Barkaoui, et al. Refining the transit-timing and photometric analysis of TRAPPIST-1: masses, radii, densities, dynamics, and ephemerides. The planetary science journal, 2(1):1, 2021. doi:10.3847/PSJ/abd022.

Y. Alibert and W. Benz. Formation and composition of planets around very low mass stars. Astronomy & Astrophysics, 598:L5, 2017. doi:10.1051/0004-6361/201629671.

G. Anglada-Escudé, P. J. Amado, J. Barnes, Z. M. Berdiñas, R. P. Butler, G. A. Coleman, I. de La Cueva, S. Dreizler, M. Endl, B. Giesers, et al. A terrestrial planet candidate in a temperate orbit around Proxima Centauri. Nature, 536(7617):437–440, 2016. doi:10.1038/nature19106.

N. Astudillo-Defru, T. Forveille, X. Bonfils, D. Ségransan, F. Bouchy, X. Delfosse, C. Lovis, M. Mayor, F. Murgas, F. Pepe, et al. The HARPS search for southern extra-solar planets-XLI. A dozen planets around the M dwarfs GJ 3138, GJ 3323, GJ 273, GJ 628, and GJ 3293. Astronomy & Astrophysics, 602:A88, 2017. doi:10.1051/0004-6361/201630153.

P. Auclair-Desrotour, J. Laskar, S. Mathis, and A. Correia. The rotation of planets hosting atmospheric tides: from Venus to habitable super-Earths. Astronomy & Astrophysics, 603:A108, 2017. doi:10.1051/0004-6361/201628701.

I. Baraffe, D. Homeier, F. Allard, and G. Chabrier. New evolutionary models for pre-main sequence and main sequence low-mass stars down to the hydrogen-burning limit. Astronomy & Astrophysics, 577: A42, 2015. doi:10.1051/0004-6361/201425481.

J. Barstow, C. Tsang, C. Wilson, P. Irwin, F. Taylor, K. McGouldrick, P. Drossart, G. Piccioni, and S. Tellmann. Models of the global cloud structure on Venus derived from Venus Express observations. Icarus, 217(2):542–560, 2012. doi:10.1016/j.icarus.2011.05.018.

N. E. Batalha, N. K. Lewis, M. R. Line, J. Valenti, and K. Stevenson. Strategies for constraining the atmospheres of temperate terrestrial planets with JWST. The Astrophysical Journal Letters, 856(2): L34, 2018. doi:10.3847/2041-8213/aab896.

N. M. Batalha, J. F. Rowe, S. T. Bryson, T. Barclay, C. J. Burke, D. A. Caldwell, J. L. Christiansen, F. Mullally, S. E. Thompson, T. M. Brown, et al. Planetary candidates observed by Kepler. III. Analysis of the first 16 months of data. The Astrophysical Journal Supplement Series, 204(2):24, 2013. doi:10.1088/0067-0049/204/2/24.

J. L. Bean, D. S. Abbot, and E. M.-R. Kempton. A statistical comparative planetology approach to the hunt for habitable exoplanets and life beyond the Solar System. The Astrophysical Journal Letters, 841(2):L24, 2017. doi:10.3847/2041-8213/aa738a.

J. L. Bean, K. B. Stevenson, N. M. Batalha, Z. Berta-Thompson, L. Kreidberg, N. Crouzet, B. Benneke, M. R. Line, D. K. Sing, H. R. Wakeford, et al. The transiting exoplanet community early release science program for JWST. Publications of the Astronomical Society of the Pacific, 130(993):114402, 2018. doi:10.1088/1538-3873/aadbf3.

T. Bertrand and F. Forget. Observed glacier and volatile distribution on Pluto from atmosphere–topography processes. Nature, 540(7631):86–89, 2016. doi:10.1038/nature19337.

T. Bertrand and F. Forget. 3D modeling of organic haze in Pluto's atmosphere. Icarus, 287:72–86, 2017. doi:10.1016/j.icarus.2017.01.016.

T. Bertrand, F. Forget, O. White, B. Schmitt, S. Stern, H. Weaver, L. Young, K. Ennico, C. Olkin, and N. H. S. Team. Pluto's Beating Heart Regulates the Atmospheric Circulation: Results From High-Resolution and Multiyear Numerical Climate Simulations. Journal of Geophysical Research: Planets, 125(2):e2019JE006120, 2020. doi:10.1029/2019JE006120.

E. Bolmont, A.-S. Libert, J. Leconte, and F. Selsis. Habitability of planets on eccentric orbits: Limits of the mean flux approximation. Astronomy & Astrophysics, 591:A106, 2016. doi:10.1051/0004-6361/201628073.

X. Bonfils, X. Delfosse, S. Udry, T. Forveille, M. Mayor, C. Perrier, F. Bouchy, M. Gillon, C. Lovis, F. Pepe, et al. The HARPS search for southern extra-solar planets-XXXI. The M-dwarf sample. Astronomy & Astrophysics, 549:A109, 2013. doi:10.1051/0004-6361/201014704.

X. Bonfils, N. Astudillo-Defru, R. Díaz, J.-M. Almenara, T. Forveille, F. Bouchy, X. Delfosse, C. Lovis, M. Mayor, F. Murgas, et al. A temperate exo-Earth around a quiet M dwarf at 3.4 parsec. Astronomy & Astrophysics, 613:A25, 2018. doi:10.1051/0004-6361/201731973.

W. J. Borucki, D. G. Koch, G. Basri, N. Batalha, T. M. Brown, S. T. Bryson, D. Caldwell, J. Christensen-Dalsgaard, W. D. Cochran, E. DeVore, et al. Characteristics of planetary candidates observed by Kepler. II. Analysis of the first four months of data. The Astrophysical Journal, 736(1):19, 2011. doi:10.1088/0004-637X/736/1/19.

T. M. Brown. Transmission spectra as diagnostics of extrasolar giant planet atmospheres. The Astrophysical Journal, 553(2):1006, 2001. doi:10.1086/320950.

A. Burdanov, S. Lederer, M. Gillon, L. Delrez, E. Ducrot, J. de Wit, E. Jehin, A. Triaud, C. Lidman, L. Spitler, et al. Ground-based follow-up observations of TRAPPIST-1 transits in the near-infrared. Monthly Notices of the Royal Astronomical Society, 487(2):1634–1652, 2019. doi:10.1093/mnras/stz1375.

A. J. Burgasser and E. E. Mamajek. On the Age of the TRAPPIST-1 System. The Astrophysical Journal, 845(2):110, 2017. doi:10.3847/1538-4357/aa7fea.

A. Cassan, D. Kubas, J.-P. Beaulieu, M. Dominik, K. Horne, J. Greenhill, J. Wambsganss, J. Menzies, A. Williams, U. G. Jørgensen, et al. One or more bound planets per Milky Way star from microlensing observations. Nature, 481(7380):167–169, 2012. doi:10.1038/nature10684.

S. Chapman and R. S. Lindzen. Atmospheric tides: thermal and gravitational, volume 15. Springer Science & Business Media, 1969.

D. Charbonneau, T. M. Brown, R. W. Noyes, and R. L. Gilliland. Detection of an extrasolar planet atmosphere. The Astrophysical Journal, 568(1):377, 2002. doi:10.1086/338770.

B. Charnay, F. Forget, R. Wordsworth, J. Leconte, E. Millour, F. Codron, and A. Spiga. Exploring the faint young Sun problem and the possible climates of the Archean Earth with a 3-D GCM. Journal of Geophysical Research: Atmospheres, 118(18):10–414, 2013. doi:10.1002/jgrd.50808.

B. Charnay, F. Forget, G. Tobie, C. Sotin, and R. Wordsworth. Titan's past and future: 3D modeling of a pure nitrogen atmosphere and geological implications. Icarus, 241:269–279, 2014. doi:10.1016/j.icarus.2014.07.009.

B. Charnay, V. Meadows, and J. Leconte. 3D modeling of GJ1214b's atmosphere: vertical mixing driven by an anti-Hadley circulation. The Astrophysical Journal, 813(1):15, 2015. doi:10.1088/0004-637X/813/1/15.

B. Charnay, D. Blain, B. Bézard, J. Leconte, M. Turbet, and A. Falco. Formation and dynamics of water clouds on temperate sub-Neptunes: the example of K2-18b. Astronomy & Astrophysics, 646:A171, 2021. doi:10.1051/0004-6361/202039525.

R. T. Clancy, B. J. Sandor, and J. Hoge. Doppler winds mapped around the lower thermospheric terminator of Venus: 2012 solar transit observations from the James Clerk Maxwell Telescope. Icarus, 254:233–258, 2015. doi:10.1016/j.icarus.2015.03.031.

C. Cofield and T. Greicius. The 7 rocky trappist-1 planets may be made of similar stuff, 2021. URL `https://www.nasa.gov/feature/the-7-rocky-trappist-1-planets-may-be-made-of-similar-stuff`. (last accessed: 10.02.2021).

C. S. Cooper and A. P. Showman. Dynamic meteorology at the photosphere of HD 209458b. The Astrophysical Journal Letters, 629(1):L45, 2005. doi:10.1086/444354.

C. S. Cooper and A. P. Showman. Dynamics and disequilibrium carbon chemistry in hot Jupiter atmospheres, with application to HD 209458b. The Astrophysical Journal, 649(2):1048, 2006. doi:10.1086/506312.

A. C. Correia and J. Laskar. The four final rotation states of Venus. Nature, 411(6839):767–770, 2001. doi:10.1038/35081000.

A. C. Correia, B. Levrard, and J. Laskar. On the equilibrium rotation of Earth-like extra-solar planets. Astronomy & Astrophysics, 488(3):L63–L66, 2008. doi:10.1051/0004-6361:200810388.

N. B. Cowan and E. Agol. Inverting phase functions to map exoplanets. The Astrophysical Journal Letters, 678(2):L129, 2008. doi:10.1086/588553.

N. B. Cowan and E. Agol. A model for thermal phase variations of circular and eccentric exoplanets. The Astrophysical Journal, 726(2):82, 2010. doi:10.1088/0004-637X/726/2/82.

N. B. Cowan and E. Agol. The statistics of albedo and heat recirculation on hot exoplanets. The Astrophysical Journal, 729(1):54, 2011. doi:10.1088/0004-637X/729/1/54.

P. Cresswell and R. P. Nelson. On the evolution of multiple protoplanets embedded in a protostellar disc. Astronomy & Astrophysics, 450(2):833–853, 2006. doi:10.1051/0004-6361:20054551.

I. J. Crossfield. Observations of exoplanet atmospheres. Publications of the Astronomical Society of the Pacific, 127(956):941, 2015. doi:10.1086/683115.

I. J. Crossfield, B. M. Hansen, J. Harrington, J. Y.-K. Cho, D. Deming, K. Menou, and S. Seager. A new 24 μm phase curve for υ Andromedae b. The Astrophysical Journal, 723(2):1436, 2010. doi:10.1088/0004-637X/723/2/1436.

I. De Pater and J. J. Lissauer. Planetary Sciences. Cambridge University Press, 2015.

J. de Wit, H. R. Wakeford, M. Gillon, N. K. Lewis, J. A. Valenti, B.-O. Demory, A. J. Burgasser, A. Burdanov, L. Delrez, E. Jehin, et al. A combined transmission spectrum of the Earth-sized exoplanets TRAPPIST-1 b and c. Nature, 537(7618):69–72, 2016. doi:10.1038/nature18641.

J. de Wit, H. R. Wakeford, N. K. Lewis, L. Delrez, M. Gillon, F. Selsis, J. Leconte, B.-O. Demory, E. Bolmont, V. Bourrier, et al. Atmospheric reconnaissance of the habitable-zone Earth-sized planets orbiting TRAPPIST-1. Nature Astronomy, 2(3):214–219, 2018. doi:10.1038/s41550-017-0374-z.

L. Delrez, M. Gillon, A. Triaud, B.-O. Demory, J. De Wit, J. Ingalls, E. Agol, E. Bolmont, A. Burdanov, A. Burgasser, et al. Early 2017 observations of TRAPPIST-1 with Spitzer. Monthly Notices of the Royal Astronomical Society, 475(3):3577–3597, 2018. doi:10.1093/mnras/sty051.

B.-O. Demory, J. De Wit, N. Lewis, J. Fortney, A. Zsom, S. Seager, H. Knutson, K. Heng, N. Madhusudhan, M. Gillon, et al. Inference of inhomogeneous clouds in an exoplanet atmosphere. The Astrophysical Journal Letters, 776(2):L25, 2013. doi:10.1088/2041-8205/776/2/L25.

I. Dobbs-Dixon and D. Lin. Atmospheric dynamics of short-period extrasolar gas giant planets. I. Dependence of nightside temperature on opacity. The Astrophysical Journal, 673(1):513, 2008. doi:10.1086/523786.

I. Dobbs-Dixon, A. Cumming, and D. Lin. Radiative hydrodynamic simulations of HD209458b: temporal variability. The Astrophysical Journal, 710(2):1395, 2010. doi:10.1088/0004-637X/710/2/1395.

I. Dobbs-Dixon, E. Agol, and A. Burrows. The impact of circumplantary jets on transit spectra and timing offsets for hot Jupiters. The Astrophysical Journal, 751(2):87, 2012. doi:10.1088/0004-637X/751/2/87.

A. R. Dobrovolskis. Insolation patterns on synchronous exoplanets with obliquity. Icarus, 204(1):1–10, 2009. doi:10.1016/j.icarus.2009.06.007.

S. Dreizler, S. Jeffers, E. Rodríguez, M. Zechmeister, J. Barnes, C. Haswell, G. Coleman, S. Lalitha, D. Hidalgo Soto, J. Strachan, et al. RedDots: a temperate 1.5 Earth-mass planet candidate in a compact multiterrestrial planet system around GJ 1061. Monthly Notices of the Royal Astronomical Society, 493(1):536–550, 2020. doi:10.1093/mnras/staa248.

E. Ducrot, M. Sestovic, B. Morris, M. Gillon, A. Triaud, J. De Wit, D. Thimmarayappa, E. Agol, Y. Almleaky, A. Burdanov, et al. The 0.8–4.5 μm broadband transmission spectra of TRAPPIST-1 planets. The Astronomical Journal, 156(5):218, 2018. doi:10.3847/1538-3881/aade94.

E. Ducrot, M. Gillon, L. Delrez, E. Agol, P. Rimmer, M. Turbet, M. Günther, B.-O. Demory, A. Triaud, E. Bolmont, et al. TRAPPIST-1: Global results of the Spitzer Exploration Science Program Red Worlds. Astronomy & Astrophysics, 640:A112, 2020. doi:10.1051/0004-6361/201937392.

T. Encrenaz. Infrared spectroscopy of exoplanets: observational constraints. Philosophical Transactions of the Royal Society A: Mathematical, Physical and Engineering Sciences, 372(2014):20130083, 2014. doi:10.1098/rsta.2013.0083.

V. Eymet, C. Coustet, and B. Piaud. kspectrum: An open-source code for high-resolution molecular absorption spectra production. In Journal of Physics: Conference Series, volume 676, page 012005. IOP Publishing, 2016. doi:10.1088/1742-6596/676/1/012005.

J. Faria, A. S. Mascareño, P. Figueira, A. Silva, M. Damasso, O. Demangeon, F. Pepe, N. Santos, R. Rebolo, S. Cristiani, et al. A candidate short-period sub-Earth orbiting Proxima Centauri. Astronomy & Astrophysics, 658:A115, 2022. doi:10.1051/0004-6361/202142337.

T. J. Fauchez, M. Turbet, G. L. Villanueva, E. T. Wolf, G. Arney, R. K. Kopparapu, A. Lincowski, A. Mandell, J. de Wit, D. Pidhorodetska, et al. Impact of clouds and hazes on the simulated JWST transmission spectra of habitable zone planets in the TRAPPIST-1 system. The Astrophysical Journal, 887(2):194, 2019. doi:10.3847/1538-4357/ab5862.

T. J. Fauchez, M. Turbet, D. E. Sergeev, N. J. Mayne, A. Spiga, L. Sohl, P. Saxena, R. Deitrick, G. Gilli, S. D. Domagal-Goldman, et al. TRAPPIST Habitable Atmosphere Intercomparison (THAI) Workshop Report. The Planetary Science Journal, 2(3):106, 2021. doi:10.3847/PSJ/abf4df.

F. Forget and J. Leconte. Possible climates on terrestrial exoplanets. Philosophical Transactions of the Royal Society A: Mathematical, Physical and Engineering Sciences, 372(2014):20130084, 2014. doi:10.1098/rsta.2013.0084.

F. Forget, F. Hourdin, R. Fournier, C. Hourdin, O. Talagrand, M. Collins, S. R. Lewis, P. L. Read, and J.-P. Huot. Improved general circulation models of the Martian atmosphere from the surface to above 80 km. Journal of Geophysical Research: Planets, 104(E10):24155–24175, 1999. doi:10.1029/1999JE001025.

F. Forget, R. Wordsworth, E. Millour, J.-B. Madeleine, L. Kerber, J. Leconte, E. Marcq, and R. M. Haberle. 3D modelling of the early martian climate under a denser CO2 atmosphere: Temperatures and CO2 ice clouds. Icarus, 222(1):81–99, 2013. doi:10.1016/j.icarus.2012.10.019.

F. Forget, T. Bertrand, M. Vangvichith, J. Leconte, E. Millour, and E. Lellouch. A post-new horizons global climate model of Pluto including the N2, CH4 and CO cycles. Icarus, 287:54–71, 2017. doi:10.1016/j.icarus.2016.11.038.

Q. Fu and K. Liou. On the correlated k-distribution method for radiative transfer in nonhomogeneous atmospheres. Journal of Atmospheric Sciences, 49(22):2139–2156, 1992. doi:10.1175/1520-0469(1992)049<2139:OTCDMF>2.0.CO;2.

C. Gable, H. Betz, and S. Maron. Phase Equilibria of the System Sulfur Trioxide-Water1. Journal of the American Chemical Society, 72(4):1445–1448, 1950. doi:10.1021/ja01160a005.

P. Gao, R. Hu, T. D. Robinson, C. Li, and Y. L. Yung. Stability of CO2 atmospheres on desiccated M dwarf exoplanets. The Astrophysical Journal, 806(2):249, 2015. doi:10.1088/0004-637X/806/2/249.

I. Garate-Lopez and S. Lebonnois. Latitudinal variation of clouds' structure responsible for Venus' cold collar. Icarus, 314:1–11, 2018. doi:10.1016/j.icarus.2018.05.011.

P. J. Gierasch. Meridional circulation and the maintenance of the Venus atmospheric rotation. Journal of Atmospheric Sciences, 32(6):1038–1044, 1975. doi:10.1175/1520-0469(1975)032<1038:MCATMO>2.0.CO;2.

M. Gillon, E. Jehin, P. Magain, V. Chantry, D. Hutsemékers, J. Manfroid, D. Queloz, and S. Udry. TRAPPIST: a robotic telescope dedicated to the study of planetary systems. In EPJ Web of Conferences, volume 11, page 06002. EDP Sciences, 2011. doi:10.1051/epjconf/20101106002.

M. Gillon, E. Jehin, A. Fumel, P. Magain, and D. Queloz. TRAPPIST-UCDTS: A prototype search for habitable planets transiting ultra-cool stars. In EPJ Web of Conferences, volume 47, page 03001. EDP Sciences, 2013. doi:10.1051/epjconf/20134703001.

M. Gillon, E. Jehin, S. M. Lederer, L. Delrez, J. de Wit, A. Burdanov, V. Van Grootel, A. J. Burgasser, A. H. Triaud, C. Opitom, et al. Temperate Earth-sized planets transiting a nearby ultracool dwarf star. Nature, 533(7602):221–224, 2016. doi:10.1038/nature17448.

M. Gillon, A. H. Triaud, B.-O. Demory, E. Jehin, E. Agol, K. M. Deck, S. M. Lederer, J. De Wit, A. Burdanov, J. G. Ingalls, et al. Seven temperate terrestrial planets around the nearby ultracool dwarf star TRAPPIST-1. Nature, 542(7642):456–460, 2017. doi:10.1038/nature21360.

S. L. Grimm, B.-O. Demory, M. Gillon, C. Dorn, E. Agol, A. Burdanov, L. Delrez, M. Sestovic, A. H. Triaud, M. Turbet, et al. The nature of the TRAPPIST-1 exoplanets. Astronomy & Astrophysics, 613: A68, 2018. doi:10.1051/0004-6361/201732233.

M. Hammond and R. T. Pierrehumbert. Wave-mean flow interactions in the atmospheric circulation of tidally locked planets. The Astrophysical Journal, 869(1):65, 2018. doi:10.3847/1538-4357/aaec03.

R. Haus, D. Kappel, and G. Arnold. Self-consistent retrieval of temperature profiles and cloud structure in the northern hemisphere of Venus using VIRTIS/VEX and PMV/VENERA-15 radiation measurements. Planetary and Space Science, 89:77–101, 2013. doi:10.1016/j.pss.2013.09.020.

K. Heng. On the existence of shocks in irradiated exoplanetary atmospheres. The Astrophysical Journal Letters, 761(1):L1, 2012. doi:10.1088/2041-8205/761/1/L1.

K. Heng and B.-O. Demory. Understanding trends associated with clouds in irradiated exoplanets. The Astrophysical Journal, 777(2):100, 2013. doi:10.1088/0004-637X/777/2/100.

K. Heng and A. P. Showman. Atmospheric dynamics of hot exoplanets. Annual Review of Earth and Planetary Sciences, 43:509–540, 2015. doi:10.1146/annurev-earth-060614-105146.

K. Heng, D. M. Frierson, and P. J. Phillipps. Atmospheric circulation of tidally locked exoplanets: II. Dual-band radiative transfer and convective adjustment. Monthly Notices of the Royal Astronomical Society, 418(4):2669–2696, 2011a. doi:10.1111/j.1365-2966.2011.19658.x.

K. Heng, K. Menou, and P. J. Phillipps. Atmospheric circulation of tidally locked exoplanets: a suite of benchmark tests for dynamical solvers. Monthly Notices of the Royal Astronomical Society, 413(4): 2380–2402, 2011b. doi:10.1111/j.1365-2966.2011.18315.x.

F. Hourdin, I. Musat, S. Bony, P. Braconnot, F. Codron, J.-L. Dufresne, L. Fairhead, M.-A. Filiberti, P. Friedlingstein, J.-Y. Grandpeix, et al. The LMDZ4 general circulation model: climate performance and sensitivity to parametrized physics with emphasis on tropical convection. Climate Dynamics, 27 (7):787–813, 2006. doi:10.1007/s00382-006-0158-0.

A. W. Howard, G. W. Marcy, J. A. Johnson, D. A. Fischer, J. T. Wright, H. Isaacson, J. A. Valenti, J. Anderson, D. N. Lin, and S. Ida. The occurrence and mass distribution of close-in super-Earths, Neptunes, and Jupiters. Science, 330(6004):653–655, 2010. doi:10.1126/science.1194854.

R. Hu, L. Peterson, and E. T. Wolf. O2-and CO-rich atmospheres for potentially habitable environments on TRAPPIST-1 planets. The Astrophysical Journal, 888(2):122, 2020. doi:10.3847/1538-4357/ab5f07.

W. Hubbard, J. Fortney, J. Lunine, A. Burrows, D. Sudarsky, and P. Pinto. Theory of extrasolar giant planet transits. The Astrophysical Journal, 560(1):413, 2001. doi:10.1086/322490.

P. Hut. Stability of tidal equilibrium. Astronomy and Astrophysics, 92:167–170, 1980. URL `https://articles.adsabs.harvard.edu/pdf/1980A%26A....92..167H`.

N. Ignatiev, D. Titov, G. Piccioni, P. Drossart, W. Markiewicz, V. Cottini, T. Roatsch, M. Almeida, and N. Manoel. Altimetry of the Venus cloud tops from the Venus Express observations. Journal of Geophysical Research: Planets, 114(E9), 2009. doi:10.1029/2008JE003320.

A. P. Ingersoll and A. R. Dobrovolskis. Venus' rotation and atmospheric tides. Nature, 275(5675):37–38, 1978. doi:10.1038/275037a0.

L. Kaltenegger and W. A. Traub. Transits of Earth-like planets. The Astrophysical Journal, 698(1):519, 2009. doi:10.1088/0004-637X/698/1/519.

S. R. Kane and K. von Braun. Constraining orbital parameters through planetary transit monitoring. The Astrophysical Journal, 689(1):492, 2008. doi:10.1086/592381.

S. R. Kane, T. Barclay, and D. M. Gelino. A potential super-Venus in the Kepler-69 system. The Astrophysical Journal Letters, 770(2):L20, 2013. doi:10.1088/2041-8205/770/2/L20.

S. R. Kane, R. K. Kopparapu, and S. D. Domagal-Goldman. On the frequency of potential Venus analogs from Kepler data. The Astrophysical Journal Letters, 794(1):L5, 2014. doi:10.1088/2041-8205/794/1/L5.

J. F. Kasting, D. P. Whitmire, and R. T. Reynolds. Habitable zones around main sequence stars. Icarus, 101(1):108–128, 1993. doi:10.1006/icar.1993.1010.

J. F. Kasting, R. Kopparapu, R. M. Ramirez, and C. E. Harman. Remote life-detection criteria, habitable zone boundaries, and the frequency of Earth-like planets around M and late K stars. Proceedings of the National Academy of Sciences, 111(35):12641–12646, 2014. doi:10.1073/pnas.1309107110.

T. Kataria, A. P. Showman, N. K. Lewis, J. J. Fortney, M. S. Marley, and R. S. Freedman. Three-dimensional atmospheric circulation of hot Jupiters on highly eccentric orbits. The Astrophysical Journal, 767(1):76, 2013. doi:10.1088/0004-637X/767/1/76.

G. Keating, J. Bertaux, S. Bougher, R. Dickinson, T. E. Cravens, A. F. Nagy, A. Hedin, V. Krasnopolsky, J. Nicholson III, L. Paxton, et al. Models of Venus neutral upper atmosphere: Structure and composition. Advances in Space Research, 5(11):117–171, 1985. doi:10.1016/0273-1177(85)90200-5.

E. M.-R. Kempton, J. L. Bean, D. R. Louie, D. Deming, D. D. Koll, M. Mansfield, J. L. Christiansen, M. López-Morales, M. R. Swain, R. T. Zellem, et al. A framework for prioritizing the TESS planetary candidates most amenable to atmospheric characterization. Publications of the Astronomical Society of the Pacific, 130(993):114401, 2018. doi:10.1088/1538-3873/aadf6f.

L. Kerber, F. Forget, and R. Wordsworth. Sulfur in the early martian atmosphere revisited: Experiments with a 3-D Global Climate Model. Icarus, 261:133–148, 2015. doi:10.1016/j.icarus.2015.08.011.

H. A. Knutson, D. Charbonneau, L. E. Allen, J. J. Fortney, E. Agol, N. B. Cowan, A. P. Showman, C. S. Cooper, and S. T. Megeath. A map of the day–night contrast of the extrasolar planet HD 189733b. Nature, 447(7141):183–186, 2007. doi:10.1038/nature05782.

H. A. Knutson, D. Charbonneau, N. B. Cowan, J. J. Fortney, A. P. Showman, E. Agol, G. W. Henry, M. E. Everett, and L. E. Allen. Multiwavelength constraints on the day-night circulation patterns of HD 189733b. The Astrophysical Journal, 690(1):822, 2008. doi:10.1088/0004-637X/690/1/822.

H. A. Knutson, N. Lewis, J. J. Fortney, A. Burrows, A. P. Showman, N. B. Cowan, E. Agol, S. Aigrain, D. Charbonneau, D. Deming, et al. 3.6 and 4.5 μm phase curves and evidence for non-equilibrium chemistry in the atmosphere of extrasolar planet HD 189733b. The Astrophysical Journal, 754(1):22, 2012. doi:10.1088/0004-637X/754/1/22.

H. A. Knutson, B. Benneke, D. Deming, and D. Homeier. A featureless transmission spectrum for the Neptune-mass exoplanet GJ 436b. Nature, 505(7481):66–68, 2014. doi:10.1038/nature12887.

R. Kopparapu, E. T. Wolf, G. Arney, N. E. Batalha, J. Haqq-Misra, S. L. Grimm, and K. Heng. Habitable moist atmospheres on terrestrial planets near the inner edge of the habitable zone around M dwarfs. The Astrophysical Journal, 845(1):5, 2017. doi:10.3847/1538-4357/aa7cf9.

R. K. Kopparapu. A revised estimate of the occurrence rate of terrestrial planets in the habitable zones around Kepler M-dwarfs. The Astrophysical Journal Letters, 767(1):L8, 2013b. doi:10.1088/2041-8205/767/1/L8.

R. K. Kopparapu, R. Ramirez, J. F. Kasting, V. Eymet, T. D. Robinson, S. Mahadevan, R. C. Terrien, S. Domagal-Goldman, V. Meadows, and R. Deshpande. Habitable zones around main-sequence stars: new estimates. The Astrophysical Journal, 765(2):131, 2013a. doi:10.1088/0004-637X/765/2/131.

L. Kreidberg, J. L. Bean, J.-M. Désert, B. Benneke, D. Deming, K. B. Stevenson, S. Seager, Z. Berta-Thompson, A. Seifahrt, and D. Homeier. Clouds in the atmosphere of the super-Earth exoplanet GJ 1214b. Nature, 505(7481):69–72, 2014. doi:10.1038/nature12888.

L. Kreidberg, M. R. Line, J. L. Bean, K. B. Stevenson, J.-M. Désert, N. Madhusudhan, J. J. Fortney, J. K. Barstow, G. W. Henry, M. H. Williamson, et al. A detection of water in the transmission spectrum of the hot Jupiter WASP-12b and implications for its atmospheric composition. The Astrophysical Journal, 814(1):66, 2015. doi:10.1088/0004-637X/814/1/66.

L. Kreidberg, E. Agol, E. Bolmont, M. Gillon, R. Hu, D. Koll, A. Mandell, V. S. Meadows, C. Morley, L. Schaefer, et al. Hot Take on a Cool World: Does Trappist-1c Have an Atmosphere? JWST Proposal. Cycle 1, page 2304, 2021. URL `https://www.stsci.edu/jwst/phase2-public/2304.pdf`.

S. Lebonnois, F. Hourdin, V. Eymet, A. Crespin, R. Fournier, and F. Forget. Superrotation of Venus' atmosphere analyzed with a full general circulation model. Journal of Geophysical Research: Planets, 115(E6), 2010. doi:10.1029/2009JE003458.

S. Lebonnois, J. Burgalat, P. Rannou, and B. Charnay. Titan global climate model: A new 3-dimensional version of the IPSL Titan GCM. Icarus, 218(1):707–722, 2012. doi:10.1016/J.ICARUS.2011.11.032.

S. Lebonnois, V. Eymet, C. Lee, and J. Vatant d'Ollone. Analysis of the radiative budget of the Venusian atmosphere based on infrared Net Exchange Rate formalism. Journal of Geophysical Research: Planets, 120(6):1186–1200, 2015. doi:10.1002/2015JE004794.

J. Leconte, G. Chabrier, I. Baraffe, and B. Levrard. Is tidal heating sufficient to explain bloated exoplanets? Consistent calculations accounting for finite initial eccentricity. Astronomy & Astrophysics, 516:A64, 2010. doi:10.1051/0004-6361/201014337.

J. Leconte, F. Forget, B. Charnay, R. Wordsworth, F. Selsis, E. Millour, and A. Spiga. 3D climate modeling of close-in land planets: circulation patterns, climate moist bistability, and habitability. Astronomy & Astrophysics, 554:A69, 2013a. doi:10.1051/0004-6361/201321042.

J. Leconte, F. Forget, B. Charnay, R. Wordsworth, and A. Pottier. Increased insolation threshold for runaway greenhouse processes on Earth-like planets. Nature, 504(7479):268–271, 2013b. doi:10.1038/nature12827.

J. Leconte, F. Forget, and H. Lammer. On the (anticipated) diversity of terrestrial planet atmospheres. Experimental Astronomy, 40(2-3):449–467, 2015a. doi:10.1007/s10686-014-9403-4.

J. Leconte, H. Wu, K. Menou, and N. Murray. Asynchronous rotation of Earth-mass planets in the habitable zone of lower-mass stars. Science, 347(6222):632–635, 2015b. doi:10.1126/science.1258686.

Y. J. Lee, A. G. Muñoz, T. Imamura, M. Yamada, T. Satoh, A. Yamazaki, and S. Watanabe. Brightness modulations of our nearest terrestrial planet Venus reveal atmospheric super-rotation rather than surface features. Nature communications, 11(1):1–8, 2020. doi:10.1038/s41467-020-19385-6.

N. K. Lewis, A. P. Showman, J. J. Fortney, M. S. Marley, R. S. Freedman, and K. Lodders. Atmospheric circulation of eccentric hot Neptune GJ436b. The Astrophysical Journal, 720(1):344, 2010. doi:10.1088/0004-637X/720/1/344.

N. K. Lewis, H. A. Knutson, A. P. Showman, N. B. Cowan, G. Laughlin, A. Burrows, D. Deming, J. R. Crepp, K. J. Mighell, E. Agol, et al. Orbital phase variations of the eccentric giant planet HAT-P-2b. The Astrophysical Journal, 766(2):95, 2013. doi:10.1088/0004-637X/766/2/95.

S. S. Limaye and M. Rengel. Atmospheric circulation and dynamics. In Towards understanding the climate of Venus, pages 55–70. Springer, 2013. doi:10.1007/978-1-4614-5064-1_5.

S. S. Limaye, D. Grassi, A. Mahieux, A. Migliorini, S. Tellmann, and D. Titov. Venus atmospheric thermal structure and radiative balance. Space Science Reviews, 214(5):1–71, 2018. doi:10.1007/s11214-018-0525-2.

A. P. Lincowski, V. S. Meadows, D. Crisp, T. D. Robinson, R. Luger, J. Lustig-Yaeger, and G. N. Arney. Evolved climates and observational discriminants for the TRAPPIST-1 planetary system. The Astrophysical Journal, 867(1):76, 2018. doi:10.3847/1538-4357/aae36a.

A. P. Lincowski, J. Lustig-Yaeger, and V. S. Meadows. Observing isotopologue bands in terrestrial exoplanet atmospheres with the James Webb Space Telescope: implications for identifying past atmospheric and ocean loss. The Astronomical Journal, 158(1):26, 2019. doi:10.3847/1538-3881/ab2385.

J. J. Lissauer, G. W. Marcy, S. T. Bryson, J. F. Rowe, D. Jontof-Hutter, E. Agol, W. J. Borucki, J. A. Carter, E. B. Ford, R. L. Gilliland, et al. Validation of Kepler's multiple planet candidates. II. Refined statistical framework and descriptions of systems of special interest. The Astrophysical Journal, 784 (1):44, 2014. doi:10.1088/0004-637X/784/1/44.

R. Luger and R. Barnes. Extreme water loss and abiotic O2 buildup on planets throughout the habitable zones of M dwarfs. Astrobiology, 15(2):119–143, 2015. doi:10.1089/ast.2014.1231.

R. Luger, M. Sestovic, E. Kruse, S. L. Grimm, B.-O. Demory, E. Agol, E. Bolmont, D. Fabrycky, C. S. Fernandes, V. Van Grootel, et al. A seven-planet resonant chain in TRAPPIST-1. Nature Astronomy, 1(6):1–8, 2017a. doi:10.1038/s41550-017-0129.

J. Lustig-Yaeger, V. S. Meadows, and A. P. Lincowski. The detectability and characterization of the TRAPPIST-1 exoplanet atmospheres with JWST. The Astronomical Journal, 158(1):27, 2019a. doi:10.3847/1538-3881/ab21e0.

J. Lustig-Yaeger, V. S. Meadows, and A. P. Lincowski. A mirage of the cosmic shoreline: Venus-like clouds as a statistical false positive for exoplanet atmospheric erosion. The Astrophysical Journal Letters, 887(1):L11, 2019b. doi:10.3847/2041-8213/ab5965.

S. J. Mackwell, A. A. Simon-Miller, J. W. Harder, and M. A. Bullock. Comparative climatology of terrestrial planets. University of Arizona Press, 2014.

V. V. Makarov, C. Berghea, and M. Efroimsky. Dynamical evolution and spin–orbit resonances of potentially habitable exoplanets: the case of GJ 581d. The Astrophysical Journal, 761(2):83, 2012. doi:10.1088/0004-637X/761/2/83.

E. Mamajek, A. Prsa, G. Torres, P. Harmanec, M. Asplund, P. Bennett, N. Capitaine, J. Christensen-Dalsgaard, E. Depagne, W. Folkner, et al. IAU 2015 resolution B3 on recommended nominal conversion constants for selected solar and planetary properties. 2015. doi:10.48550/arXiv.1510.07674.

G. W. Marcy, R. P. Butler, E. Williams, L. Bildsten, J. R. Graham, A. M. Ghez, and J. G. Jernigan. The planet around 51 Pegasi. The Astrophysical Journal, 481(2):926, 1997. doi:10.1086/304088.

N. Mayne, I. Baraffe, D. M. Acreman, C. Smith, N. Wood, D. S. Amundsen, J. Thuburn, and D. R. Jackson. Using the UM dynamical cores to reproduce idealised 3-D flows. Geoscientific Model Development, 7(6):3059–3087, 2014. doi:10.5194/gmd-7-3059-2014.

M. Mayor and D. Queloz. A Jupiter-mass companion to a solar-type star. Nature, 378(6555):355–359, 1995. doi:10.1038/378355a0.

K. McGouldrick, O. B. Toon, and D. H. Grinspoon. Sulfuric acid aerosols in the atmospheres of the terrestrial planets. Planetary and Space Science, 59(10):934–941, 2011. doi:10.1016/j.pss.2010.05.020.

V. S. Meadows. Reflections on O2 as a biosignature in exoplanetary atmospheres. Astrobiology, 17(10): 1022–1052, 2017. doi:10.1089/ast.2016.1578.

S. M. Mills, D. C. Fabrycky, C. Migaszewski, E. B. Ford, E. Petigura, and H. Isaacson. A resonant chain of four transiting, sub-Neptune planets. Nature, 533(7604):509–512, 2016. doi:10.1038/nature17445.

J. L. Mitchell and J. M. Lora. The climate of Titan. Annual Review of Earth and Planetary Sciences, 44: 353–380, 2016. doi:10.1146/annurev-earth-060115-012428.

C. V. Morley, L. Kreidberg, Z. Rustamkulov, T. Robinson, and J. J. Fortney. Observing the atmospheres of known temperate Earth-sized planets with JWST. The Astrophysical Journal, 850(2):121, 2017. doi:10.3847/1538-4357/aa927b.

NASA. Nasa exoplanet archive, 2022a. URL `https://exoplanetarchive.ipac.caltech.edu/`.

O. Nobel Prize. Press release: The nobel prize in physics 2019, 2019. URL `https://www.nobelprize.org/prizes/physics/2019/press-release/`.

C. Ostberg and S. R. Kane. Predicting the yield of potential venus analogs from TESS and their potential for atmospheric characterization. The Astronomical Journal, 158(5):195, 2019. doi:10.3847/1538-3881/ab44b0.

V. Parmentier and I. J. Crossfield. Exoplanet phase curves: Observations and theory. Handbook of exoplanets, 116, 2018. doi:10.1007/978-3-319-55333-7_116.

J. P. Peixoto and A. H. Oort. Physics of Climate. 1992.

D. Perez-Becker and A. P. Showman. Atmospheric heat redistribution on hot Jupiters. The Astrophysical Journal, 776(2):134, 2013. doi:10.1088/0004-637X/776/2/134.

R. Perna, K. Heng, and F. Pont. The effects of irradiation on hot Jovian atmospheres: Heat redistribution and energy dissipation. The Astrophysical Journal, 751(1):59, 2012. doi:10.1088/0004-637X/751/1/59.

R. T. Pierrehumbert and F. Ding. Dynamics of atmospheres with a non-dilute condensible component. Proceedings of the Royal Society A: Mathematical, Physical and Engineering Sciences, 472(2190): 20160107, 2016. doi:10.1098/rspa.2016.0107.

R. T. Pierrehumbert and M. Hammond. Atmospheric circulation of tide-locked exoplanets. Annual Review of Fluid Mechanics, 51:275–303, 2019. doi:10.1146/annurev-fluid-010518-040516.

J. B. Pollack, J. B. Dalton, D. Grinspoon, R. B. Wattson, R. Freedman, D. Crisp, D. A. Allen, B. Bezard, C. DeBergh, L. P. Giver, et al. Near-infrared light from Venus' nightside: A spectroscopic analysis. Icarus, 103(1):1–42, 1993. doi:10.1006/icar.1993.1055.

F. Pont, H. Knutson, R. Gilliland, C. Moutou, and D. Charbonneau. Detection of atmospheric haze on an extrasolar planet: the 0.55–1.05 μm transmission spectrum of HD 189733b with the Hubble Space Telescope. Monthly Notices of the Royal Astronomical Society, 385(1):109–118, 2008. doi:10.1111/j.1365-2966.2008.12852.x.

E. Rauscher and K. Menou. Three-dimensional modeling of hot Jupiter atmospheric flows. The Astrophysical Journal, 714(2):1334, 2010. doi:10.1088/0004-637X/714/2/1334.

E. Rauscher and K. Menou. A General Circulation Model for Gaseous Exoplanets with Double-gray Radiative Transfer. The Astrophysical Journal, 750(2):96, 2012. doi:10.1088/0004-637X/750/2/96.

S. N. Raymond, R. Barnes, and A. M. Mandell. Observable consequences of planet formation models in systems with close-in terrestrial planets. Monthly Notices of the Royal Astronomical Society, 384(2): 663–674, 2008. doi:10.1111/j.1365-2966.2007.12712.x.

P. Read. Super-rotation and diffusion of axial angular momentum: II. A review of quasi-axisymmetric models of planetary atmospheres. Quarterly Journal of the Royal Meteorological Society, 112(471): 253–272, 1986. doi:10.1002/qj.49711247114.

P. Read. Dynamics and circulation regimes of terrestrial planets. Planetary and Space Science, 59(10): 900–914, 2011. doi:10.1016/j.pss.2010.04.024.

P. L. Read and S. Lebonnois. Superrotation on Venus, on Titan, and elsewhere. Annual Review of Earth and Planetary Sciences, 46:175–202, 2018. doi:10.1146/annurev-earth-082517-010137.

I. Ribas, E. Bolmont, F. Selsis, A. Reiners, J. Leconte, S. N. Raymond, S. G. Engle, E. F. Guinan, J. Morin, M. Turbet, et al. The habitability of Proxima Centauri b-I. Irradiation, rotation and volatile inventory from formation to the present. Astronomy & Astrophysics, 596:A111, 2016. doi:10.1051/0004-6361/201629576.

C. Richard, I. E. Gordon, L. S. Rothman, M. Abel, L. Frommhold, M. Gustafsson, J.-M. Hartmann, C. Hermans, W. J. Lafferty, G. S. Orton, et al. New section of the HITRAN database: Collision-induced absorption (CIA). Journal of Quantitative Spectroscopy and Radiative Transfer, 113(11): 1276–1285, 2012. doi:10.1016/j.jqsrt.2011.11.004.

L. S. Rothman, I. E. Gordon, Y. Babikov, A. Barbe, D. C. Benner, P. F. Bernath, M. Birk, L. Bizzocchi, V. Boudon, L. R. Brown, et al. The HITRAN2012 molecular spectroscopic database. Journal of Quantitative Spectroscopy and Radiative Transfer, 130:4–50, 2013. doi:10.1016/j.jqsrt.2013.07.002.

J. F. Rowe, S. T. Bryson, G. W. Marcy, J. J. Lissauer, D. Jontof-Hutter, F. Mullally, R. L. Gilliland, H. Issacson, E. Ford, S. B. Howell, et al. Validation of Kepler's multiple planet candidates. III. Light curve analysis and announcement of hundreds of new multi-planet systems. The Astrophysical Journal, 784(1):45, 2014. doi:10.1088/0004-637X/784/1/45.

F. Sainsbury-Martinez, P. Wang, S. Fromang, P. Tremblin, T. Dubos, Y. Meurdesoif, A. Spiga, J. Leconte, I. Baraffe, G. Chabrier, et al. Idealised simulations of the deep atmosphere of hot Jupiters-Deep, hot adiabats as a robust solution to the radius inflation problem. Astronomy & Astrophysics, 632:A114, 2019. doi:10.1051/0004-6361/201936445.

A. Sánchez-López, F. J. Alonso-Floriano, M. López-Puertas, I. A. Snellen, B. Funke, E. Nagel, F. Bauer, P. J. Amado, J. Caballero, S. Czesla, et al. Water vapor detection in the transmission spectra of HD 209458 b with the CARMENES NIR channel. Astronomy & Astrophysics, 630:A53, 2019. doi:10.1051/0004-6361/201936084.

S. Seager and D. Sasselov. Theoretical transmission spectra during extrasolar giant planet transits. The Astrophysical Journal, 537(2):916, 2000. doi:10.1086/309088.

A. Seiff, J. Schofield, A. Kliore, F. Taylor, S. Limaye, H. Revercomb, L. Sromovsky, V. Kerzhanovich, V. Moroz, and M. Y. Marov. Models of the structure of the atmosphere of Venus from the surface to 100 kilometers altitude. Advances in Space Research, 5(11):3–58, 1985. doi:10.1016/0273-1177(85)90197-8.

F. Selsis, J. F. Kasting, B. Levrard, J. Paillet, I. Ribas, and X. Delfosse. Habitable planets around the star Gliese 581? Astronomy & Astrophysics, 476(3):1373–1387, 2007. doi:10.1051/0004-6361:20078091.

A. Showman and T. Guillot. Atmospheric circulation and tides of "51 Pegasus b-like" planets. Astronomy & Astrophysics, 385(1):166–180, 2002. doi:10.1051/0004-6361:20020101.

A. P. Showman and L. M. Polvani. The Matsuno-Gill model and equatorial superrotation. Geophysical Research Letters, 37(18), 2010. doi:10.1029/2010GL044343.

A. P. Showman and L. M. Polvani. Equatorial superrotation on tidally locked exoplanets. The Astrophysical Journal, 738(1):71, 2011. doi:10.1088/0004-637X/738/1/71.

A. P. Showman, C. S. Cooper, J. J. Fortney, and M. S. Marley. Atmospheric circulation of hot Jupiters: Three-dimensional circulation models of HD 209458b and HD 189733b with simplified forcing. The Astrophysical Journal, 682(1):559, 2008. doi:10.1086/589325.

A. P. Showman, J. J. Fortney, Y. Lian, M. S. Marley, R. S. Freedman, H. A. Knutson, and D. Charbonneau. Atmospheric circulation of hot Jupiters: Coupled radiative-dynamical general circulation model simulations of HD 189733b and HD 209458b. The Astrophysical Journal, 699 (1):564, 2009. doi:10.1088/0004-637X/699/1/564.

A. P. Showman, R. D. Wordsworth, T. M. Merlis, and Y. Kaspi. Atmospheric circulation of terrestrial exoplanets. Comparative climatology of terrestrial planets, 1:277–326, 2013. doi:10.2458/azu_uapress_9780816530595-ch12.

A. Stolzenbach. Etude de la photochimie de Vénus à l'aide d'un modèle de circulation générale. PhD Thesis: Paris 6, 2016. URL `https://tel.archives-ouvertes.fr/tel-01415771`.

M. R. Swain, G. Vasisht, and G. Tinetti. The presence of methane in the atmosphere of an extrasolar planet. Nature, 452(7185):329–331, 2008. doi:10.1038/nature06823.

J. C. Tarter, P. R. Backus, R. L. Mancinelli, J. M. Aurnou, D. E. Backman, G. S. Basri, A. P. Boss, A. Clarke, D. Deming, L. R. Doyle, et al. A reappraisal of the habitability of planets around M dwarf stars. Astrobiology, 7(1):30–65, 2007. doi:10.1089/ast.2006.0124.

F. W. Taylor, H. Svedhem, and J. W. Head. Venus: the atmosphere, climate, surface, interior and near-space environment of an Earth-like planet. Space Science Reviews, 214(1):1–36, 2018. doi:10.1007/s11214-018-0467-8.

S. Tellmann, M. Pätzold, B. Häusler, M. K. Bird, and G. L. Tyler. Structure of the Venus neutral atmosphere as observed by the Radio Science experiment VeRa on Venus Express. Journal of Geophysical Research: Planets, 114(E9), 2009. doi:10.1029/2008JE003204.

C. Terquem and J. C. Papaloizou. Migration and the formation of systems of hot super-Earths and Neptunes. The Astrophysical Journal, 654(2):1110, 2007. doi:10.1086/509497.

G. Tinetti, A. Vidal-Madjar, M.-C. Liang, J.-P. Beaulieu, Y. Yung, S. Carey, R. J. Barber, J. Tennyson, I. Ribas, N. Allard, et al. Water vapour in the atmosphere of a transiting extrasolar planet. Nature, 448 (7150):169–171, 2007. doi:10.1038/nature06002.

D. V. Titov, N. I. Ignatiev, K. McGouldrick, V. Wilquet, and C. F. Wilson. Clouds and hazes of Venus. Space Science Reviews, 214(8):1–61, 2018. doi:10.1007/s11214-018-0552-z.

S.-M. Tsai, I. Dobbs-Dixon, and P.-G. Gu. Three-dimensional structures of equatorial waves and the resulting super-rotation in the atmosphere of a tidally locked hot Jupiter. The Astrophysical Journal, 793(2):141, 2014. doi:10.1088/0004-637X/793/2/141.

A. Tsiaras, I. P. Waldmann, G. Tinetti, J. Tennyson, and S. N. Yurchenko. Water vapour in the atmosphere of the habitable-zone eight-Earth-mass planet K2-18 b. Nature Astronomy, 3(12):1086–1091, 2019. doi:10.1038/s41550-019-0878-9.

M. Turbet. Habitability of planets using numerical climate models. Application to extrasolar planets and early Mars. PhD Thesis: Sorbonne Université, 2018b. URL `https://tel.archives-ouvertes.fr/tel-02024621`.

M. Turbet, J. Leconte, F. Selsis, E. Bolmont, F. Forget, I. Ribas, S. N. Raymond, and G. Anglada-Escudé. The habitability of Proxima Centauri b-II. Possible climates and observability. Astronomy & Astrophysics, 596:A112, 2016. doi:10.1051/0004-6361/201629577.

M. Turbet, F. Forget, J. W. Head, and R. Wordsworth. 3D modelling of the climatic impact of outflow channel formation events on early Mars. Icarus, 288:10–36, 2017a. doi:10.1016/j.icarus.2017.01.024.

M. Turbet, F. Forget, J. Leconte, B. Charnay, and G. Tobie. CO2 condensation is a serious limit to the deglaciation of Earth-like planets. Earth and Planetary Science Letters, 476:11–21, 2017b. doi:10.1016/j.epsl.2017.07.050.

M. Turbet, E. Bolmont, J. Leconte, F. Forget, F. Selsis, G. Tobie, A. Caldas, J. Naar, and M. Gillon. Modeling climate diversity, tidal dynamics and the fate of volatiles on TRAPPIST-1 planets. Astronomy & Astrophysics, 612:A86, 2018a. doi:10.1051/0004-6361/201731620.

M. Turbet, E. Bolmont, V. Bourrier, B.-O. Demory, J. Leconte, J. Owen, and E. T. Wolf. A review of possible planetary atmospheres in the TRAPPIST-1 system. Space science reviews, 216(5):1–48, 2020a. doi:10.1007/s11214-020-00719-1.

M. Turbet, C. Gillmann, F. Forget, B. Baudin, A. Palumbo, J. Head, and O. Karatekin. The environmental effects of very large bolide impacts on early Mars explored with a hierarchy of numerical models. Icarus, 335:113419, 2020b. doi:10.1016/j.icarus.2019.113419.

M. Turbet, E. Bolmont, G. Chaverot, D. Ehrenreich, J. Leconte, and E. Marcq. Day–night cloud asymmetry prevents early oceans on Venus but not on Earth. Nature, 598(7880):276–280, 2021. doi:10.1038/s41586-021-03873-w.

V. Van Grootel, C. S. Fernandes, M. Gillon, E. Jehin, J. Manfroid, R. Scuflaire, A. J. Burgasser, K. Barkaoui, Z. Benkhaldoun, A. Burdanov, et al. Stellar parameters for Trappist-1. The Astrophysical Journal, 853(1):30, 2018. doi:10.3847/1538-4357/aaa023.

G. L. Villanueva, M. D. Smith, S. Protopapa, S. Faggi, and A. M. Mandell. Planetary Spectrum Generator: An accurate online radiative transfer suite for atmospheres, comets, small bodies and exoplanets. Journal of Quantitative Spectroscopy and Radiative Transfer, 217:86–104, 2018. doi:10.1016/j.jqsrt.2018.05.023.

A. M. Vinson, D. Tamayo, and B. M. Hansen. The chaotic nature of TRAPPIST-1 planetary spin states. Monthly Notices of the Royal Astronomical Society, 488(4):5739–5747, 2019. doi:10.1093/mnras/stz2113.

P. Von Paris, P. Gratier, P. Bordé, and F. Selsis. Inferring heat recirculation and albedo for exoplanetary atmospheres: Comparing optical phase curves and secondary eclipse data. Astronomy & Astrophysics, 587:A149, 2016. doi:10.1051/0004-6361/201526297.

H. Wang and R. Wordsworth. Extremely long convergence times in a 3D GCM simulation of the sub-Neptune Gliese 1214b. The Astrophysical Journal, 891(1):7, 2020. doi:10.3847/1538-4357/ab6dcc.

D. R. Williams. Venus fact sheet, 2022a. URL `https://nssdc.gsfc.nasa.gov/planetary/factsheet/venusfact.html`. (last accessed: 04.01.2022).

D. R. Williams. Mars fact sheet, 2022b. URL `https://nssdc.gsfc.nasa.gov/planetary/factsheet/marsfact.html`. (last accessed: 04.01.2022).

R. Wordsworth, F. Forget, and V. Eymet. Infrared collision-induced and far-line absorption in dense CO2 atmospheres. Icarus, 210(2):992–997, 2010. doi:10.1016/j.icarus.2010.06.010.

R. Wordsworth, F. Forget, E. Millour, J. Head, J.-B. Madeleine, and B. Charnay. Global modelling of the early martian climate under a denser CO2 atmosphere: Water cycle and ice evolution. Icarus, 222(1):1–19, 2013. doi:10.1016/j.icarus.2012.09.036.

R. D. Wordsworth, F. Forget, F. Selsis, E. Millour, B. Charnay, and J.-B. Madeleine. Gliese 581d is the first discovered terrestrial-mass exoplanet in the habitable zone. The Astrophysical Journal Letters, 733(2):L48, 2011. doi:10.1088/2041-8205/733/2/L48.

R. D. Wordsworth, L. Kerber, R. T. Pierrehumbert, F. Forget, and J. W. Head. Comparison of "warm and wet" and "cold and icy" scenarios for early Mars in a 3-D climate model. Journal of Geophysical Research: Planets, 120(6):1201–1219, 2015. doi:10.1002/2015JE004787.

D. Wright, R. Wittenmyer, C. Tinney, J. Bentley, and J. Zhao. Three planets orbiting Wolf 1061. The Astrophysical Journal Letters, 817(2):L20, 2016. doi:10.3847/2041-8205/817/2/L20.

J. Yang, G. Boué, D. C. Fabrycky, and D. S. Abbot. Strong dependence of the inner edge of the habitable zone on planetary rotation rate. The Astrophysical Journal Letters, 787(1):L2, 2014. doi:10.1088/2041-8205/787/1/L2.

K. J. Zahnle and D. C. Catling. The cosmic shoreline: The evidence that escape determines which planets have atmospheres, and what this may mean for Proxima Centauri b. The Astrophysical Journal, 843 (2):122, 2017. doi:10.3847/1538-4357/aa7846.

M. Zechmeister, S. Dreizler, I. Ribas, A. Reiners, J. Caballero, F. Bauer, V. Béjar, L. González-Cuesta, E. Herrero, S. Lalitha, et al. The CARMENES search for exoplanets around M dwarfs-Two temperate Earth-mass planet candidates around Teegarden's Star. Astronomy & astrophysics, 627:A49, 2019. doi:10.1051/0004-6361/201935460.

R. T. Zellem, N. K. Lewis, H. A. Knutson, C. A. Griffith, A. P. Showman, J. J. Fortney, N. B. Cowan, E. Agol, A. Burrows, D. Charbonneau, et al. The 4.5 μm full-orbit phase curve of the hot Jupiter HD 209458b. The Astrophysical Journal, 790(1):53, 2014. doi:10.1088/0004-637X/790/1/53.

L. Zeng, D. D. Sasselov, and S. B. Jacobsen. Mass–radius relation for rocky planets based on PREM. The Astrophysical Journal, 819(2):127, 2016. doi:10.3847/0004-637X/819/2/127.

Appendices

A Appendix I. Possible rotation states of highly-irradiated M-dwarf exoplanets

Given the absence of synchronous rotator planets in our Solar System, we can ask whether the highly-irradiated exoplanets whose Climate we seek to study are likely to be synchronous rotators? Thus, we have to analyse these worlds' potential for synchronisation by evaluating tidal stress in relation to the orbital distance between two bodies. In fact, despite current studies on brightness modulations made developments towards the understanding of the origin of periodic signals on either the atmosphere or a planetary surface (Lee et al., 2020), the assessment of the spin state of exoplanets from direct observations remain an elusive target, beyond current technological capabilities.

Tidal stress decreases in inverse proportion to the sixth power distance between two bodies. The synchronisation timescale estimates for our Solar System's three innermost planets are 80 Myr, 3 Gyr and 20 Gyr for Mercury, Venus and Earth, respectively (Forget and Leconte, 2014; Leconte et al., 2010). For the Earth, this is consistent with the fact the planet is a fast rotator with a significant obliquity value. However, despite having small obliquities and being slow rotators, Venus and Mercury are not synchronous rotators. These findings can be translated to the case of exoplanetary systems, as tidal synchronisation might not be the only possible rotation state for a planet. We briefly present the most likely states of planetary rotation for highly-irradiated exoplanets, in particular, those orbiting small mass stars:

- **Synchronous rotation**. Rocky planets orbiting inside the HZ inner edge of small mass stars, such as the M-dwarf stars, have much smaller orbital radii than the Solar System planets. The tidal potential for these worlds is very significant, and tidal evolution might lead to low obliquity, eccentricity and spin-orbit synchronisation;

- **Higher order spin-orbit resonance**. If the planet starts with a fast rotation rate, it has the chance of becoming trapped in a high order spin-orbit resonance during the rapid spin-down forced by tidal forces as a consequence of *significant* orbital eccentricity. If a planetary orbit exceeds a given eccentricity threshold, the planet can be captured into a higher-order spin-orbit resonance. Mercury's orbit is the case of a 3:2 spin-orbit resonance, i.e. three rotations per two orbits. Planets with *non-negligible* eccentricity have a higher probability of being captured in a 3:2 or higher spin-orbit resonance, with the possibility of an evolution for a synchronous state (Makarov et al., 2012);

- **Synchronous state with libration**. In compact systems, such as the case of TRAPPIST-1([25]), the planets' relative proximity lead to non-negligible planet-planet gravitational interactions. These are likely to be strong enough to influence orbital dynamics. In particular, for TRAPPIST-1 system, Vinson et al. (2019) concluded that some planets might be pushed into one or two modes of *quasi-stable spin states of synchronous rotation*. The analysis suggests that some planets might be in a synchronous rotation with *libration* and/or *complete circulation of the spin state*. Both cases have timescales on the order of hundreds of planetary orbits. The quasi-stability between these two spin-states means that TRAPPIST-1 planets might switch between the two states in timescales that depend on the planet and tidal dissipation factors assumed, but on the order of 10^3 to 10^5 Earth years;

---

[25] In the case of TRAPPIST-1 planetary system, all seven known planets orbit the host star at a distance inferior to 0.06 AU

- **Thermal tides non-synchronous driven state**. In planets with a thick atmosphere, the effect of thermal tides in the atmosphere can create a torque that drives the planet out of synchronous rotation. This mechanism is thought to have caused Venus to avoid a synchronous rotation, leading the planet to be in a slow retrograde rotation (Auclair-Desrotour et al., 2017; Chapman and Lindzen, 1969; Correia and Laskar, 2001; Ingersoll and Dobrovolskis, 1978; Leconte et al., 2015b). The mechanism can potentially lead rocky exoplanets out of synchronisation (Correia et al., 2008). However, for thermal tides to prevent synchronisation, the planet's orbit must be within a distance range where the stellar tides are strong enough to reduce the solid-body rotation and yet be less intense than the torque driven by atmospheric tides. For TRAPPIST-1, all planets are known to orbit inward this zone, i.e., stellar driven solid-body tides overpower the effects of atmospheric tides. The kind of impact from thermal tides seen in Venus today's atmosphere can not occur in TRAPPIST-1 planetary atmospheres. Atmospheric tides in the TRAPPIST-1 system are unable to significantly change the spin rate of the planets (Turbet et al., 2020a).

The final rotation state of highly-irradiated planets orbiting low-mass stars will depend on factors such as the age of the system, orbital eccentricity, compactness of the orbital architecture, orbital distance and the potential for thermal tides to drive a planet out of synchronous rotation. For TRAPPIST-1, a planetary system older than the Solar System, with 8 Gyr (Burgasser and Mamajek, 2017), the orbital characteristics: an old, compact system with very low orbital eccentricities (Agol et al., 2021; Grimm et al., 2018; Turbet et al., 2020a) lead to a likely assumption of a near tidal equilibrium, with small obliquities, orbital circularisation and, likely, a tide-locked state (Turbet et al., 2020a) with high order spin-orbit resonances being unlikely (Turbet et al., 2018a) ([26]). Therefore, the assumption of synchronous rotation for the highly-irradiated planets with possible Venus-like climates orbiting small mass stars is a likely one (Dobrovolskis, 2009). The present understanding of orbital evolution opens the possibility of higher-order spin-orbit resonances for significant orbital eccentricities. In compact systems, libration might have to be considered for more complex Climate simulations.

---

[26] The TRAPPIST-1 system's planets have orbital eccentricities lower than 0.01 (Grimm et al., 2018), making capture into a high order synchronous rotation unlikely (Turbet et al., 2018a). The study has taken into consideration planet-planet interactions and tides, revealing that the probability of capture into higher-order spin-orbit resonance becomes only greater than 10% for eccentricities above 0.03.

B Appendix II. PCAR - Phase Curves Assessment Routine

Phase Curves Assessment Routine (PCAR)

Version (3) December 15th 2021
Based on the code developed for spectral curve analysis on April/May 2021.
Updated on July 2021 to include corrections to the phase curves and spectra.
Authors: Diogo Quirino, Gabriella Gilli

Libraries

```
import netCDF4 as nc4
import numpy as np
import math as math
import matplotlib.pyplot as plt
import matplotlib.ticker as tck
from matplotlib.ticker import ScalarFormatter
```

Section 1: Calling and assessing GCM and star parameters (variables)

Subsection 1.1. - GCM output files

```
filepath = [path to the file with the radiative TOA flux (reflection or emission)]
#Calling the files
filename = nc4.Dataset(filepath, ‘r’, Format =‘NetCDF4’)
# Assessment for the GCM output files Simple code lines to check variable keys and generic information.
# Uncomment for using.
#Print variables keys for a specific test to check which variables are present in each test.
#print (filename.variables.keys())
#Print the characteristics of the variable: type, organisation, title, units, shape, default value.
#print (filename[“OLR3D”]) # Select the variable you want to analyse.
# Declare in the tag if the file corresponds to visible or IR light.
tag = [Declared by the user]
```

Subsection 1.2. - Stellar spectrum files

```
#Path for the txt or dat file that contains the stellar spectrum flux file
flux_path = [Path to the stellar spectrum flux file]
#Open and read the stellar spectrum flux file
file = open (flux_path, ‘r’).readlines()
#Creates the stellar surface flux file
surface_flux = [float(line[:-1]) for line in file]
#Conversion from list into array
flux_surface = np.array(surface_flux)
#Path for the txt or dat file that contains the wavelength path associated with the stellar flux file
wavelength_path = [Path to wavelength file]
#Open and read the wavelength file
file2 = open (wavelength_path, ‘r’).readlines()
#Creates the wavelength file
lambdas = [float(line[:-1]) for line in file2]
```

```
#Conversion from list into array
lambdas = np.array(lambdas)
```

Section 2: Defining GCM variables and physical parameters

Subsection 2.1. - Defining GCM variables

```
#Latitude
lat = filename[“latitude”][:]
#Longitude
lon = filename[“longitude”][:]
#cell area
area = filename[“aire”][:, :]
```

```
#Progression of day. Now a note of caution, the code presented here has been built for the
#Generic-GCM and for a planet in a synchronous rotation. The code can be modified to
#higher-order spin-orbit resonances, as explained bellow.
```

```
#Sub-observer longitude
solon = lon[::-1]
```

```
#Note that in this case we are considering a tidally-locked planet, as such the sub-observer longitude
#evolves from 180° to 0°, then to -180°. It is possible to simulate higher-order spin-orbit resonances if
#the radiative time step coincides with known sub-observer longitudes. In that case, a user can update
#the sub-observer longitude (in the inclination 90° case) to match the radiative time step. For example in
#a 2:1 spin-orbit resonance, the planet will complete two rotations in one orbit. If the radiative time step
#is 9 per orbit then the user can represent 9 different sub-observer longitudes by defining a new solon
#array.
```

```
#Sub-observer latitude (dependent on the inclination)
#Is set to remain constant throughout the iterative process
inclination = 90 # defined by the user
solat = 90 - inclination
```

Subsection 2.2. - Interaction with user

```
if tag == “VIS”: # if the user selects the visible file
    #Instantaneous intensity of the short-wavelength radiation coming from the planet
    OSR3Di = filename[“OSR3D”][:, :, :, :].mean(axis = 0)
    radiation = OSR3Di
    wavenumberVI = filename[“VI_Wavenumber”][:]
    bandwidthVI = filename[“VI_Bandwidth”][:]
    bandwidth = bandwidthVI
    wavenumber = wavenumberVI
elif tag == “IR”: # if the user selects the thermal file
    OLR3Di = filename[“OLR3D”][:, :, :, :].mean(axis = 0)
    radiation = OLR3Di
    wavenumberIR = filename[“IR_Wavenumber”][:]
    bandwidthIR = filename[“IR_Bandwidth”][:]
    bandwidth = bandwidthIR
```

```
    wavenumber = wavenumberIR

#Wavenumber [cm^-1] conversion to wavelengths in [μm]
wavelength = (1/wavenumber) * 1e4
```

Subsection 2.3. - Defining Planetary physical parameters

```
#TRAPPIST-1 c semimajor axis in [m]
UA = 1495978707e2 # meters
a = 0.0158 * UA

# Distance to Earth in [m]
d = 12.4 * 3.08567758e16

#Stellar radius for TRAPPIST-1 according to Agol et al., 2021
R_Sun = 6.957e8 # nominal solar radius in [m], according to IAU
R_star = 0.1192 * R_Sun # TRAPPIST-1 radius according to Agol et al., 2021

#Calculates the ratio between squared stellar radius and the planet’s semimajor axis
R_a = (R_star / a)**2
```

Subsection 2.4. - Wavelength range extremes

```
#Calculates the range extremes for each wavelength band
min_band = wavenumber - bandwidth/2 ; max_band = wavenumber + bandwidth/2
#And converts these values from wavenumbers to wavelengths
max_wavelength = 1/min_band*1e4 ; min_wavelength = 1/max_band*1e4
```

Section 3: Obtaining the planetary orbital phase disk-integration intensity variation

Subsection 3.1. - Angle between two points located on a sphere’s surface

```
#Note that this is important for two reasons, as it yields the observer angle between a cell and the
#sub-observer point. The second reason is that it limits the flux to the cells in the Earth-facing hemisphere.

def get_angle (lat1, lon1, lat2, lon2):
    “““Returns the angle between two points on a sphere.
    Important: the parameters are given in degrees!
    Requires: 2 latitudes and 2 longitudes from each point on the surface of the sphere.
    Latitude and longitude are introduced in degrees and then converted into radians.
    Ensures: A float, the angle between the two points in radians.
    ”””

    A1 = lat1*np.pi/180 ; A2 = lon1*np.pi/180 ; B1 = lat2*np.pi/180 ; B2 = lon2*np.pi/180

    #Difference in longitude.
    delta = B2 - A2
    formula = np.sin(A1) * np.sin(B1) + np.cos(A1) * np.cos(B1) * np.cos(delta)

    return math.acos (formula)
```

Subsection 3.2. - Planetary orbital phase disk-integrated intensity calculation

```
#Part of the code dedicated to calculate the planetary disk-integrated intensity according to the equation
#(10) in von Paris et al., 2016 and following the recommendation by Frank Selsis and Martin Turbet.

#Empty list to save the orbital phase disk-integrated intensity evolution
```

```
phaseIntensity = []

#For each orbital phase, given by the evolution of the sub-observer longitude, solon:
for p in range(len(solon) - 1):

    #Creates an empty list that receives the disk-integrated flux divided by π
    planetaryIntensity = []

    #Prints (uncomment if you like) the actual orbital phase of the calculations.
    #print(solon[p])

    #For each wavenumber k:
    for k in range(len(wavenumber)):

        #Declares the initial Planetary Flux to be zero (before another run)
        Flux = 0

        #For each cell (latitude x longitude):
        for i in range(len(lat)):
            for j in range(len(lon) - 1):

                #Calculates the angle between the sub-observer point (solat, solon) and each cell centre
                #grid point
                angle_value = get_angle(solat, solon[p], lat[i], lon[j])

                #If the angle between these two points is smaller than π/2, then it is visible to the observer
                #and the cell can be considered for disk-integration!
                if angle_value <= np.pi/2:

                    #Flux disk integration: it integrates the flux contribution from every cell visible to
                    #the observer, for a given wavenumber assuming the relative contribution cell surface
                    #area and the one from the cosine of the observer angle.
                    Flux += radiation[k, i, j] * np.cos(angle_value) * area[i, j] * bandwidth[k] / \
                    (max_wavelength[k] - min_wavelength[k])

                    #Note the existence of the conversion factor for the radiation which is originally given
                    #in units W/m^2/cm^-1 (as a function of wavenumber). By using the unit conversion,
                    #radiation is now expressed in terms of wavelength, such that its units are in W/m^2/µm.

        #Assuming an isotropic distribution of intensity, we divide the flux per π. This is the
        #disk-integrated intensity for a specific wavenumber k.
        planetaryIntensity.append(Flux/(np.pi))
        #In the end, the length of the planetaryIntensity must be equal to that of the wavenumber.
        #Advances to the next wavenumber within the *same* orbital phase.

    #Appends the resulting disk-integrated intensities, per wavenumber, for a given orbital phase
    phaseIntensity.append(planetaryIntensity)

    #Advances to the *next* orbital phase configuration.

#Converts the list phaseIntensity to an array for future calculations related with the ratio planet/star
#contrast.
phaseIntensity = np.array(phaseIntensity)
```

```
#This is the array that contains all the information related to the planetary intensity variation per orbital
#phase, for every wavenumber established in the GCM files. This is a way of storing information for
#phase curve calculations. However, we are interested in gathering information for separate bands. This
#is why we must come up with an array that gives the disk-integrated planetary intensity for each orbital
#phase of the planet.
```

Subsection 3.3. - Orbital phase disk-integrated intensity for a given band/central wavenumber

```
def pInt (k):
    “““Orbital phase evolution of the disk-integrated intensity for a given band or, as defined by the GCM
    output file, per a given central wavenumber k.
    Requires: an integer, representing the wavenumber or band number that you are interested in.
    Ensures: the orbital phase variation of the disk-integrated intensity for a specific wavenumber.
    ”””
    #Creates an empty list for the disk-integrated intensity for a given band across the planet’s orbital
    #phase evolution.
    p_Intensity = []

    #For a given central wavenumber k from a band, per orbital phase:
    for orbital_phase in range(len(phaseIntensity)):
        #Appends to the list the planetary disk-integrated intensity from a given band/central
        #wavenumber k, for an orbital phase.
        p_Intensity.append(phaseIntensity[orbital_phase][k])
    #The resulting object must have a length equal to that solon-1 and must represent the planetary
    #disk-integration evolution over the course of an orbit, for a selected band/central wavenumber k.
    return p_Intensity
```

Subsection 3.4. - Planetary disk-integrated intensity for a given orbital phase, across the wavelength range

```
def orbital_phase(phase):
    “““Planetary disk-integrated intensity behaviour for a given orbital phase, across the entire range of
    available wavelengths.
    Requires: phase is an integer from 0 to 63 that represents the orbital phase (total of 64 orbital phases).
    Ensures: An array, the disk-integrated intensity for a given orbital phase.
    ”””
    return phaseIntensity[phase]
```

Section 4: Stellar Flux Proceedings

```
#Normalisation and calibration of the stellar flux
flux_norm = 0
for i in range(1, len(lambdas) - 1):
    flux_norm += flux_surface[i] * (lambdas[i + 1] - lambdas[i - 1])/2
calibration = L_star / (4 * np.pi * (R_star**2))
for i in range(0, len(lambdas)):
    flux_surface[i] = flux_surface[i] * calibration / flux_norm
stellar_spectra = flux_surface
```

```
#Creates the same wavelength range for the stellar flux as in the planetary flux
wave_limits = np.zeros((len(wavenumber), 2), dtype=’f’)
wave_mic = np.zeros(len(wavenumber), dtype=’f’)
for i in range(0, len(wavenumber)):
    #Creates the limits of the band
    wave_limits[i,0]= 1e4 / (wavenumber[i] + bandwidth[i] / 2)
    wave_limits[i,1]= 1e4 / (wavenumber[i] - bandwidth[i] / 2)
    #Creates the central value
    wave_mic[i]= 1e4 / wavenumber[i]
#Creates the array to receive the stellar flux at each band
spec_star_band = np.zeros((len(wavenumber)))
for i in range(0, len(wavenumber)):
    for j in range(1, len(lambdas)-1):
        if((lambdas[j] > wave_limits[i,0]) and (lambdas[j] < wave_limits[i,1])):
            spec_star_band[i] += stellar_spectra[j] * (lambdas[j+1] - lambdas[j-1]) / + \
                    (2*(wave_limits[i,1] - wave_limits[i,0]))
```

Section 5: Plotting functions

Subsection 5.1. - Planet-to-star contrast function

```
#Planet to star contrast ratio for a given band
def ratio (band):
    “““Planet to star contrast ratio per band.
    Requires: band, an integer representing the index of the band/central wavenumber.
    Ensures: an array, planet_to_star, representing the planet-to-star contrast ratio for the specific band
    of interest.
    ”””

    # Calculates the star contribution for the planet-to-star contrast ratio.
    #First, it creates an array with zero values whose length is equal to the number of orbital phases.
    #Second, since the stellar flux is assumed to be constant over the planet’s orbital period, the normalised
    #and calibrated stellar flux value for a given band will be added to the zero values array.
    #A contribution from the squared planet semimajor axis is included.
    #This inclusion follows the description given by von Paris et al., 2016 on how to calculate the phase
    #curves, and the suggestion given by Franck Selsis.
    sflux = np.zeros(len(pInt(band))) + ((spec_star_band[band])*np.pi*(R_star**2 / (d**2)))
    #Third, it calculates the ratio between the planetary contribution (time-dependent) and the
    #star contribution (time invariant), to yield the planet-to-star contrast ratio for a given band.
    planet_to_star = pInt(band) / sflux
    return planet_to_star
```

Subsection 5.2 - Orbital phase dependent planet-to-star contrast variation function

```
def ratio_band (phase):
    “““Orbital phase dependent planet-to-star contrast variation.
    Requires: phase, an integer that represents the orbital phase.‘
    Ensures: ratio, an array representing the planet-to-star contrast per wavelength for a selected orbital
    phase.
```

```
    ”””
    #Creates an empty list to receive the stellar flux.
    sflux_band = []
    #For each band/central wavenumber, appends the stellar flux for that band.
    #(which is a time invariant)
    for band in range(len(wavenumber)):
        sflux_band.append(spec_star_band[band] * np.pi * (R_star**2 / (d**2)))
    #In practice, a ratio of planetary and stellar intensities, it takes the planetary, disk-integrated, intensity
    #across all bands, orbital_phase(phase), for a given orbital phase, i.e., the function’s argument ”phase”.
    #It divides the planetary and stellar intensities across the respective bands to create a ratio that
    #retrieves the planet-to-star contrast per band for a selected orbital phase.
    ratio = orbital_phase(phase) / sflux_band
    return ratio
```

Section 6: Data visualisation

Subsection 6.1. - Phase Curves visualisation

```
#Phase curve plot initialisation
plt.close()
#Initial definitions
plt.figure(figsize = (7,8))
ax = plt.subplot(1,1,1)
ax.grid(which = “both”, alpha = 1.)
#Phase curves selection
bands = [2, 7, 10, 13, 16, 24, 35] #example of selecting by central wavenumber/wavelength

#Plots the phase curves for any given band
bands = bands[::-1]

for i in range(len(bands)):
    novo = ratio(bands[i])[0]
    newlist = list(ratio(bands[i]))
    newlist.append(novo)
    plt.semilogy(solon[:][::-1], newlist, linewidth = 2.75)

# L A B E L L I N G
#Labelsize and ticks parameters
plt.tick_params(labelsize = 17)
plt.tick_params(which = “both”, right = True, top = True)
plt.tick_params(which = “major”, length = 5, width = 1.25)
plt.tick_params(which = “minor”, length = 2, width = 1.3)
#Axis terminology and identification
plt.xlabel(“orbital phase”, fontsize = 17)
plt.ylabel(“planet/star contrast”, fontsize = 17)
#Axis limits
xlimits = plt.xlim(-180, 180) ; ylimits = plt.ylim(6e-11, 2e-6)
plt.xticks([-180, -90, 0, 90, 180])
```

```
#Inclination i box
rounded_box = dict(boxstyle = “round”, edgecolor = “black”, facecolor = “wheat”, alpha = 0.95)
i_text = plt.text(120, 1.2e-6, “i = ” + str(inclination) + “°”, fontsize = 16, bbox = rounded_box)
#Subplot label
plt.text(-168, 1.2e-6, “a”, fontweight = “bold”, fontsize = 24)
#Saves the figure
plt.tight_layout()
```

Subsection 6.2. - Orbital phase and band-dependent planet-to-star contrast visualisation

```
#Plot initialisation
plt.close()
fig = plt.figure(figsize = (14, 7))
ax = plt.subplot(111)
ax.grid(which = “both”, alpha = 0.3)
ax.grid(which = “major”, alpha = 0.9)
#Orbital phases and legend correspondence
orbital_phases = [ratio_band(8), ratio_band(16), ratio_band(24), ratio_band(32), ratio_band(40), ratio_band(48),
ratio_band(56)]
orbital_phases_legend = [r“−3π/4”, r“−π/2”, r“−π/4”, r“0”, r“π/4”, r“π/2”, r“3π/4”]
colour = [“blue”, “darkgreen”, “teal”, “black”, “darkorange”, “deeppink”, “red”]
#Plotting
for phase in range(len(orbital_phases)):
    plt.semilogy(wavelength, orbital_phases[phase], color = colour[phase], lw = 2.75, \
    orbital_phases_legend[phase])
# L A B E L L I N G
#Labelsize and ticks parameters
plt.tick_params(which = “both”, labelsize = 17, right = True, top = True)
ax.xaxis.set_minor_locator(tck.MultipleLocator(0.1))
ax.xaxis.set_major_locator(tck.MultipleLocator(0.5))
plt.tick_params(which = “major”, length = 6, width = 1.25)
plt.tick_params(which = “minor”, length = 3, width = 1.3)
#Axis terminology and identification
plt.xlabel(“Wavelength, λ [μm]”, fontsize = 17)
plt.ylabel(“planet/star contrast”, fontsize = 17)
plt.xlim(0.1, 5.1) ; plt.ylim(3e-9, 4e-4)
plt.ylim(6e-11, 6e-6)
#Inclination i box
rounded_box = dict(boxstyle = “round”, edgecolor = “black”, facecolor = “wheat”, alpha = 0.95)
i_text = plt.text(4.65, 2.5e-6, “i = ” + str(inclination) + “°”, fontsize = 16, bbox = rounded_box)
#Legend
plt.legend(fontsize = 15.5, edgecolor = “black”, loc = “lower left”, framealpha = 1)
#Saves the figure
plt.tight_layout()
```